ENGINEERING AND CHARACTERIZING LIGHT-MATTER
INTERACTIONS IN PHOTONIC CRYSTALS


BY

ANDREW BRZEZINSKI


DISSERTATION

Submitted in partial fulfillment of the requirements
for the degree of Doctor of Philosophy in Materials Science and Engineering
in the Graduate College of the
University of Illinois at Urbana-Champaign, 2010


Urbana, Illinois


Doctoral Committee:

   Professor Paul Braun, Chair
   Professor Pierre Wiltzius, University of California, Santa Barbara
   Professor John Rogers
   Associate Professor Harley T. Johnson

| Report Documentation Page | | *Form Approved*<br>*OMB No. 0704-0188* |
|---|---|---|

Public reporting burden for the collection of information is estimated to average 1 hour per response, including the time for reviewing instructions, searching existing data sources, gathering and maintaining the data needed, and completing and reviewing the collection of information. Send comments regarding this burden estimate or any other aspect of this collection of information, including suggestions for reducing this burden, to Washington Headquarters Services, Directorate for Information Operations and Reports, 1215 Jefferson Davis Highway, Suite 1204, Arlington VA 22202-4302. Respondents should be aware that notwithstanding any other provision of law, no person shall be subject to a penalty for failing to comply with a collection of information if it does not display a currently valid OMB control number.

| 1. REPORT DATE<br>**2010** | 2. REPORT TYPE | 3. DATES COVERED<br>**00-00-2010 to 00-00-2010** |
|---|---|---|
| 4. TITLE AND SUBTITLE<br>**Engineering and Characterizing Light-Matter Interactions in Photonic Crystals** | | 5a. CONTRACT NUMBER |
| | | 5b. GRANT NUMBER |
| | | 5c. PROGRAM ELEMENT NUMBER |
| 6. AUTHOR(S) | | 5d. PROJECT NUMBER |
| | | 5e. TASK NUMBER |
| | | 5f. WORK UNIT NUMBER |
| 7. PERFORMING ORGANIZATION NAME(S) AND ADDRESS(ES)<br>**University of Illinois at Urbana-Champaign,Urbana,IL,61801** | | 8. PERFORMING ORGANIZATION REPORT NUMBER |
| 9. SPONSORING/MONITORING AGENCY NAME(S) AND ADDRESS(ES) | | 10. SPONSOR/MONITOR'S ACRONYM(S) |
| | | 11. SPONSOR/MONITOR'S REPORT NUMBER(S) |

| 12. DISTRIBUTION/AVAILABILITY STATEMENT<br>**Approved for public release; distribution unlimited** |
|---|

| 13. SUPPLEMENTARY NOTES |
|---|

14. ABSTRACT

**Photonic crystals can affect the behavior of visible light, and other electromagnetic waves, in ways that are not possible by other means. The propagation of photons can be completely forbidden or the the light can be made to follow a welldefined path. Fluorescent emission can be enhanced for some wavelengths or completely shut off for others, and it is possible to do all this simultaneously in a single structure. However, photonic crystals are very difficult to fabricate as they require precision patterning at sub-micron length scales. This fabrication difficulty has resulted in many of the potential applications for photonic crystals to currently be unrealized. Similarly, there is an abundance of opportunities to explore the workings of photonic crystals and also to develop exciting new methods for their fabrication. The content of this dissertation explores some methods for fabricating photonic crystals, including direct laser writing, interference lithography, colloidal deposition, and chemical vapor deposition. The angle-resolved characterization of photonic crystals is performed on fluorescent photonic crystals that exhibit uniquely photonic effects, which are explained with a simplified model of the electromagnetic wave-functions. Another model is shown to well-explain the emission from fluorescent photonic crystals that are not of sufficient quality to exhibit truly photonic effects. The ability to perform angleresolved optical characterization is improved with a commercial 4-circle diffractometer. A method to determination the resulting structure of conformal deposition processes proves useful as a tool for the design, modeling, and characterization of photonic crystals. Finally, attempts are made to radically alter the emission of light from rare earth emitters embedded inside photonic crystals.**

| 15. SUBJECT TERMS | | | | | |
|---|---|---|---|---|---|

| 16. SECURITY CLASSIFICATION OF: | | | 17. LIMITATION OF ABSTRACT | 18. NUMBER OF PAGES | 19a. NAME OF RESPONSIBLE PERSON |
|---|---|---|---|---|---|
| a. REPORT<br>**unclassified** | b. ABSTRACT<br>**unclassified** | c. THIS PAGE<br>**unclassified** | **Same as Report (SAR)** | **115** | |

**ABSTRACT**

Photonic crystals can affect the behavior of visible light, and other electromagnetic waves, in ways that are not possible by other means. The propagation of photons can be completely forbidden or the the light can be made to follow a well-defined path. Fluorescent emission can be enhanced for some wavelengths or completely shut off for others, and it is possible to do all this simultaneously in a single structure. However, photonic crystals are very difficult to fabricate as they require precision patterning at sub-micron length scales. This fabrication difficulty has resulted in many of the potential applications for photonic crystals to currently be unrealized. Similarly, there is an abundance of opportunities to explore the workings of photonic crystals and also to develop exciting new methods for their fabrication.

The content of this dissertation explores some methods for fabricating photonic crystals, including direct laser writing, interference lithography, colloidal deposition, and chemical vapor deposition. The angle-resolved characterization of photonic crystals is performed on fluorescent photonic crystals that exhibit uniquely photonic effects, which are explained with a simplified model of the electromagnetic wave-functions. Another model is shown to well-explain the emission from fluorescent photonic crystals that are not of sufficient quality to exhibit truly photonic effects. The ability to perform angle-resolved optical characterization is improved with a commercial 4-circle diffractometer. A method to determination the resulting structure of conformal deposition processes proves useful as a tool for the design, modeling, and characterization of photonic

crystals. Finally, attempts are made to radically alter the emission of light from rare earth emitters embedded inside photonic crystals.

*To my Mother*

# ACKNOWLEDGEMENTS

I wish to thank my advisors, Professor Paul Braun and Professor Pierre Wiltzius. Together, they provided me with a steady stream of guidance, insight, encouragement and inspiration. Paul was an excellent model of industriousness, knowledgeability, creativity and friendliness. Pierre's hands-off management style was complemented by his remarkable ability to ask the right questions, which forced you to think like a scientist. I was very fortunate to be co-advised by Paul and Pierre, and equally fortunate to work in the research groups that they headed.

There are many colleagues that have greatly enriched my experiences while at Illinois. I truly believe that the group I was a part of were some of the most friendly and helpful people that anybody could hope to work with. I wish to thank them all.

I would like to thank my Mother, who has always been supportive and caring. I hope that she is pleased with the choices that I have made in my life.

Furthermore, I want to thank Lauren Flynn for standing by me and putting up with the frustrations of a long-distance relationship. I am very happy that we have finally gotten married.

**TABLE OF CONTENTS**

# CHAPTER 1

# INTRODUCTION

## 1.1 Photonic Crystals

Photonic crystals [1] obtain interesting electromagnetic properties by virtue of their periodic structure. When the dielectric constant is modulated in one, two, or three dimensions the electromagnetic wave-functions obtain forms that can be radically different from the plane-wave form found in homogeneous dielectric media. Some of the first studies of photonic crystals occurred around a century ago, when Lord Rayleigh studied optical reflections from a one-dimensional periodic dielectric stack [2]. However, it was in 1987 that Yablonovich [3] and John [4] independently and simultaneously proposed the existence of complete photonic band-gaps in photonic crystals. Much of the theory behind the physics of photonic crystals had already been developed in the preceding decades. For example, Bloch [5] described the behavior of waves in three-dimensional periodic structures. Also, Ewald [6] developed dynamical diffraction theory, which describes electromagnetic wave-functions in photonic crystals, such as x-rays propagating in crystalline matter. The ground breaking content of the proposals by Yablonovich and John is the existence of complete photonic band-gaps, where electromagnetic waves having certain energies can be forbidden from propagating.

## 1.1.1 Partial Photonic Band-gaps

Partial band-gaps, known as stop-gaps, can occur along certain directions in the photonic crystal because sufficient dielectric contrast in combination with the

appropriate periodicity causes strong diffraction for certain electromagnetic wavelengths. In a one-dimensional photonic crystal, the stop-gaps change the plane-wave modes of free-space into a new set of modes that are linear combinations of forward and backward propagating waves [1]. The modes that once existed in free space with a photon energy corresponding to the center of the stop-gap have been pushed out of the gap and into the energy regions adjacent to the partial gap where they contribute to a local increase in the density of modes [5,7]. This mechanism can used to engineering the optical response of a photonic crystal by manipulation of the spatial distribution of the dielectric material. The propagation of light within a photonic crystal can be shaped to encourage more light to travel in certain directions while preventing propagation in the stop-gap directions.

1.1.2 Complete Photonic Band-gaps

Complete band-gaps can form in three-dimensional photonic crystals if there is enough overlap in both the direction and energy of the stop-gaps [4]. Two important criteria for creating complete band-gaps are having sufficiently large dielectric contrast and having an appropriate periodic structure, in three-dimensions.

1.1.3 Consequences of Fermi's Golden Rule

Luminescent and absorbing molecules will behave differently when incorporated into photonic crystals. According to Fermi's Golden Rule, the rate of emission or absorption is proportional to the density per unit energy of the available electromagnetic modes [8]. Placing an emissive molecule into a structure with a complete photonic

band-gap would forbid the molecule from emitting any photons at the energy corresponding to the band-gap [3]. This same emitter, when placed within a complete band-gap structure, would have its emission rate increased at energies ranges just outside of the band-gap, where the electromagnetic density of modes is typically increased [8]. This occurs because the modes which may not exist within the gap are altered and redistributed into nearby energy ranges. Similarly, an absorptive molecule can increase its rate of absorption if the absorption energy falls at the band-gap edge [6]. Also, absorption can not occur is for energies within the band-gap as the electromagnetic modes are forbidden. The above rules also apply to structures with partial band-gaps but the results may be less dramatic than in the complete band-gap case.

1.1.4 Applications for Photonic Crystals

Many applications have been proposed for photonic crystals. One such application is the creation of loss-less waveguides that are ultra-compact and can have bends with zero radius of curvature [9-13]. Inside of a photonic crystal with a complete band-gap, a zero-loss waveguide can be created by introducing a line defect into an otherwise perfect structure. Analogous to semiconductors, the defect will manifest as a wave-function mode that has an energy within the band-gap. As electrons are fermions, we would expect only a single electron to populate a defect mode. However, photons are bosons so a limitless number of them can populate the defect mode in the photonic crystal. These photons, with energies inside the band-gap, will be guided through the photonic crystal by the defect while being unable to escape the waveguide.

Other applications include omni-directional mirrors [14,15], where photons at any incident angle are reflected for energies within the band-gap. The zero-threshold laser [16,17] is created by engineering the electromagnetic modes in a photonic crystal so that emission from the gain region primarily occurs into the spatial mode of the laser resonator. Such lasers can be very compact and power efficient with makes them suitable for integrated optical devices, which could hold hundreds, thousands or more of these lasers.

## 1.2 Methods for Manufacturing Three-Dimensional Photonic Crystals

### 1.2.1 Colloidal Crystals

Some of the first experimental realizations of photonic crystals were fabricated using mono-disperse colloidal particles [18,19]. A variety of techniques can induce the self-assembly of these colloidal crystals. The earliest methods involved sedimenting [20] colloids from a solution so that a closed-packed crystal is formed at the bottom of the container. The method of vertical deposition [21] can create colloidal crystals of very high quality. In vertical deposition, a substrate is placed vertically in a solution of colloids. As solvent evaporates from the meniscus, the colloids are drawn up by the forces and form into an face-centered-cubic arrangement. Most of these self-assembly methods result in close-packed structures, typically face-centered cubic with the (111) plane parallel to the substrate. However, patterning the substrate with dimples [22] so that it acts as a template in conjunction with sedimentation has been used to produce colloidal crystals with different structural symmetry and orientation. Another method to

template the colloids employs a flow cell where a colloid solution is flowed into the cell [23] and the colloids are forced to self-assemble by the restricted geometry. This flow cell method is also capable of controlling structural symmetry and orientation.

Colloidal crystals are relatively easy to fabricate but they have some disadvantages when used as photonic crystals. There are two main reasons why most colloidal crystals use colloids of polystyrene, silica, polymethyl methacrylate, or similarly low refractive index materials [24]. First, it is more difficult to fabricate colloids in high refractive index materials. Second, high refractive index materials are often denser which negatively impacts the balance between gravity and buoyancy necessary for colloidal crystal formation. The low refractive index colloids are not capable of having complete band-gaps [4]. Although colloidal crystals can exhibit reasonably strong partial band-gaps, the inclusion of defects inherent in the manufacturing process [21] degrades the quality of the photonic crystal. These defects include vacancies, stacking faults, and drying cracks. Furthermore, the strong preference to form into close packed structures plus the fixed spherical shape of the colloids preclude the ability to easily alter the colloidal crystal structure. Hence, the photonic properties of colloidal crystals are somewhat fixed to a limited subset of what could be possible, using other structures.

1.2.2 Multi-Beam Interference Lithography

When a single laser beam is split into two coherent beams which are directed to overlap each other, a periodic one-dimensional standing wave pattern is formed. This pattern is readily recorded in a photo-resist, which can be developed to reveal a structure having the same form as the original standing wave. When a third coherent

beam is added, which is not parallel to other beams, a periodic two-dimensional interference pattern is formed. A fourth beam, not co-planer with the others, results in a periodic three-dimensional pattern that can be recorded in photo-resist. By altering the directions of the beams and their polarization vectors, it is possible to make a great variety of periodic structures with control over the structure symmetry, periodic spacing, and shape of the unit cell [25-27]. As the photo-resist faithfully records the interference pattern, it is possible to create large-scale defect free structures for use as photonic crystals.

There are some limitations to multi-beam interference lithography. A high quality laser beam with profile that is sufficiently uniform over the exposure volume is needed to produce a uniform interference pattern. Some beam angles may not be achievable inside the photo-resist due to refraction at the photo-resist interface. This refraction problem can be addressed with a scheme to couple the beam into the photo-resist [28], but the cost is an increased complexity in the optical setup. With four beams, the optical setup become somewhat complex, requiring numerous mirrors, wave-plates, and beam-splitters. Such a complex setup is difficult to align and prone to becoming unaligned, which makes it difficult to achieve a uniform interference pattern in the exposure volume. Furthermore, suitable photo-resists typically have a low refractive index of 1.5, which is insufficient to form complete photonic band-gaps.

1.2.3 Direct Laser Writing

Direct laser writing [29,30] is a versatile method of recording any type of pattern, within some resolution limit, into a photo sensitive film. In direct laser writing, a laser

6

beam is brought into a tight focus within the photo sensitive film. Polymerization only occurs at the focal point, where the intensity is sufficiently high to cause an appreciable amount of two-photon absorption. The focal point is then translated such that a three-dimensional pattern is directly drawn into the film.

Two photon absorption is the process by which a molecule simultaneously absorbs two photons having a certain wavelength and uses the combined energy as if the molecule absorbed a single photon with a wavelength that was half as long. The two photon absorption cross-section for most substances is very small relative to the single photon absorption cross-section [31]. Thus, a very high intensity or flux of photons is needed in order to have appreciable amounts of two photon absorption. Furthermore, the rate of two photon absorption is proportional to the square of the intensity rather than being proportional to the just the intensity, as in the case of single photon absorption. By using a very high numerical aperture lens, such as an oil immersion microscope objective, a region of extremely high intensity is created at the focal point. When the square of the intensity at the focal point is sufficient to induce polymerization via two photon absorption, the square of the intensity outside the focal point drops off quickly. Almost zero two photon absorption will occurs beyond about half a wave length out from the focal point [32]. In this way, polymerization only occurs at the focal point while the remainder of the film is unchanged from its unexposed state.

Pulsed titanium sapphire lasers [33], with pulse widths of about 100 femto-seconds, are often employed for direct laser writing. The femto second pulses have extremely high peak intensity that readily initiate polymerization in a variety of photo-resists. However, reports do exist where nano-second pulsed Nd:YAG lasers have

successfully been used for direct laser writing [34]. Two photon absorption still occurs in pulsed lasers with lower peak power, or even with continuous lasers [35]. However, a much higher average flux is required in order to achieve the same number of photons absorbed via the two photon process, compared with femto-second lasers.

1.2.4 Proximity Field Nano-Patterning

A more recently developed fabrication method that incorporates the principles of multi-beam interference lithography but simplifies the optical setup is proximity field nano-pattering [36-38]. Instead of using optical elements to split a laser beam, a diffraction grating is embossed on to the surface of the photo-resist. This grating serves to split a single laser beam into numerous overlapping beams that form an interference pattern within the photo-resist. Compared with multi-beam interference lithography, there is some sacrifice in the level of control over the intensity, polarization, and direction of the beams that exit the grating. The parameters of the beams are controlled by the depth, spacing, and unit cell shape of the embossed diffraction grating, in conjunction with the direction, and polarization of the single incoming exposure beam. The desired relief pattern is etched into a silicon master, which is then replicated into a stamp made of polydimethylsiloxane. The stamp is then placed in conformal contact with the photo-resist surface. A small amount of solvent and slightly elevated temperature will cause the photo-resist surface to adopt the relief pattern of the original silicon master mold. Then the stamp is  removed and the photo-resist is then exposed. A particular advantage of this method is the ability to expose with a pulsed titanium sapphire laser to induce polymerization in a two-photon process, which greatly

enhances the pattern fidelity and structural integrity.

1.3 Photo-Resists for Photonic Crystal Fabrication

A variety of photo-resists have been successfully employed in the making of photonic crystals. However, the commercially available EPON SU8 has many properties that make it better-suited compared with most other photo-resists [39,40]. The SU8 monomer has, on average, eight epoxy groups, that under go a ring-opening polymerization in the presence of an acid catalyst. SU8 falls into the category of being a chemically amplified resist, because a single absorption event will generate an acid proton which will catalyze many ring opening polymerizations. So less light absorption is required to achieve the same degree of polymerization compared with a non-amplified photo-resist, such as poly-methyl-methacrylate. SU8 also has the advantage of forming strong, highly cross-linked films, due to the monomer's high degree of functionality. The mechanical robustness of highly cross-linked SU8 enables it to better withstand further processing at elevated temperatures, where other photo-resists would fail. Furthermore, the acid-catalyzed ring opening polymerization only occurs very slowly at temperatures below 60 degrees. This permits lengthy patterning of SU8 to take place at room temperature, where the generated acid diffuses very little in the film. Subsequently, the time and temperature sensitive polymerization and cross-linking reaction, referred to as post-bake, can be performed under the conditions that cross-link the exposed areas while leaving the remainder soluble in the developer solvent.

1.4 Templates for Photonic Crystals

The fabrication procedures discussed above are all capable of creating the structure geometries that show interesting electromagnetic responses when used as photonic crystals. But, these methods typically rely on materials that only have a moderate refractive index of 1.5 or thereabouts. It is desirable to fabricate photonic crystals with high refractive index materials that are capable of exhibiting complete photonic band-gaps [41]. However, it is difficult to directly pattern high dielectric materials so an alternative is to use the low refractive index photonic crystals as templates for infilling with materials that have higher refractive indexes [42,43]. This templating procedure is also useful for adding materials that have optical functionality, such as fluorescent emitters. Furthermore, the combination of creating an appropriate template which is then infilled by a controlled amount of another material represents a flexible way to fine tune the distribution of dielectric material, which controls the electromagnetic properties of the photonic crystal. The original template can optionally be removed or at any step an etching procedure can be used to selectively remove one of the materials. The multiple combination of infilling and etching gives a huge number of possibilities for obtaining different final structures based on the a single initial starting template.

## 1.5 Infilling Templates

The various methods that can be used to infill photonic crystal templates can be divided in to two categories, liquid-phase deposition and gas-phase deposition.

## 1.5.1 Liquid-Phase Infilling

Solvent casting [44] is a simple liquid-phase method where a solid material is dissolved in a solvent. The mixture is then infiltrated into the pores of the template and the solvent evaporates while the solid reforms inside the template. Another liquid-phase technique is the application of sol-gel chemistry [44,45]. A solution including the sol-gel precursors is introduced into the template and the sol-gel process deposits layers of solid material on the template surface. Titanium dioxide shells were formed around the colloids in a colloidal crystal using a sol-gel method [20]. Upon etching the colloids, the titanium dioxide shells, with a refractive index of ~2.2, exhibit strong photonic stop-gap effects. The final example of a liquid-phase process is electro-deposition [46,47]. In electro-deposition, the deposition typically starts at the substrate, which must be conductive, and proceeds upwards through the template. This bottom-up deposition is different than the conformal deposition, previously discussed. Electro-deposition is well-suited to making several layers of material inside the template, each layer having a different composition. Electro-deposition has been used to deposit zinc oxide [48] as well as copper oxide [49] into colloidal and SU8 polymer photonic crystal templates, respectively.

1.5.2 Gas-Phase Infilling

Gas-phase deposition typically introduces gas phase precursor molecules that react on the template surface to deposit a solid material. This process is called chemical vapor deposition [50] and there is a very wide range of available precursors that form many different solids. The challenge with chemical vapor deposition is that often the reaction needs to take place at a temperature that is too high for the process to be

compatible with a polymer template. But, it is possible to overcome the temperature limitation by first replicating the template with a material that can better withstand high temperature. This replication can be performed at a temperature compatible with the template. An example of such a procedure is the low temperature chemical vapor deposition of silica on an SU8 template [51].

Another challenge with chemical vapor deposition is that the reaction needs to occur slowly enough so that the precursors can diffuse into the depth of the template and the by-products can diffuse back out. Otherwise, the rate of reaction is not uniform throughout the template, resulting in final structure that is no longer periodic. To solve this problem, atomic layer deposition can be used. Atomic layer deposition [52] alternates between two rate limiting reactions so that only a monolayer or less of material is deposited in each cycle. This makes atomic layer deposition very well suited for depositing precise amounts of dielectric material on to a photonic crystal template.

## 1.6 Characterizing Photonic Crystals

Many methods exist for characterizing photonic crystals [53]. These range from standard imagining techniques, such a optical and scanning electron microscopy to non-standard techniques that take advantage of a photonic crystal's electromagnetic properties.

## 1.6.1 Optical Microscopy

Typical photonic crystals have feature sizes on the order of visible light, which prevents optical microscopy from revealing the fine details inside the periodic unit cell of

the photonic crystal. However, optical microscopy is capable of imaging larger scale features, such as drying cracks in colloidal crystals. Confocal microscopy [54] can be used to investigate the interior of photonic crystals. In this case, an index matching fluid with a fluorescent imaging dye can reveal defects within the photonic crystal. The confocal microscope is somewhat better than the optical microscope at resolving fine details, but other techniques are preferable.

1.6.2 Scanning Electron Microscopy

Scanning electron microscopy easily resolves the fine details within the unit cells of photonic crystals but information is only available from exposed surfaces. Fracturing a photonic crystal permits one to image the cross-section, at the fracture surface. However, this surface is often distorted and jagged as a result of the fracture [54]. Using focused ion-beam milling, a clean cross-section of a photonic crystal can be obtained. This is a good method to determine the level of uniformity in the structure, as a function of depth. However, focused ion-beam milling can be time-consuming and satisfactory information is often attainable by simply fracturing the sample and using a scanning electron microscope.

1.6.3 Diffraction Spots

As a photonic crystal is a periodic arrangement of dielectric material, it will readily diffract an incoming beam of light into numerous diffraction spots. If the incident beam is monochromatic, such as a laser, then the symmetry and the direction of the diffracting beams can reveal details about the periodic spacing and the symmetry of the photonic

crystal [55]. The refractive properties of the photonic crystal to air interface make it difficult to extract spacing information in the direction perpendicular to the surface. However, spacing information is easily obtained for the directions parallel to the surface. A simple application of Bragg's law, when the wavelength and beam angles are known will provide the pitch of features on the photonic crystal surface.

1.6.4 Optical Characterization of Photonic Crystals

The optical response of photonic crystals are commonly characterized by transmission, reflection, and light emission measurements [41]. The majority of these characterizations only measure the light propagating in a single direction, normal to the surface of the photonic crystal. When the refractive index contrast is comparatively weak, as in the case of a polymer photonic crystal, the light traveling in the normal direction is mainly affected by the variation in the refractive index in this direction [56]. This variation corresponds to the (111)-direction in vertically-deposited colloids, so that light is reflecting from the (111)-planes. The planes in other orientations typically contribution little towards the reflection and transmission data, unless the refractive index contrast is sufficiently high. If the refractive index is high then electromagnetic modes in the off-normal direction will significantly couple with the light, causing large decreases in the transmitted light. These large dips in the transmission occur because the light is diverted into off-normal directions that are not collected in the transmission and reflection measurements [57]. In order to fully examine the coupling of a photonic crystal's electromagnetic modes it is necessary to collect the light from a range of exit angles and to also use a range of incident angles when probing a photonic crystal.

Comparatively few studies [58-61] interrogate the off-normal directions, because it is difficult to obtain reliable data when the probe or exit beams make arbitrary angles with the photonic crystal surface. Furthermore, the theoretical analysis of light propagation inside the photonic crystal and the interpretation of experimental results are greatly complicated when arbitrary measurement angles are employed.

Optical characterization of the electromagnetic modes in a photonic crystal fall into two general categories. The first category uses an incident probe beam that carries a range of wavelengths and typically has a small numerical aperture so that most of the photons are traveling at nearly the same incident angle. The photons impinge on the sample, interact with it, and then are collected by a detector, placed so that only photons traveling at a certain angle are collected. Analysis of these probe beam measurements are complicated because light not only propagates through the photonic crystal, but it must first attempt to couple into and couple back out of the structure. Typically the probe beam and detected beams are well described by plane waves that form the electromagnetic modes of free space. But, complexity arises as the beams transition across the surface of the photonic crystal surface because inside the crystal the propagating electromagnetic waves must couple into the modes of the photonic crystal [62].

The second category of measurement, emission collection, relies on collecting light generated by emissive species, such as a fluorescent dye, embedded within the photonic crystal [63]. The rate of photon generation from the embedded emitters will follow Fermi's Golden Rule, which states that the rate is proportional to the density of electromagnetic modes. This means that we should expect changes in the fluorescent

lifetime of emissive molecules embedded withing the photonic crystal . For energy ranges where the density of modes is below that of the free-space density of modes the lifetime will be longer. Similarly, an increased density of modes results in a shorter fluorescent lifetime. Placing an emitter into a photonic crystal so that parts of the free-space emission wavelengths overlap a band-gap while other parts of the emission wavelengths are just outside the band-gap edge can cause the emission spectrum to be radically altered. In this case, emission that is now forbidden from because of the band-gap would tend to be emitted at the wavelengths just out-side the band-gap.

Collecting the angle-resolved emission of light, generated from within the photonic crystal, provides a mechanism to measure the distribution of the electromagnetic modes [64]. The intensity of light at a certain angle will be larger when more modes couple the light out in that direction. This method does not need to worry about the coupling of light into the photonic crystal because the detected photons are created inside. However, the coupling of light from inside the crystal into the free-space modes that are impinge on the detector must still be accounted for. Compared to the previous incident probe beam method, the emission collection method has a simplified analysis and more readily provides data about the electromagnetic mode distribution. Ultimately, it may not be possible or desirable to incorporate emissive species within a photonic crystal so both of the methods have can be useful.

1.7 Calculating Electromagnetic Properties of Photonic Crystals

There are a number of methods for calculating the electromagnetic response from photonic crystals [41]. The choice of which method is most suitable depends on

the type of data required.

### 1.7.1 Transfer Matrix

For simple normal direction reflection and transmission data from low refractive index photonic crystals it is sufficient to use a transfer matrix approach [56,65,66]. Here, the crystal is approximated as a series of homogeneous layers, parallel to the substrate, with each layer having an appropriate effective average refractive index. Analysis of angle resolved optical measurements requires more suitable models with which to compare and interpret the data. Transfer or scattering matrix methods that take a layer by layer approach are not well suited to model coupling and propagation at arbitrary angles.

### 1.7.2 Vos Model

Light which propagates a relatively far distance through a low quality photonic crystal can be appropriately described by the Vos model [58,61,67]. The assumption is made that the photons travel as though they are diffusing through the structure, with special consideration given to reflection from the periodic planes. However, the Vos Model does not provide a good fit to the data when light travels relatively short distances inside the photonic crystal, such as when fluorescence emission occurs near the surface.

### 1.7.3 Finite Difference Time Domain

The most general method to model an electromagnetic system is by propagating

the waves using Maxwell's Equations in a finite-difference time-domain simulation [68]. The entire problem space is subdivided into small cubes, no larger than 10% of the shortest wavelength of interest. Maxwell's equations are applied to the current fields to calculate the new fields after a tiny time-step into the future. This is an iterative process that is only appropriate for small computational volumes and short time scales because of the large amount of computational effort required. Otherwise, finite-difference time-domain calculations place very few restrictions on the types of problems that can be calculated. For a wide variety of structures and incident electromagnetic waves one can calculate the resulting electromagnetic fields. But, it is important to understand some of the limitations of the finite-difference time-domain method. One should realize that the calculated fields are only a good approximation to the actual system under study, and the approximation becomes worse as the refractive index contrast of the photonic crystal increases. An excellent finite-difference time-domain package [69] is provided as open-source software by researchers at the Massachusetts Institute of Technology. This package is very flexible and integrates well with other software.

1.7.4 Eigenmode Decomposition

Another useful calculation method is the eigenvalue and eigenmode decomposition of the electromagnetic waves in a unit cell of a photonic crystal [70]. This calculation assumes that the photonic crystal fills all space, to infinity, and it provides the field distribution for the electromagnetic modes and the energy of the photons contained in that mode. As the calculation does not account for any surfaces, the resulting modes are only applicable withing the bulk of the photonic crystal. Another method, such as a

18

finite-difference time-domain calculation, would be required to investigate the affect of surface interfaces. However, eigenmode calculations are standard for describing the properties of a particular photonic crystal structure. Typically, one calculates the mode along the edges of the first Brillouin zone so their energies may be plotted, as a function of the Bloch wave-vector. This produces a photonic band diagram. Such band diagrams are useful for identifying both complete and partial band-gaps. Another type of calculations involves calculating a very large number of modes, where the Bloch wave-vector is uniformly distributed in the inverse wave-vector space. This calculation can reveal the density of electromagnetic modes and is a more reliable method of identifying the band-gaps and energy ranges with significantly enhanced or reduced density of electromagnetic modes. An excellent open-source software package [71] for calculating the  electromagnetic modes is provided by researchers at the Massachusetts Institute of Technology.

1.8 Input Data for Calculations

A reasonable representation of the photonic crystal structure must be input into any model. In the case of interference lithography a constant intensity surface of the calculated interference pattern suffices. However, conformal material deposition methods such as atomic layer deposition create complicated surfaces not amenable to analytic treatment. For a subset of photonic crystals, with the required symmetry, a method [72] partially address the issue of structure determination for photonic crystals subjected to conformal deposition. However, the procedure is a complicated and not applicable to the general case. The lack of a generally applicable method to determine

structure resulting from conformal deposition is a hindrance when designing and

modeling photonic crystals fabricated using conformal deposition methods.

# CHAPTER 2

# DIRECT LASER WRITING[a]

2.1 Introduction

Direct laser writing is a versatile method of recording any type of pattern, within some resolution limit, into a photo sensitive film. In direct laser writing, a laser beam is brought into a tight focus within a photo sensitive film. Polymerization only occurs at the focal point, where the intensity is sufficiently high to cause an appreciable amount of two-photon absorption. The focal point is then translated such that a three-dimensional pattern is directly drawn into the film.

2.2 Fabrication of Woodpile Photonic Crystals

The woodpile structure [73] consists of 4 alternating layers of parallel rods. The first and third layers have their rods perpendicular to the second and fourth layers. Relative to the first layer, the third layer is translated in the plane by half of the rod spacing. Likewise, relative to the second layer the fourth layer is translated in the plane by half the rod spacing. The pattern repeats as more layer are added and the result bears a similarity to a pile of logs, hence the name woodpile. Calculation of the photonic bands reveals that this structure has a significant band-gap if fabricated with materials of sufficient dielectric strength. The goal was to fabricate a woodpile photonic crystal with direct laser writing.

---

a   This chapter contains material that was previously published in reference #54. The copyright owner has provided permission to reprint this material here.

2.2.1 Methods and Materials

The substrate used was a standard type-1 microscope cover-slip with a thickness of about 170 microns. Several drops of the 2020 SU8 formulation, manufactured by Microchem, was deposited on the cover-slip which was mounted in a spin coater. An initial spin speed of 500 RPM was held for 10 seconds and then a final speed of 2000 RPM was held for 30 seconds. Spin speeds were ramped up at a rate of 300 RPM per second. The cover-slip was then pre-baked, to remove excess solvent, using a hot plate. First, 2 minutes at 65 degrees C then the cover-slip was transfered to another hot plate, at 95 degrees C, where it remained for 5 minutes before being removed.

Direct laser writing was performed using a scanning confocal microscope (Lecia SP1) outfitted with a Ti:Sapphire laser operating at 780 nm. The substrate was mounted on the stage and leveled. Immersion fluid was used on the 63 times objective lens. The beam expander was set to 3 times, the resolution to 2048 scan lines by 2048 pixels, and a scan rate of 200 Hz was used. Tests were run at various gain settings of the electro-optic modulator, which controlled the intensity of the laser beam entering the objective lens. The gain setting used was that just below the threshold for laser induced film damage, which occurs due to the vaporizing of the monomer or residual solvent in the film. Four settings of the gain were employed in making four woodpiles. These gain settings were 25%, 50%, 75%, and 100% of the square of intensity, where the 100% level is just below the damage threshold. A curve of intensity versus gain setting, obtained with a power meter using the 10 times objective, was used to determine the required gain setting from the desired intensity.

The pattern of rods, for each of the four unique layers, was programed into a text

file that defines each rod as a region of interest within the control software of the

confocal microscope. To write the first layer of rods, the region of interest file was

loaded and 6 scans were performed, where each subsequent scan was performed at

166 nm above the previous scan. The rods were defined to be 1 micron in width with 1

micron of air separating adjacent rods. The electro-optic modulator does not allow the

laser to pass except when scanning within a region of interest. The next layer's region of

interest file was loaded and the process was repeated until 20 layers of rods were

written.

The sample was then removed and post-bake was performed on a hot plate.

First, 2 minutes at 65 degrees C then the sample was transfered to another hot plate, at

95 degrees C, where it remained for 5 minutes before being removed and allowed to

cool. The sample was immersed into propylene glycol monomethyl developer for 5

minutes and rinsed in isopropanol. The sample was then imaged in a scanning electron

microscope.

2.2.2 Results and Discussion

Of the multiple structures fabricated, only the structure made with 50% setting of

the squared intensity resulted in a good quality structure (Fig. 1). The 75% squared

intensity structure was found to be over-polymerized (Fig. 2) while the 25% structure

was washed away by the developing process. Woodpile structures were attempted for

rod widths and thicknesses less than 1 micron, but the first successful results only

occurred when the spacing was 1 micron.

Although the resulting structure with 1 micron spacing was of high quality, the

spacing is too large so that any photonic crystal effects would occur at wavelengths in the infrared spectrum. These effects would not be easily measured by our available spectrometers which operate in the visible and near-infrared, at wavelengths shorter than 1.6 microns. Similarly, the majority of interesting luminescent species operate in the visible and near infrared spectrum which would make them unsuitable for incorporation into a woodpile with 1 micron spacing. Furthermore, the high quality woodpile could only be reliably fabricated when the lateral dimensions were small. Attempts to increase the lateral dimensions up to 200 microns per side failed. This failure was likely due to variances in the intensity distribution at the focal point as the laser is scanned across the field of view, resulting in vaporization damage. For these reasons, the making of photonic crystals by the sole use of direct laser writing was not continued. If direct laser writing of photonic crystals were to be continued it is recommended that improved control software be obtained, as the semi-manual method of using region of interest text files is limiting and error prone. Furthermore, better results would be possible if the translation of the focal point was done with piezoelectric stages rather than scanning mirrors. Lastly, a dedicated direct laser writing apparatus could likely be more highly optimized for the task as compared with the multi-user apparatus that was used.

2.3 One-Step Fabrication of Channels in Holographic Photonic Crystals

Interference lithography is capable of recording defect-free patterns into photo-resist. However, incorporating engineered defects, which could function as waveguides, requires a patterning procedure capable of writing non-periodic features. Direct laser

24

writing is ideal for adding non-periodic features to the defect-free large scale patterns produced by multi-beam interference lithography. The overall periodicity of the photonic crystal is defined by the high-throughput method while the low-throughput method performs the complementary task of adding a relatively small volume of non-periodic features.

## 2.3.1 Methods and Materials

As both patterning methods can use the same SU8 photo-resist, the original approach was to first record a latent image, of dissociated acid, using interference lithography and then use direct laser writing to add features to the latent image. Alignment of the defects with the host photonic crystal was performed using coumarin-6 fluorescent dye, which shifts its emission wavelength according to the local pH. This permitted imaging the latent image of the host photonic crystal and the added defects, as they were being written. Subsequently, the photo-resist was then post-baked and developed as discussed in section 2.2.1.

## 2.3.2 Results and Discussion

Direct laser writing generated acid images that generally had significantly higher contrast compared to that created with interference lithography. The typical result was defect structures that were significantly more robust than the host photonic crystal so that the host photonic crystal was severely distorted in the vicinity of any defects (Fig. 3). This effect was a result of the differential shrinkage, due to different cross-linking densities and subsequent development stresses, in the differently patterned regions.

## 2.4 Two-Step Fabrication of Channels in Holographic Photonic Crystals

### 2.4.1 Methods and Materials

The alternate approach to one-step fabrication was to backfill trimethylol propane triacrylate monomer into a fully developed SU8 photonic crystal, created using interference lithography. The monomer also contained BODIPY, an imaging dye, and the two-photon sensitizer AF-350. Defects were added to the host photonic crystal by polymerizing the monomer via direct laser writing. The excess monomer was then removed by rinsing with ethanol. The structure could now be used for further processing. The polymer photonic crystal was replicated in silicon using chemical vapor deposition. The polymer template was subsequently removed by baking at 410 °C. The silicon photonic crystal was subjected to focused ion-beam milling in order to examine the cross-sections at the sites of the added defects.

### 2.4.2 Results and Discussion

The confocal images, in Figure 4, show that the polymerized defects appear to have well defined boundaries that roughly match the intended sizes of 4, 2, 1, and 0.5 microns, respectively. However, the scanning electron micrographs of the cross-sections revealed channels with very roughly defined boundaries. This is likely due to the combination of the resolution limits of the photo-resist, trimethylol propane triacrylate, combined with the somewhat severe procedure used to to remove the polymer. Overall, this experiment successfully demonstrates that interference

lithography can be coupled with direct laser writing to add defects to large scale photonic crystals. The resulting structure can then be used as templates for further processing [54].

## 2.5 Conclusions

It has been demonstrated that direct laser writing is a versatile method to precisely initiate polymerization of any three-dimensional pattern, within the resolution limits. The effective reliable resolution limit for the confocal apparatus employed appears to be on the order of 0.5 micron. But, this could likely be improved by refining the protocols and converting the apparatus to a single purpose device where the optics and motion control is dedicated to direct laser writing. At the expense of long processing times, large photonic crystal patterns can be formed. However, defects can be relatively quickly and easily added to photonic crystal patterns by using direct laser writing.

# CHAPTER 3

# HIGH QUALITY FLUORESCENT PHOTONIC CRYSTALS[b]

## 3.1 Introduction

Photonic crystals structures with periodicity on the order of the wavelength of light, can be particularly useful for light emitting diode (LED) structures. Most of the emission in ordinary LEDs is trapped by internal reflection but photonic crystals can direct more light out of the structure. Previous work has concentrated on using two-dimensional photonic crystals to scavenge photons from LEDs [74,75], but three-dimensional crystals have the potential to more significantly control electromagnetic emission and propagation. In this work, we have fabricated an fcc fluorescent photonic crystal (FPC), composed primarily of ruthenium tris-bipyridine $[Ru(bpy)_3]^{2+}(PF6^-)_2$, (RuBpy), a molecular semiconductor which can serve as the active emitter in LEDs.

There are many promising reports [76-81] of emitters introduced into three-dimensional photonic crystals, but the characterization and modeling of subsequent results predominately focuses on a limited set of the possible directions in which light exits the structure. We have performed angle-resolved spectroscopy encompassing 76% of $2\pi$ sr on one side of the FPC and have observed highly anisotropic emission that is attributed to the FPC optical modes and dispersion. These phenomena have not been previously reported and are explained in the context of an analytic model incorporating two plane-waves coupled by diffraction from a single Bragg plane. Our results identify emissive enhancements arising from two distinct phenomena within the

---

b   This chapter contains material that was previously published in reference #7. The copyright owner has provided permission to reprint this material here.

photonic crystal. The magnitudes of these effects relative to each other and to the background bulk-like emission are clearly demonstrated over 76% of 2π sr.

3.2 Methods and Materials

Fabrication of our FPC proceeds with polystyrene colloids grown into an fcc colloidal crystal via vertical deposition on a glass substrate. Atomic layer deposition of 10 nm alumina improves structural stability while negligibly affecting the photonic band structure [82]. RuBpy, dissolved in acetonitrile, is wicked into the interstitial pores. The solvent evaporates to form a solid RuBpy matrix. Reactive ion etching exposes the polystyrene colloids lying beneath the RuBpy over-layer. Finally, polystyrene is removed with toluene.

Scanning electron microscopy shows excellent structural order on the polystyrene template surface [Fig. 5(a)] and in the ion-milled FPC cross-section [Fig. 5(b)]. The lattice constant $a = 577 \pm 9 \ \mathrm{nm}$ , measured by surface diffraction with a 351 nm laser, gives an effective hard sphere diameter of $408 \pm 6 \ \mathrm{nm}$ , consistent with the nominal 420 nm colloid diameter. Normal incidence reflectance [Fig. 5(c)] peaks of the template and FPC occur at the expected positions and are consistent with other works [76-81]. The 50% FPC normal incidence reflectance and clear Fabry-Perot fringes (150 μm spot size), are indicative of a high degree of order. The ~20 layer thick FPC is transparent to the eye with ~75% transmission at 532 nm, corresponding to a mean free path of ~20 μm.

Solid-angle-resolved spectroscopy is used to measure the FPC emission patterns. The crystal-air surface is irradiated with a normal-incident 532 nm continuous-

wave laser beam at 30 μW focused to a 50 μm spot with 0.02 numerical aperture. A detector assembly collects fluorescent emission from the substrate side, within a 2.5º apex-angle cone. Collected emission is filtered to pass vacuum wavelengths $\lambda > 534 \ \mathrm{nm}$ and then focused into an optical fiber (randomizing the polarization) coupled to a spectrometer. The detector is positioned 15 cm from the sample and is mounted on 2 perpendicular motorized rotary-stages with rotation axes passing through the excitation volume. The θ-stage sets the detector angle relative to the FPC surface normal and the φ-stage sets the azimuth angle14. Measurement proceeds by sweeping θ from -75º to +75º, in 2º steps, for each φ from 0º to 180º, also in 2º steps.

Photo-bleaching reduces fluorescent intensity ~50% during the 6 hours of data collection. A correction is applied by normalizing each θ-sweep to the intensity collected at $\theta = \pm 1°$ (normal incidence). This corrected data is further normalized by making the θ-φ-integrated intensity equal for each λ, facilitating comparison of emission patterns at different λ. A reference dataset is similarly collected from a non-diffracting unstructured RuBpy film. Presented in Fig. 5(c) are the FPC and reference spectra, integrated over 76% of 2π sr and normalized in frequency space. These spectra show only minor deviations. This is consistent with the notion that a periodic dielectric structure serves to redistributes the electromagnetic modes present in free-space, shifting them from forbidden energy ranges or directions and placing them in nearby allowed ranges.

3.3 Results and Discussion

Very anisotropic FPC emission patterns are presented, for five representative λ, in Fig. 6(a)(i)-6(e)(i). The three-fold fcc symmetry is evident in the 2 sets of 3 bright arcs

30

in Fig. 6(e)(i). Such detailed and dramatic emission patterns from three-dimensional

photonic crystals incorporating fluorescent species have not been previously reported.

We compared our results with a model [58] for FPC emission. Fig. 6(a)(ii) is generated

by inserting our FPC parameters into the model and is directly comparable with Fig. 6(a)

(i). Agreement is found for the reduced intensity ring with a minimum at $\theta = 27°$. This

feature will be shown to be caused by the stop-gap from the $(111)$ planes parallel to

the FPC surface. Stark disagreement occurs for the three-fold symmetric reductions in

the model. Instead, slight intensity enhancements are observed which we refer to as

mode enhancements. We will show that these are due to the nature of the FPC optical

modes. The model [58] does not explain our data because it is based on photon

diffusion theory which requires a transport distance longer than the mean free path.

However, our mean free path is 3 times the FPC thickness.

Diffraction effects are predicted whenever the Bragg condition $\vec{k} - \vec{k}' = \vec{G}$ is nearly

satisfied [8]. An incident plane-wave wave-vector k is related to a diffracted wave-vector

$\vec{k}'$ by a reciprocal lattice vector $\vec{G}_{hkl} = (2\pi/a)(h\ k\ l)$ for Miller indices h, k, and l all even

or all odd. The magnitude $\|\vec{k}\| = \|\vec{k}'\| = 2\pi \varepsilon_{000}^{1/2}/\lambda$ where $\varepsilon_{000}$ is the average FPC dielectric

constant, calculated by assuming air spheres in a RuBpy matrix. Plane-waves inside the

FPC are related to those in air by conservation of the parallel component of momentum

across the FPC surface. Plots depicting the satisfaction of Bragg's Law are presented in

Figs. 6(b)(ii)-2(e)(ii), where the angles are directly comparable with data in Figs. 6(b)(i)-

6(e)(i). FPC emission features are unmistakably correlated with Bragg diffraction. As λ

decreases in the series, Figs. 6(a)(i)-6(e)(i), the $(111)$ stop-gap expands to larger θ

while the mode enhancements correlated with $(11\bar{1})$, $(1\bar{1}1)$, $(\bar{1}11)$ and $\{200\}$

31

diffraction move to smaller θ, resulting in a prominent hexagon-like pattern in Fig. 6(d)

(i). The FPC stop-gap positions for $\lambda = 560 \text{ to } 712 \text{ nm}$ are best matched with

$\varepsilon_{000} = 1.46 \text{ to } 1.42$ but the theoretical $\varepsilon_{000} = 1.50 \text{ to } 1.45$. This discrepancy may be

attributed to a reduced effective density of ~93% for RuBpy within the FPC, reasonable,

since the colloidal template likely frustrates densification upon solvent evaporation.

Assuming a position and dipole orientation independence for RuBpy absorption

and subsequent isotropic fluorescence, the emission pattern for a non-structured bulk

slab of RuBpy is expected19 to be proportional to $\cos\theta$. When structured into a FPC

the dielectric contrast is small, thus bulk-like behavior (BLB) dominates for k far from

Bragg planes and photonic crystal effects dominate for k near Bragg planes [3,4]. The

variations of the φ-averaged intensity versus θ, relative to the BLB, are presented in

Figs. 6(a)(iii)-6(e)(iii). The experimental curve was normalized to the expected BLB by

first equating the total θ-φ-integrated intensity, then dividing by the FPC to reference

spectra ratio [Fig. 5(c)] at each λ, and scaling by 0.85 to overlap the large θ and long-λ

portion of the data, beyond the diffraction cutoff where the FPC acts like a bulk slab.

Clear examples of BLB are seen for small and large θ in Figs. 6(b)(iii)-6(d)(iii) with other

features superimposed at midrange θ.

The final feature observed will be attributed to maxima in the electromagnetic

mode density. These enhancements border both sides of the stop-gap, have narrow ~5°

width and intensity ~15% above the BLB. Mode density enhancements are most clearly

seen in Fig. 6(b)(i) at $\theta = 19°$, on the stop-gap inner-edge, and in both Fig. 6(a)(i) at

$\theta = 46°$ and Fig.6(d)(i) at $\theta = 61°$, on the stop-gap outer-edge.

An analytical solution for the FPC emission is derived following an approach

similar to the dynamical diffraction theory of X-rays [6] but complicated by the non-negligible dielectric contrast. We assume two electric-field plane-waves $\vec{E}_p e^{i\vec{p}\cdot\vec{r}}$ and $\vec{E}_q e^{i\vec{q}\cdot\vec{r}}$ with wave-vectors $\vec{p}$ and $\vec{q}=\vec{p}-\vec{G}_{hkl}$, diffracted by a single Bragg plane defined by $\vec{G}_{hkl}$. Solutions are obtained from Maxwell's equations which are linear combinations, $\vec{E}=\vec{E}_p e^{i\vec{p}\cdot\vec{r}}+\vec{E}_q e^{i\vec{q}\cdot\vec{r}}$. This satisfies Bloch's Theorem requiring the solution be a product of a plane-wave $e^{i\vec{p}\cdot\vec{r}}$ and an amplitude $\vec{E}_p+\vec{E}_q e^{-i\vec{G}\cdot\vec{r}}$ periodic with the FPC. We have the following 2-vector system [6]:

$$(k^2 \varepsilon_{000}-\vec{p}\cdot\vec{p})\vec{E}_p+k^2 \varepsilon_{hkl}\vec{E}_q+(\vec{p}\cdot\vec{E}_p)\vec{p}=0$$

$$(k^2 \varepsilon_{000}-\vec{q}\cdot\vec{q})\vec{E}_q+k^2 \varepsilon_{hkl}\vec{E}_p+(\vec{q}\cdot\vec{E}_q)\vec{q}=0$$

The photon energy and magnitude of the free-space momentum are defined by $k=2\pi/\lambda$. $\varepsilon_{000}$ and $\varepsilon_{hkl}$ are respectively the average and the $G_{hkl}$-fluctuating components of the Fourier series expansion of the dielectric constant. For fcc air spheres in RuBpy, $\varepsilon_{000}=1.428$ and $\varepsilon_{111}=0.158$ at $\lambda=690$ nm. Non-trivial solutions require the matrix of coefficients to be singular. We obtain the dispersion relation

$$F_{TE}F_{TM}=0$$

where

$$F_{TE}=(k^2 \varepsilon_{000}-\vec{p}\cdot\vec{p})(k^2 \varepsilon_{000}-\vec{q}\cdot\vec{q})-k^4 \varepsilon_{hkl}^2$$

$$F_{TM}=F_{TE}+[\varepsilon_{hkl}^2/(\varepsilon_{000}^2-\varepsilon_{hkl}^2)](\vec{p}\times\vec{q})\cdot(\vec{p}\times\vec{q}).$$

This dispersion is a convenient product of the transverse-electric (TE) $F_{TE}$

( $\vec{E}\perp\vec{p}, \vec{E}\perp\vec{q}, \vec{E}\perp\vec{G}_{hkl}$ ) and the transverse-magnetic (TM) $F_{TM}$ contributions. It is

straight forward to obtain the dispersion surface, giving p and q, for a particular λ, and

then back-solve for a mode's $\vec{E}_p$ and $\vec{E}_q$ . The solution is limited to small dielectric

contrast, estimated as $\varepsilon_{111}<(5/36)\varepsilon_{000}\simeq 0.2$ derived for a stop-gap centered at ½ the

distance between the center and the edge of a {111} Brillouin zone face and requiring

the stop-gap not reach past ¾ that distance. This allows neighborhoods of k where

diffraction is only significant from no more than one Bragg plane. Also, k must be

sufficiently distant from any intersections of multiple Bragg planes [intersections of lines

in Figs. 6(a)(ii)-6(e)(ii)]. The solution will then apply to any single feature (stop-gap,

mode or mode density enhancements) observed at these k. Such features are identified

in the inset tables of Fig. 6.

Figure 7 describes the FPC optical modes where diffraction is only significant

from $\vec{G}_{111}$ and $\lambda=690 \text{ nm}$ , corresponding to Fig. 6(b). Both the TE and TM dispersion

surfaces have radial symmetry around $\vec{G}_{111}$ and mirror symmetry in the Bragg plane.

The magnitude and direction of p and q are obtained by starting from the origin and

$\vec{G}_{111}$ , respectively, and drawing vectors to a single point (representing one FPC mode)

on the dispersion surface. The $k\varepsilon_{000}^{1/2}$ radius circles centered at the origin and $\vec{G}_{111}$

depict an effective $\varepsilon_{000}$ -media with the Bragg condition occurring at the circle's

intersections.

The FPC optical modes describe light propagation and RuBpy fluorescence

34

emission within the FPC. Modes are related to the data because they must decompose into the plane-waves that ultimately impinge on the detector. Conversions from internal FPC propagation directions to those in free-space are obtained by conserving momentum parallel to the FPC surface. Momentum conservation is applied individually to both the plane-waves that comprise one FPC mode,

$$\|p\| \sin \theta_p = k \sin \theta_{p-air}$$

$$\|q\| \sin \theta_q = k \sin \theta_{q-air} \ .$$

To avoid total internal reflection at the FPC surface we must have

$$\|p\| \sin \theta_p < k$$

$$\|q\| \sin \theta_q < k \ .$$

Both the TE and TM dispersions (Fig. 7) have ranges of parallel momentum for which no modes exists, and thus no fluorescence emission should occur. These gaps in the $\vec{G}_{111}$ dispersion surface give rise to the stop-gap feature. The theoretical TE and TM stop-gap angular widths in free-space are plotted as horizontal over-bars in Fig. 6(a) (iii)-6(e)(iii), showing good agreement with the data.

The mode density versus parallel momentum, normalized to that of $k\varepsilon_{000}^{1/2}$ plane-waves, is plotted in Fig. 7. Adjacent to the vanishing mode density in the stop-gaps are pronounced maxima, recognized as Van Hove singularities [8]. According to Fermi's Golden Rule, the rate of RuBpy emission is proportional to the mode density [83]. Thus, corresponding peaks in emission should occur and are observed as mode density enhancements, adjacent to the stop-gap and ~15% higher intensity than the BLB. Consider the $(11\bar{1})$ Bragg plane, from the $\{111\}$ family but not parallel to the FPC

surface. The $\vec{G}_{11\bar{1}}$ dispersion for $\lambda = 690\ nm$ [Fig. 7(inset)] is identical to the $\vec{G}_{111}$

dispersion but tilted by $70.5° = \arccos{}^{1}\!/_{3}$ from the FPC surface. A forbidden range of

momentum parallel to $(11\bar{1})$ occurs, but contrary to the $\vec{G}_{111}$ case, modes exist for all

values of momentum parallel to the FPC surface less than $\sim k\varepsilon_{000}^{1/2}$. This is

demonstrated by the inability to draw a line perpendicular to the FPC surface which

does not intersect the $\vec{G}_{11\bar{1}}$ dispersion. This explains why strong intensity suppressions

only occur for $(111)$ diffraction. Diffraction from the remaining $\{111\}$ and the $\{200\}$

planes are instead associated with mode enhancements which are clearly seen in Fig.

6(e)(i). Mode enhancements arises because the $\vec{E}_{p}$ and $\vec{E}_{q}$ plane-waves comprising

one mode may differ significantly in how strongly they are confined to the FPC. Plane-

waves incident on the FPC surface at small angles to the normal are weakly confined

relative to those at large angles where strong Fresnel reflections or total internal

reflection may occur. For Bragg planes not normal to $(111)$, p and q for a single mode

may make quite different angles [Fig. 7(inset)] with the FPC surface, resulting in $\vec{E}_{p}$

and $\vec{E}_{q}$ having significantly different energy flux across the surface. Since a mode's

$\vec{E}_{p}$ and $\vec{E}_{q}$ are coupled, the amplitude of the leaky plane-wave is compensated from

the more confined plane-wave and should result in increased intensity in the leaky

direction. This is observed as mode enhancements, where intensity is up to ~50%

above the BLB. The effect should be stronger when $\vec{E}_{p}$ and $\vec{E}_{q}$ are strongly coupled,

which occurs when they have comparable amplitudes. Figure 7 plots the amplitude

fraction of the smaller magnitude plane-wave, as a measure of coupling, versus

momentum parallel to the $\{111\}$ Bragg plane. Coupling is strongest near the Bragg

condition, where the largest mode enhancements are observed but are absent for

diffraction from $\vec{G}_{111}$ because here $\|p\|\sin\theta_p = \|q\|\sin\theta_q$ so both plane-waves are

similarly confined. Finally, we observed that BLB occurs at data points far from any

Bragg planes. Here the DOM is practically that of $k\varepsilon_{000}^{1/2}$ plane-waves and coupling is

weak. Consequently, these modes are very much like a plane-wave, giving rise to the

BLB in the data.


3.4 Conclusions

In summary, solid-angle resolved spectroscopy captured highly anisotropic

emission patterns that are explained by our approximate analytical solution. The distinct

mode enhancements and mode density enhancements are separately identified and

direct geometrical insights are provided that are not easily extracted from numerical

solution methods [81]. These insights may enable LED designs with more efficient or

customized emission patterns.

# CHAPTER 4

## MODERATE QUALITY FLUORESCENT PHOTONIC CRYSTALS

4.1 Introduction

The study of high quality fluorescent photonic crystals, discussed in the previous chapter, also yielded moderate quality photonic crystals with emission patterns that were not well explained by the presented model. However, the model of Vos [58], also discussed in the previous chapter, was a better fit for the moderate quality photonic crystals compared with the high quality structures. A physically justified modification of the Vos model produced results that were a reasonable fit to the emission patterns obtained for the moderate quality fluorescent photonic crystals. This new model and our observations is the topic of this chapter.

4.1.1 Justification for a Modified Model

The Vos model was derived to describe the propagation of photons that are generated deep within a photonic crystal and then exit at the surface, where the distance traveled is sufficient to cause appreciable diffraction from the ordered Bragg planes. The propagation of these photons is assumed to behave as if the photons were diffusing throughout the structure. The Vos model also assumes that the Bragg diffracted photons are redirected to deep within the photonic crystal, so it is as if these photons never made any progress towards the surface. However, if a photon travels to a point close to the surface and is then Bragg reflected, the photon acquires a new trajectory where the probability of being Bragg reflected again is the same as when it

was in the original trajectory. This is because the photon keeps the same angle with respect to the normal of the Bragg plane, in which the reflection is assumed to be specular. Reconsider the case of the photon that was near the surface when it was reflected by the Bragg plane. This reflected photon is just as likely to be redirected towards the surface as it was to be reflected originally, but the path to the surface is now very short, which significantly increases the escape probability.

4.2 The Modified Model

The Vos model can be modified to better account for the photons that are Bragg reflected. This modification makes it very difficult, if not impossible, to derive an analytical expression that describes the emission pattern. Hence, a numerical simulation is performed that retains the essential aspects of the Vos model while better accounting for reflected photons.

The depth within the photonic crystal is divided into a finite number of layers. In each layer the propagation directions are divided into states that represent a number of photon, traveling within a certain solid angle at a certain depth within the crystal. The portions of solid angle is equal for each state. By the translational symmetry in the plane of the photonic crystal, the photon distribution only depends on the depth and direction. The current distribution of photons is used to calculate the next distribution of photons at a small increment of time into the future.

The rules for calculating the next state are as follows: 1) Photons, all traveling at the same speed in the crystal, continue in the direction they are traveling unless they undergo an event that changes their direction. 2) Bragg reflection occurs with a certain

probability that is dependent on the quality of the photonic crystal and the propagation direction. 3) Fresnel reflections occur at the interfaces of the photonic crystal. 4) a finite scattering probability exist for scattering into a random direction. 5) the generation of photons due to fluorescence emission is assumed to be constant and uniform throughout the depth of the photonic crystal.

Any initial state suffices to start the simulation because eventually a steady state distribution of photons will emerge where the escaping photons balances the generated photons. At this steady state, the photon distribution will cease changing and the calculated emission pattern can be compared with the emission pattern measured by angle-resolved spectroscopy.

4.3 Fabrication and Characterization of Fluorescent Photonic Crystals

The procedure detailed in chapter 3 was used to fabricate and characterize these moderate quality fluorescent photonic crystals.

4.4 Model Parameters

The modeled photonic crystal was divided into 20 layers in the vertical direction. Each layer was further divided into about 16500 states, each containing photons propagating in one direction with a solid angle of approximately $(0.5°)^2$. The reflection of each (111)-plane was set to 0.058 so that the overall reflection is about equal to 70% $[(1-0.58)^{20} = 1 - 0.7]$. The value of 70% reflectance for the stop-gap was justified as being within the range of experimental reflectance measurements, taken across the sample. Furthermore, 70% reflectance was employed in the Vos model. The reflectance

of the (100)-planes was set to 75% of the reflectance of the (111)-planes. The value of 75% corresponds with the square of the relative areal packing density for sphere on a face-centered cubic lattice, which seems to be a reasonable choice. However, a more throughout investigation is warranted to determining what the (100)-reflection should be set to. The random scattering rate was set to 2% per time-step which would result in the reasonable value of about 67% transmission through the photonic crystal, for a normally incident beam that is not affected by the Bragg reflections. The angular dependence of the reflectance was the same as that used in the Vos Model, which is a squared Gaussian that has a frequency width of about 10% of the center stop-gap frequency.

4.5 Results and Discussion

Figure 8 depicts the angles for collecting the data and shows how these angles correspond to the angle resolved emission patterns that are plotted in a polar format. Figure 9 shows the emission of the high quality fluorescent photonic crystal and the emission obtained using the Vos model. These emission patterns are very different from each other. Furthermore, both of these patterns are also differ (Figs. 10, 11, and 12) from the experimental data collected for the moderate quality fluorescent photonic crystals and the new model, which better accounts for photons reflected in Bragg planes.

There are three moderate quality crystals which are fabricated with three different sizes of colloids, 400 nm (Fig. 10), 330 nm (Fig. 11), and 466 nm (Fig. 12). From normal incidence reflectance data at various points across each sample, there appeared to be a hierarchy of quality in these three crystals. The 400 nm appeared to be lowest in

quality. The 330 nm crystal was the next highest and the 466 nm was highest quality. A similar trend is seen in how well these three moderate quality crystals fit the new model.

The 400 nm crystal is the poorest fit to the new model but the hexagon shaped stop-band centered about θ=45° and the 6 slightly darker bands that extend outwards past θ=75° are also present in the new model. It is noteworthy that of all the photonic crystals measured, this lowest quality specimen is the most similar to Vos model, where a pronounced brighting occurs between the stop-band and θ=0°. But, the dark bands of the Vos model are very subdued on the 400 nm crystal.

The 330 nm crystal has a reasonable fit with the new simulation. But the 466 nm crystal appears to fit the new model quite well. Figure 12 shows how both data sets have the fine bright arcs, 3 due to Bragg reflections in the (111)-planes not parallel to the surface and the other 3 due to Bragg refection in the (100)-planes. Such reflections only appear in the new model because the depth at which the photons are at is well accounted for as they are reflected back and forth by the Bragg planes.

Close inspection of the high quality 466 nm crystal in both Figure 9 and Figure 13 reveals that both edges of the stop-gap, the darker ring at about θ=35° to 40°,is bordered be a thinner region where the intensity is noticeably higher than the adjacent background levels. These features are manifestations of enhancements in the density of modes, causing the rate of emission into these directions to be similarly enhanced. As neither the Vos model or the new model take into account the true nature of the electromagnetic wave, neither model exhibits these features. This makes it appropriate to refer to the 466 nm crystal as being of high enough quality, such that the uniquely photonic effect of increased mode density at the band-edge can be observed.

4.6 Conclusions

Polar plots of the experimental angle-resolved emission data for moderate quality fluorescent photonic crystals compares favorably with the new model of emission. The new model is based on the Vos model, but modified to better account for the distribution of photons as a function of depth within the crystal. The model appears to be limited to describing photonic crystals which fall into a range of moderate quality. Poorer quality structures tend to fit better with the Vos model. The higher quality structures, which exhibit purely photonic effects, need to be described in terms of the altered electromagnetic modes, as was done for the high quality photonic crystals in chapter 3.

**CHAPTER 5**

**FOUR CIRCLE DIFFRACTOMETER**

5.1 Introduction

The successful collection of scientifically interesting angle-resolved data using a two-circle diffractometer, discussed in chapter 2, justified the expansion of our ability to collect angle-resolved data from photonic crystals. A four-circle machine allows the simultaneous specification of any incident angle for a probe beam and any exit angle, at which the detector collects light from the sample. The original 2-circle diffractometer was a combination of two stepper motors mounted perpendicular to each other. A significant amount of care was used to ensure that the detector was consistently focused on the center point, where the rotation axes of the two motors intersect, or rather, where the distance between these axes is a minimum. The sphere of confusion was estimated to be on the order of 2 millimeters.

5.1.1 Limitations of the Previous Diffractometer

Attempts were made to add two additional stepper motors in order to create a diffractometer with four circles. However, repeated attempts failed for numerous reasons. First, the motors were somewhat weak so only a very limited payload could be carried. This excluded mounting the detector and excitation lenses on translation stages, which would greatly assist in aligning the beams. The second reason is the increase to 4 stepper motors tended to cause geometrical obstructions for either or both of the excitation and detector beams over a significant range of angles. The final, and

most important reason to abandon our in-house 4-circle diffractometer was due to the excessively large sphere of confusion and difficulty in aligning the optical beams. There are too many degrees of freedom that need to be fixed when 4 motors are required to rotate about a single point in space while keeping the two lenses focused on the center point.

5.1.2 Commercial Diffractometer

A decision was made to obtain a commercial 4-circle diffractometer, manufactured by Huber. The commercial system would come with a fixed alignment that provides a specified sphere of confusion of 10 microns for the four circles. Also, the one movable arm has a maximum payload of over 10 kilograms while the payload of the fixed arm is essentially infinite. This allows great flexibility in mounting excitation and detector systems. Furthermore, the large payloads permit the addition of stages to easily align the optics towards the center point of rotation. The inclusion of a telescope, for visualizing the sample position, greatly aids in aligning both the optics and the sample.

5.2 Materials and Methods

5.2.1 Stages for Mounting and Aligning Optics

Both the movable and the fixed arms of the diffractometer were outfitted with a stage setups that facilitates aligning the optics. As a frame of reference, the z-direction is vertically up, the x-direction moves towards the center point and the y-direction is

perpendicular to both x and z.

On the fixed arm (Fig. 14), one ball bearing stage moves in the x-direction. Mounted on to the x-stage, a  pair of dovetail stages move in the y direction. Concurrent movement of these two stages will translate in the y-direction but movement of only one of these stage causes the direction of the optic to change angle. Mounted onto each of the y-stages is a dovetail stage that moves in the z-direction. Again, concurrent movement of both z-stages constitutes a translation while only moving a single stage amounts to a change in angle of the optic. Mounted to each z-stage is a post and both posts are affixed to rail that is aligned in the x-direction. Upon the rail, the optical assembly is mounted. These stages permit the optical beam to translate in the three perpendicular directions in space and also allow the two degrees in freedom in setting the angle of the beam. Such a system facilitate all the necessary motions for aligning the optic that is mounted on the rail.

On the movable arm (Fig. 15), an integrated three-axis dovetail translation stage is affixed. A mounting platform is mounted onto the translation stage. Another mounting platform is above the first and several screws permit the top platform to be pointed, with two degrees of freedom, relative to the bottom platform. Mounted to the top platform is the optical assembly. The optical assembly can be translated in three directions and pointed in two, fully facilitating alignment.

## 5.2.2 Optical Alignment

The optical beams need to be aligned so that they both focus on the center point and both make correct angles with the frame of reference. The alignment needle is

mounted into the sample mount and the movable arm should be exactly opposite of the fixed arm. First, the needle is aligned with the center of the chi-axis, which is accomplished when the needle does not translate, but only rotates, when the chi-axis is rotated. Next, the optical beams are focused so that the focal points fall on the needle. Rotation of the phi-axis to the positions of 0°, 90°, 180°, and 270° will readily reveal if the optical beams are directed through the center point. Simultaneously, the height of the both optical assemblies are set equal with the assistance of a level, which is positioned to span across both optical assemblies. The beam directions are adjusted so that the light emitted from one optical assembly impinges onto the center of the opposite optical assembly. The above procedures are iteratively applied until both focal points fall on the needle, the heights of both optical assemblies are equal, both optical beams are directed through the center point, and each optical beam impinges on the center of the opposite optical assembly. Once this is achieved, the optics are aligned.

5.2.3 Sample Alignment

Mounting wax was used to attach the sample to the mounting pin and fasten the pin, with the sample, onto the machine. Adjustment of the sample goniometer and rotation of the sample mount was performed until the sample was normal to the incident beam. This can be checked by ensuring that the reflection of the excitation beam from the sample fall on the center of the excitation optical assembly.

5.2.4 Specifying Angles for Data Collection

A sample mounted according to the above procedure can be used as a frame of

reference for specifying excitation and collection angles, both of which are relative to the sample. The y-axis in up in the vertical direction while the z-direction points to the position of the fixed arm. This facilitates the specification of any excitation angle , $\vec{e}$ , or detector angle, $\vec{d}$ , as a unit-vector pointing from the sample. The excitation and detection angles can be considered functions of angles in the spherical coordinate system, here specified by the angles $\alpha, \beta, \gamma, \delta$ . The physical machine angles (Fig. 16) $\theta, \tau, \phi, \chi$ that correspond to $\alpha, \beta, \gamma, \delta$ are found using the relations below, where R is a standard rotation matrix.

$$\vec{e}(\alpha, \beta)=R(\chi)R(\phi)R(\theta)\hat{z}$$

$$\vec{d}(\gamma, \delta)=R(\chi)R(\phi)R(\theta+\tau)\hat{z}$$

$$\cos(\tau)=\vec{e}\cdot\vec{d}$$

$$\vec{p}=\vec{e}\times\vec{d}$$

$$\tan(\phi)=p_z/p_x$$

$$\cos(\chi)=p_y$$

$$\cos(\theta)=e_y/\sin(\chi)$$

Note that multiple solutions exist because more than one set of physical angles correspond to any direction.


5.2.5 Geometrically Blocked Directions and Order of Data Collection

Typical measurements involve probing a large set of directions. An algorithm was devised to take all the desired measurement angles and calculate all possible corresponding machine angles. The order in which the input set is traversed is dependent on which machine angle in closest to the current position. This greedy

48

algorithm was chosen due to its simplicity, its reasonable minimization of the overall collection time, and its graceful handling of the geometrically obstructed machine angles. If the input set was collected in the order the angles were specified then it becomes possible to require excessive machine movements in between subsequent input points when alternative points exist which are closer. This can occur because of the none linear relation between sample angles and machine angles. Furthermore, sometimes one set of machine angles is blocked, either by the Eulerian cradle or the motor that is carried by the cradle. However, often an unblocked alternative set of machine angles is available with which to perform the measurement. Simply specifying that the next set of machine angles is the closest one for which a measurement can be performed avoids some of the possible complexities in creating a program that can neatly handle the mentioned situations.

5.2.6 Lens Selection

There exists a relation between the focal length of a mounted lens, the numerical aperture, the required clear diameter of the lens, and the magnification ratio. These parameters need to be considered as an interrelated group. Figure 17 depicts the relation of these parameters. The magnification ratio sets the spot size on the sample because the lens magnifies and projects the image of the fiber optic cable on to the sample. The focal length needs to be appropriately choses so that the lens can be mounted a minimum of about 300 mm away from the center point to avoid collision with the Eulerian cradle. The required clear diameter of the lens sets a minimum size on the diameter of the lens. Finally, the numerical aperture affects the angular resolution of the

measurement and also controls the amount of light collected. Three achromatic doublet lenses were acquired for the diffractometer: 1) 25 mm diameter with 30 mm focal length; 2) 25 mm diameter with 40 mm focal length; and 3) 50 mm diameter with 75 mm focal length.

### 5.2.7 Recording Data

The data recorded to disk needs to contains all the relevant pieces of information that are associated with each single specified angle that is to be measured. This data includes: time of measurement in seconds, sample angles, machine angles, if the measurement was geometrically blocked, the integration time of the spectrometer, the number of spectra averaged by the spectrometer, and the counts at each pixel of the spectrometer. As each measurement occurs, this data is written to a single line in a human readable text file. Once measurement is complete for the entire set of input points then the entire text file can be processed to extract information.

### 5.2.8 Imaging Data

The diffractometer may acquire thousands of data points that need to be effectively visualized. A generalized program to plot this data was created. However, it is limited to either plotting a set of detection angles for one fixed excitation angle, or vise-versa. A plot can be made for a set of excitation angles where the detector angle is fixed. These sets of data are presented as polar plots, where the center is specified as a specific direction and orientation relative to the sample. For example, we can plot the detector angles, centered about $\vec{d} = (180°, 0°)$ where the distance from the center of

the plot is a measure of the angle from the center vector and the position about the center vector in the plot represents the position of the detector angle about the center vector.

5.3 Results and Discussion

The apparent sphere of confusion for this 4-circle diffractometer is about 1 millimeter with a relatively quick alignment of the optics. If great care is taken in aligning the optics then it may be possible to reduce the sphere of confusion to several hundred microns. These sizes for the sphere of confusion make it possible to perform reliable measurements on small sized samples such as patterns created by interference lithography, where the structures prepared in our lab are only consistent over distances of about 1 or 2 millimeters.

Collection times for large data sets is also reasonable. About 5000 points can be collected in about 6 hours when the integration time is about one second. It is sufficient to use 5000 points to make a relatively detained plot of detector angles, each spaced about 2° apart and covering about 75° from the normal direction.

The ability to collect data in the infrared was confirmed by using a near infrared spectrometer that collects 256 channels for wavelengths between 0.9 and 1.6 microns. The simultaneous collection of data with multiple spectrometers should be possible by using a bifurcated fiber-optic cable to divert the detected light into two spectrometers.

The angle resolved transmission was performed on a photonic crystal inverted in cuprous oxide. The photonic crystal template had three-fold symmetry with a ~900 nm in-plane lattice vector. A six fold pattern of sharp diffraction spots was revealed (Fig. 18).

For this plot, the incident angle was fixed, normal to the substrate and data was collected, at 2° intervals for all detector angles within 75° of the normal direction, opposite the excitation. As the intensity of collected light spans a large dynamic range parts of the plot become saturated while other parts are difficult to visualize due to the low level of signal. Further work is required to facilitate the effective imaging of data sets with large dynamic ranges.

A plot of is presented (Fig. 19) for the diffraction spots formed when the detector angle is fixed in the normal direction and the excitation angle is spanned in 2° increments inside of 75° to the normal direction. The sample was a colloidal crystal with a ~600 nm in-plane lattice vector (the colloidal diameter), inverted in titanium dioxide via atomic layer deposition. It is observed the the diffraction spots are much broader in extent compared with the cuprous oxide photonic crystal, which was prepared using interference lithography. This is likely due to the increased defect density in colloidal crystals, such as the unavoidable drying cracks, which could cause diffuse diffraction spots.

5.4 Conclusions

The 4-circle diffractometer in now a capable tool for performing angle-resolved optical characterization of photonic crystals. The further collection of more extensive data sets may potentially show a relationship between the quality of a photonic crystal structure and the quality of the angle resolved diffraction patterns.

**CHAPTER 6**

**MODELING CONFORMAL DEPOSITION**[c]

6.1 Introduction

Atomic layer deposition (ALD) is a chemical vapor deposition technique that

iterates between two self-limiting reactions to conformally deposit less than a monolayer

of material per cycle. This allows the uniform and conformal infilling of extremely high

aspect ratio structures. While most applications of ALD use substrates that are planar or

have simple cross-sections, the infilling of complex three-dimensional (3D) porous

materials is of interest for electronic and optical applications in which a material's

dielectric properties are fine-tuned [84]. This is especially important for photonic

crystals, which are periodic arrangements of dielectric materials. Profound effects in the

propagation and emission characteristics of electromagnetic radiation can occur when

wavelengths are on the order of the photonic crystal period. Interesting applications for

photonic crystals at wavelengths near the visible spectrum include high-efficiency solid

state lighting [7,85] and ultra-compact waveguides [86,87] for telecommunications.

These applications require the precise sub-micron 3D-patterning of high refractive index

materials, which is difficult to achieve with conventional lithography [65,88]. Some

promising fabrication routes involve creating a 3D template via colloidal self assembly,

direct laser writing, or multi-beam interference lithography. Chemical vapor deposition is

then used to fill the template with high refractive index materials, after which the

---

c   This chapter contains material that was previously published (A. Brzezinski, Y.C. Chen, P. Wiltzius, P.V. Braun, "Complex three-dimensional conformal surfaces formed by atomic layer deposition." Journal of Materials Chemistry, **19**, 9126-9130 (2009) . The copyright owner has provided permission to reprint this material here.

template is removed. With this technique silicon [54,89,90,51], germanium [91,43], and titanium oxide [92,93] photonic crystals have been produced. But, the final structure is generally not the direct inverse of the template because the conformal deposition eventually pinches-off the continuous channels of voids in the template, leaving some void space unfilled. Furthermore, designers are not limited to only infilling photonic crystals completely but may employ partial infilling to achieve optimal structures. However, the difficulty of accounting for conformal deposition (or etching) in porous materials and other complicated 3D structures poses a significant unsolved problem.

The conformal surface problem is a challenge in the high-refractive-index infilling of  photonic crystals because it is necessary to account for both the geometry of the original structure and the subsequent evolution of the conformally deposited material. It is not straightforward to calculate the evolving shape of the surface when conformal deposition occurs in topographically complex 3D templates such as those made using interference lithography. Here we introduce a universal conformal surface calculation method to determine the material distribution. First, the conformal surface problem is discussed and our calculation method is presented. Next, the fabrication and characterization of a conformally infilled photonic crystal template is described. Finally, experimental data are compared with predictions based on the conformal surface calculation.

## 6.2 Existing Techniques

A photonic crystal's optical characteristics are directly dependent upon the material distribution within the structure. Studies of optical features as a function of the

conformal deposition have been undertaken in colloidal crystal templates [94,93] and woodpile templates [51,91]. Such calculations are straightforward for templates described by the union of regular geometric shapes but not for more complex structures. Moon [72] required an elaborate method to study the infilling of templates fabricated by multi-beam interference lithography. The intensity pattern from multiple overlapped coherent laser beams is calculated as the squared sum of the electric field vectors [95].

$$I(\vec{r}) = | \sum_{i \in [beams]} \vec{E}_i(\vec{r})|^2$$

Moon starts with the common practice [56,96,97] of describing the photo-resist template with an iso-intensity surface, assuming regions below some threshold intensity are dissolved away while regions above the threshold remain. A gross approximation of a conformally deposited material distribution is obtained by using two iso-intensity surfaces [97]. This approximation was then significantly improved by adding correcting terms to minimize the thickness variation between the two surfaces [72]. However, the applicability to arbitrary 3D structures is limited by the trial and error method used to find enough appropriate adjustable parameters to achieve an acceptable error tolerance. Applicability is further limited because the initial structure must be adequately described by an iso-surface.

6.3 Conformal Surface Calculation Algorithm

Our conformal surface calculation relies on the discretization of space into a large number of identical parallelepipeds that occupy the sites of a lattice. These volume

elements, or voxels, are initialized to contain either void space or the initial structure material. This permits the method to handle any arbitrarily complex 3D structure with the only limitation being that the error is proportional to the fineness of the discretization. Further discussion of the error is presented below after the description of our algorithm's two major components, determining if a path exists between an interior surface and an external deposition source, and depositing conformal layers of material on the existing surface. Path testing and surface propagation are iteratively applied in a series of finely discretized steps that evolve the surface. First, path testing, then surface propagation, again path testing, and so on. Each iteration is limited to propagating the surface by no more than a third the distance of the voxel diagonal, which is equivalent to the Courant–Friedrichs–Lewy condition [98] that applies to grid-based methods for solving equations.

Testing for a path between the deposition source and a surface is done with a "flood-fill" algorithm which is a common method for finding similarly colored adjacent pixels in a drawing program [99]. This algorithm starts at a voxel and recursively checks its nearest neighbors, and their nearest neighbors, and so on, until it ultimately finds a connected cluster of empty voxels through which deposition gases can flow. Deposition only occurs on surfaces that have a path to the deposition source. "Pinch-off" is said to occur when all paths between an interior surface and the external source have been closed due to conformal deposition. Pinch-off is depicted in Fig. 20(a) where a path existed prior to the deposition of the shaded voxels, which now prevent gas flow into the pinched-off region.

Propagating the surface along the local normal is done in an implicit manner, avoiding the problematic calculation of the surface normal. The shortest distance

between a point (a voxel) and a continuous surface (many voxels that lie on the interface between solid and void) is along a line that is normal to that surface. One may simply calculate the distance between every empty voxel and every surface voxel, depositing material into empty voxels wherever the deposition thickness exceeds the shortest distance to a surface. An algorithmic improvement ($N^4$ versus $N^5$ complexity) is obtained by assuming that the shortest distance to the template surface lies along a connected path of deposited voxels that necessarily originates at one of the voxel's nearest neighbors. These connected paths are dynamically constructed by having every deposited voxel point towards the nearest neighbor through which its shortest path was found (Fig. 20). This algorithmic improvement has a slightly worse error bound for a given grid size because the central assumption is occasionally false. But, the benefit is a drastically reduced computation time. Furthermore, the memory requirement is reduced to only a portion of one byte per voxel, which permits the assignment of voxel attributes, such as several different material types, while only allocating one byte per voxel.

The space discretization sets the magnitude of the error because the calculated position of any surface cannot be resolved to less than the voxel size. The error in surface thickness is multiplied by the surface area of the structure to obtain the volumetric error. This error is typically the most important because the dielectric volume fraction strongly affects the spectral position of photonic features. For the case of a computational cell that has $N^3$ voxels, the surface area and absolute error will be proportional to $N^2$, which gives a relative volumetric error proportional to $N^{-1}$.

Our method was numerically validated using the analytical result of 3.59% total

void fraction remaining upon conformal deposition until pinch-off on an idealized

colloidal crystal. Three mutually touching spheres (Fig. 20c) define the pore that was

closed upon pinch-off. Periodic boundary conditions were applied to the parallelepiped

computation volume, forming a face-centered-cubic primitive unit-cell with angles of 60°,

60°, and 90° between the edges. 1000 different origin positions (small shifts within one

voxel) were employed for each value of N, the number of voxels on an edge. The result

(Fig. 20c) is consistent with the $N^{-1}$ dependence of the volumetric error. A maximum

error of 0.11% is obtained for N = 512, or about 56% of $N^{-1}$, which demonstrates the

accuracy of our method. Using a contemporary personal computer, a single calculation

for N = 512 completes in about two minutes. Thus, it is practical to incorporate our

method when performing design optimization, such as maximizing the photonic band-

gap. Since the error, storage, and run-time are respectively proportional to $N^{-1}$, $N^3$, and

$N^4$, halving the error requires 8 times the storage and 16 times longer to compute.


6.3.1 The Resolution Parameter, Parallelepiped Voxels, and Error Bounds

In order to discuss the scaling and error bounds of the algorithm it is useful to

define N as a measure of the resolution of the computational grid. Also, N is the length,

in voxels, of one side of the computational domain so the discussion below assumes the

domain is N * N * N = $N^3$ voxels in size. The arguments below will also apply to domains

having different numbers of voxels on each side because these lengths can be set

equal to some N scaled by a constant factor that is irrelevant to the asymptotic behavior

of the scaling and error bounds.

The thickness of material deposited in a single iteration is limited by the Courant–

Friedrichs–Lewy condition to less than the distance across a single voxel. This ensures the proper flow of information between voxels during successive growth iterations so that the algorithm correctly identifies the nearest surface to each empty voxel. When the voxel shape is cubic the maximum thickness per iteration is a third the of the voxel diagonal. However, the algorithm is designed to work with voxels having an arbitrary parallelepiped shape as this facilitates the representation of a primitive unit cell of a Bravais lattice. In this case, it is necessary to limit the deposition per iteration to no more than a third of the minimum diagonal distance across the parallelepiped voxel.

Pinch-off may occur anywhere inside the voxel but a voxel's position is represented by its center. Here, the assumption is made that the error is due solely to the difference between the true pinch-off point and the center of the voxel. Thus, the maximum possible error is proportional to the longest diagonal of the voxel. Furthermore, the error bound is made tighter by choosing a voxel shape that minimizes the longest diagonal. Also, when the resolution N is increased, the length of each voxel becomes smaller and the error bound becomes tighter. It is easy to see that the relative error in the deposition thickness at pinch-off scales as $N^{-1}$. The relative volumetric error in the amount of deposited material would be the thickness error times the surface area divided by the volume, respectively $1 * N^2 / N^3 = N^{-1}$.

To estimate the size of the bounds on the volumetric error and compare it to the expected asymptotic behavior, we used the algorithm to calculate the filling fraction of infilled spheres on an fcc lattice. 1000 calculations were performed for each value of N, where N is either 64, 128, 256, or 512. The voxel at the origin of the sphere in the privative fcc unit cell was uniformly spanned with 1000 points (a uniform grid, 10 points

in each direction) which served as the exact position of the sphere center in each respective run of the algorithm. This has the effect of shifting the exact position of the true pinch-off point. Furthermore, the voxels that are initially set solid and empty (respectively inside or outside the sphere radius) may differ for each run. The filling fraction at pinch-off was calculated for each run of the algorithm and the maximum and the minimum results were plotted (Fig. 20). This forms an empirical estimate of the error bounds and also demonstrating the apparent $N^{-1}$ convergence to the value 0.9641, the analytical result for fcc spheres. Although larger deviations might be found at points in between the 1000 sampled origin-points, it is likely that the sampling is sufficiently dense to capture the majority of the error and its behavior.

6.3.2 Calculating the Distance to a Surface

To calculate the distance from an empty voxel to a surface, the path is followed from the voxel, through the previously deposited voxels, to termination on an original surface voxel. This distance can be represented by an integer number of steps in the respective directions of the vectors which describe the parallelepiped voxel:

$$d = \left( \vec{d} \right) = \left( n_a \vec{a} + n_b \vec{b} + n_c \vec{c} \right)$$

As each of the six possible paths leading from an empty voxel are compared to find the shortest distance to a surface, it is possible that two different surface voxels are equidistant from the empty voxel. But the algorithm must choose one of these equidistant surfaces as being the nearest surface. In our implementation, the shortest equidistant path is that path that was probed first, while the order of probing (-a direction, +a, -b, +b, -c, and finally +c) remains constant. This can potentially lead to a

60

slight anisotropy in the different directions of our computational domain. Furthermore, our implementation conveniently accumulates the distance vector, d, at each voxel of the traced out path to the surface. This can cause seemingly equidistant paths being unequal due to round off as the d-vector is accumulated. Thus, in the above sampling of the 1000 origin-points to estimate the error bounds, points that may have appeared degenerate due to the fcc symmetry are in fact distinct.

The origin of the larger error bounds for our improved $N^4$ algorithm vs the straightforward $N^5$ algorithm lies in the necessary choice between two ideally equidistant surfaces. Examples can be contrived where a certain choice prevents subsequently deposited voxels from finding the true nearest surface. However, the error cause by this occurrence is a fraction of a voxel length. Furthermore, as the deposition proceeds these errors tend to be reduced and even eliminated because the distance from these other empty voxels to alternate candidates for a nearest surface either become closer to the true nearest distance or they become the true nearest distance. The above empirical estimation of the error bounds suggests that the effect due to incorrectly identifying the true nearest surface is not significant.

6.3.3 Scaling of the Computation Time

The straightforward brute-force approach to calculate each voxel's nearest surface requires calculating the euclidean distance between each empty voxel and each surface site. In a three-dimensional computational volume with N voxels per side, $N^3$ voxels in total, the number of empty voxels is proportional to the total number of voxels, $N^3$, and the total number of surface voxels will be proportional to $N^2$. The complexity for

testing $N^3$ empty voxels against $N^2$ surface voxels is $N^3 * N^2 = N^5$, which is the dominant contribution to the computation time.

In the presented algorithm the complexity is reduced to $N^4$. Each of the $N^3$ empty voxels are tested against a constant number or paths to a potential nearest surface. These tests are only performed when the empty voxel in question is adjacent to the surface, which is only for a constant number of growth iterations. However, the path length will be proportional to N, giving $N * N^3 = N^4$ computational cost. An alternate way to derive this result is that there are $N^2$ empty voxels adjacent to the surface which must be tested at each growth iteration. The total number of growth iterations, like the path length, is proportional to the linear distance across the computational domain which is proportional to N, giving $N^2 * N * N = N^4$ complexity.

The above analysis only accounted for the cost of finding the nearest surfaces. An additional cost is incurred by checking for a continuous path of empty voxels between the deposition source and the growth surface. The "flood-fill" type algorithm will visit each of the $N^3$ empty voxels in every growth iteration and the total number of iterations is proportional to N, giving $N^3 * N = N^4$ complexity. To further improve the computational cost would require improvements to both the nearest surface algorithm and continuous path algorithm which form the complete algorithm for tracking the evolving surfaces during conformal deposition.

The $N^4$ scaling of the improved algorithm is demonstrated in Fig. 21 where a primitive unit cell with the specified number of voxels per axis is used for the computation. At the last data point, with 1024 voxels per axis, the slope of computation time on the log-log plot is nearly 4, the expected asymptotic value. In comparison, the

straightforward $N^5$ algorithm that we implemented required about 10 minutes at 128

voxels per axis and about 5 hours at 256 voxels per axis. This is consistent with $N^5$

scaling and also requiring significantly more time compared to the few seconds used by

the improved algorithm.


### 6.3.4 Touching Spheres on an FCC Lattice

To find the the analytical result for the filling fraction of conformal deposition, until

pinch-off, on touching spheres arranged to form a fcc lattice, we divide the sum of the

initial and grown material volume in one primitive unit cell by the total volume of that unit

cell. Let $R_1$ be the radius of the initial spheres, then it is trivial to derive the unit cell

volume, $V_{cell}$, and the distance, $R_2$, from the sphere's center to the pinch-off point at the

centroid of three mutually touching spheres (Fig. 1):

$$V_{cell} = 8R_1^3 / \sqrt{2}$$

$$R_2 = 2R_1 / \sqrt{3}$$

The interior of the fcc lattice of spheres becomes pinched-off after a total thickness of

$R_2$-$R_1$ of material is deposited, as all path to the surface become closed. The final

volume of the initial and deposited material will be the volume of a sphere with radius $R_2$

minus the overlapping volume of the neighboring spheres. It is straightforward to derive

the volume of a spherical cap, the region bounded between a sphere of radius r and an

intersecting plane, distance p from the sphere center.

$$V_{cap} = (\pi/3)(2r^3 - 3r^2 p + p^3)$$


As there are 12 nearest neighbors, 12 cap volumes must be subtracted, with r = $R_2$ and

63

$p = R_1$. The total filling fraction at pinch-off is

$$f_{pinch} = \frac{V_{sphere}(R_2) - 12\,V_{cap}}{V_{cell}}$$

$$f_{pinch} = (\pi\sqrt{2}/6)\left(9 - 5(2/\sqrt{3})^3\right) \approx 0.964102939$$

6.4 Experimental Procedures

Comparison of the conformal surface calculation with experiment started with the use of multi-beam interference lithography to make five SU-8 photo polymer templates with differing parameters. We followed our published procedure, but using cyclopentadienyl(fluorene)iron(II) hexafluorophosphate as the photo-acid generator and using a 25° central angle (inside the photo-resist) for the four-beam umbrella configuration. The templates (Fig. 22) were conformally infilled by atomic layer deposition (ALD) of alumina. Prior to deposition, the templates were allowed to relax for 6 hours at the 85 °C deposition temperature. One ALD cycle consists of 0.03 s pulse of water vapor with 2 s hold, 65 s nitrogen at 20 sccm nitrogen flow, then trimethylaluminum was released and purged using the same parameters.

The SU-8 withstands the 85 °C ALD temperature and permits the use of an exposure intensity iso-surface to analytically describe the template surface. As alumina is deposited, the average refractive index of the structure increases, and thus the reflectance peak red shifts. The modest refractive index of 1.6 for alumina, however, avoids overlapping the reflectance peak with the SU-8 absorption at wavelengths longer than 2.4 µm, enabling accurate comparison of theory and experiment.

The reflectance spectrum was measured starting with the SU-8 polymer

template, and then after every 100 cycles (150 cycles for the first iteration) or 12.7 nm of alumina ALD, ultimately ending after 1850 cycles (Fig. 22c). A reflective silicon wafer was also present in the ALD chamber in order to measure the thickness of deposited alumina via ellipsometry. Ellipsometry also determined the SU-8 and alumina refractive indices as 1.57 and 1.60, respectively. Reflectance spectra were carefully measured from several specific locations on each template, as different regions of the sample display slight differences due to inhomogeneities in the fabrication process. These spectra are taken from a 150 μm spot with a 0.1 numerical aperture 4x lens using a Fourier transform infrared spectrometer. The discussion that follows focuses on the data from one specific location on one template because this is representative of the trends observed at all measurement spots on all five templates.

The structure of the initial SU-8 template was determined by fracturing the starting sample into two pieces, one of which was examined by focused-ion-beam milling and scanning electron microscopy (Fig. 22), the other of which was infilled with alumina. The spacing between the (111)-layers parallel to the substrate in the fcc-like structure was measured as 520 nm. The shrinkage to 44% of the original 1178 nm (111)-spacing in the interference lithography setup is typical for 3D SU-8 structures. The in-plane shrinkage is suppressed because the template adheres to the substrate. As a first-order approximation, the shrinkage is modeled as an affine scaling in the normal direction. The total thickness of the template is 10.5 (111)-layers and it sits on a substrate consisting of an adhesion promoting 700 nm SU8 layer on top of a microscope cover glass slide. The material distribution was obtained by the conformal surface calculation method, using 625 voxels per micrometer, and subsequently used

as input for a finite difference time domain calculation [69] (FDTD) using 28 voxels per micrometer. The starting point for the calculations is the iso-intensity surface that corresponds with a 43% polymer filling fraction, consistent with the Bragg approximation of the reflectance peak,

$$\lambda_{Bragg} = 2 d_{111} \sqrt{(1 - f_{SU-8}) n_{air}^2 + f_{SU-8} n_{SU-8}^2}$$

where $d_{111}$ is the (111)-layer spacing, f is the filling fraction, and n is the refractive index. This structure is then shrunk in the vertical direction to 44% of its original size. This provides an initial model of the template which is largely determined by independently measured parameters. A ~0.7° mis-orientation of the experimental (111)-surface was taken into account by averaging eight FDTD spectra with differing (111)-surface terminations to produce each presented spectra. Also, the procedure was repeated to obtain FDTD spectra for $d_{111}$ spacings of both 500 nm and 540 nm.

6.5 Discussion of Experimental Verification

The position and magnitude of experimental spectral features in Fig. 23 are well matched by the FDTD calculation. As the alumina content increases, the positions and magnitudes of the reflectance peaks and Fabry-Perot fringes evolve in unison. The slightly lower measured versus calculated reflectance is expected because of the small imperfections due to surface micro-roughness, residual stress, resist resolution limits, and imperfect laser beam profiles. At 129 nm deposited alumina, the FDTD and experimental reflectance simultaneously vanish due to the negligible variation in the average refractive index in the normal direction. At 177 nm of alumina the calculated

structure becomes pinched off with the void space occupying 5.9% of the total volume, or 10.3% of the original void space. Subsequent deposition only occurs on the topmost surface and this explains the lack of evolution for the spectra between 166 nm and 203 nm of alumina. All this indicates that the calculated structure is an accurate description of the experimental structure.

Additional verification of the conformal surface calculation is obtained by showing that a small perturbation in the input (111)-spacing yields measurable differences in the FDTD spectra. The calculation was repeated with 500 nm and 540 nm (111)-spacing. Fig. 24 compares the reflectance peak position and magnitude for all 3 calculated spacings and the experimental structure. The 520 nm spacing curve follows the experimental curve closely. On the other hand, both the 500 nm and 540 nm spacing peak-positions diverge from the experiment and they show different plateaus due to pinch-off at 151 nm and 198 nm of alumina, respectively. This demonstrates that a small ± 4% change to the (111)-spacing input into the calculation leads to significantly different distributions of conformally deposited material. After 228 nm of alumina deposition, the structure was milled by a focused ion beam to reveal an excellent match (Fig. 22c) with the calculated structure. Both the calculated and experimental structures have similar polymer cross-sections, similar thicknesses of deposited alumina, and similarly sized pinched-off voids. Based on Fig. 22c and considering the demonstrated correspondence between our calculated and observed spectra, it appears that conformal deposition techniques can achieve close to the theoretical maximum thickness before pinch-off in complicated 3D structures. Furthermore, the resulting deposition appears to have a uniform thickness throughout the depth of the structure.

6.6 Conclusions

An accurate and universal method to calculate the material distribution by conformal deposition processes within arbitrary 3D structures was developed. The algorithm correctly calculates the theoretical pinch-off for deposition on an ideal closed packed lattice of spheres and exhibits the correct scaling of the error, inversely proportional to the voxel length. The ALD performed on the complex polymer templates appears to have good uniformity of deposition throughout the structure and closely matches the final structure predicted by the algorithm. The FDTD spectra predicted by the algorithm is well matched by the experimentally obtained spectra. Our conformal surface calculation method has been established as being a useful tool for the design and analysis of photonic crystals and can easily be applied to other complex 3D structures in which conformal deposition or etching occurs.

# CHAPTER 7

# NEODYMIUM EMITTERS EMBEDDED IN PHOTONIC CRYSTALS

## 7.1 Introduction

Neodymium is a rare earth element with relatively sharp emission peaks and a lengthy fluorescence lifetime in the range of hundreds of micro-seconds [100]. These properties make it suitable for use as the gain media in lasers. When excited at the 790 nm the main emission peaks occur at about 880 nm, 1060 nm, and 1330 nm which corresponds with the transitions from the $^4F_{3/2}$ state to $^4I_{9/2}$, $^4I_{11/2}$, and $^4I_{13/2}$ respectively. The branching ratio, which describes proportion of each transition is about 25%, 60%, and 15% respectively for the $^4I_{9/2}$, $^4I_{11/2}$, and $^4I_{13/2}$ transitions [101].

## 7.1.1 Altering Neodymium Emission

Embedding neodymium atoms within a photonic crystal makes it is possible to drastically alter the above branching ratios. If a photonic crystal had a complete band-gap that overlapped with the $^4I_{11/2}$ transition, then we would expect all the emission to be redistributed to the other available relaxation pathways. Assuming a 100% quantum efficiency, which means zero non-radiative loss, the $^4I_{9/2}$ and $^4I_{13/2}$ emission would increase by 250%. However, it is difficult to reduce non-radiative losses [102] to negligible levels and it is also difficult to achieve a complete band-gap. But, significant alterations in the emission are possible as long as the quantum efficiency is sufficiently high and a significant reduction in the density of states occurs at the transition energy that we with to block. This is the ultimate goal of this experiment. There is significant

69

scientific interest in demonstrating a profound alteration of the neodymium emission.

Also, this work can potentially be applied to changing the gain wavelengths in rare-earth

based lasers and towards fabricating particles for biological imaging, as 1330 nm

photons can penetrate several centimeters of tissue.

7.1.2 Fabrication of Neodymium Doped Nano-Particles

As neodymium is subject to concentration quenching, it needs to be present in

relatively low concentrations as a dopant in a host lattice. The synthesis lanthanide

trifluoride nano-particles, doped with neodymium, as reported by Stouwdam and Veggel

[103], represents a straightforward route to making particles with various concentrations

of neodymium.

7.2 Methods and Materials

7.2.1 Calculating Optimal Photonic Crystal Structures

Using the parameters for the preexisting configuration of the multi-beam

interference lithography apparatus in our lab, calculations were performed to determine

the density electromagnetic modes. As the processing parameters lead to a range of

material filling fractions and different amounts of photo-resist shrinkage upon

processing, a range of these values were used for multiple calculations.

7.2.2 Fabricating Samples for Measurement

Three batches of neodymium-doped nano-particles were created and deposited

onto glass cover-slips so they may have their lifetimes measured. These batches have neodymium concentrations (the percent substitution in lanthanum sites) of 100%,10%, 5%, and 1%. Also, a photonic crystal sandwich structure was created where two layers of cuprous oxide photonic crystal encompassed a 200 nm thick layer of neodymium-doped (at 100%) nano-particles. The nano-particle layer was spin coated on to a flat polydimethylsiloxane stamp and transfered on to a layer of SU-8 photo-resist. A second layer of SU8 photo-resist was spin coated onto another polydimethylsiloxane stamp and transfered onto the nano-particle layer. The sandwich structure was then patterned by multi-beam interference lithography and subsequently replicated in cuprous oxide.

7.2.3 Fluorescent Lifetime and Emission Spectrum Measurements

Measurements of the lifetime and the emission spectra were achieved with similar setups (Fig. 25). A continuous wave titanium-sapphire laser is tuned to 790 nm where it produces approximately 100 mW of light. The beam is directed through lens and into a chopper wheel, positioned at the focal point so that the beam is completely chopped in the minimum amount of time. The chopper is run at its maximum frequency of 200 Hz. A second lens focuses the beam onto the sample slide at an indecent angle of about 45° and a spot diameter of about 100 microns. A pair of lenses focus the emission energy onto the slit of a monochromator. At the monochromator output, either a liquid nitrogen cooled germanium detector, for collecting the emission spectrum, or a thermal-electrically cooled indium-gallium-arsenide photo-diode, for measuring the lifetime, can be positioned. Emission spectra measurements are collected with a lock-in amplifier. Lifetime measurements use a pre-amplifier to boost the signal before it is

passed into a digital oscilloscope. The response of the system, comprised of the photo-diode, the amplifier, and the oscilloscope, is slow enough that it must be deconvolved from the recorded signal. To record the system response, the monochromator is tuned to 790 nm and the beam path into the monochromator is partially blocked so that the signal from the system is about the same magnitude as the previously measured fluorescence signal, with all gain and oscilloscope settings identical.

7.3 Results and Discussion

The best calculated candidate structure (Figs. 26, 27, and 28) had about a 40% reduction in the density of states, if replicated in cuprous oxide via electro-deposition. These parameters can likely be realized in fabricating a photonic crystal, but it is difficult to simultaneously target multiple parameters without potentially repeating the fabrication process many times. An alternate approach is to use a photonic crystal that is somewhat close to the desired parameters and fine tune the energy at with the depression in the density of states occurs by infilling the structure using atomic layer deposition. Also, other potential candidate structures include those fabricated by interference lithography with a 355 nm laser [54], and a structure created using proximity field nano-patterning [37].

Published values for lifetimes for neodymium in these nano-particles report a bi-exponential fit to 23% with a 40 micro-second lifetime and 77% with a 220 micro-second lifetime [103]. The bi-exponential decay is attributed to OH-quenching on the surface of the nano-particle, which causes a fast decay rate, and a bulk-like decay from emitters inside the nano-particle [102]. The lifetime of emitters inside the photonic crystal

72

sandwich structure was measured to be less than 25 micro-second. This very short lifetime is due to the significant concentration quenching that results in a quantum efficiency of less than 10%, which is too low to be of practical use in this experiment.

From the experiments with the 10%, 5%, and 1% doped nano-particles it is observed (Fig. 29) that the lifetime of the neodymium emitters is significantly increased at lower doping concentrations. To recover the fluorescence signal from its convolution with the response of the system it was necessary to perform reconvolution. This is necessary because Fourier transform of the signal by the transform of the system response produces significant noise in the recovered fluorescence signal. Reconvolution takes the measured system response and convolves it with with the bi-exponential model that we with to fit to. The result can then be compared for fit with the convolved signal obtained in the measurement. Using the published values of the neodymium lifetimes, 40 and 220 micro-seconds, the reconvolution procedure shows a good fit to the 1% doping data when 70% have a 40 micro-second lifetime and 30% have a 220 micro-second lifetime. Higher doping concentrations have significantly shorter lifetimes, making them not useful for this experiment.

The increased lifetime at lower concentrations fits with a report that also shows that the product of the concentration and the quantum efficiency is near constant at low doping concentrations of several percent or less [102]. By reducing the doping to only 0.25%, it is expected that a complete photonic band-gap that blocks the $^4I_{11/2}$ transition would result in an increase of 80% in the $^4I_{13/2}$ transition. Such an increase in emission should be readily detectable. Also, a partial band-gap photonic crystals should also exhibit measurable increases in the $^4I_{13/2}$ emission, as long as the quantum efficiency

was sufficiently high so that non-radiative transitions are minimized.

To further reduce quenching from OH groups on the surface it may be possible to grow a thin undoped layer around the doped nano-particles. Also, simply making the nano-particles larger may also result in a significant reduction in quenching at the surface. Alternately, another method [102] of synthesizing the nano-particles may be effective in reducing OH quenching.

Emission from the photonic crystal sandwich structure was observed to be a few times lower in magnitude compared with similarly doped particles bare nano-particles on a glass slide. It is a concern that sufficient signal be produced from these structures because the lifetime measurement system is is currently collecting data from 1% doped particles that is only about an 1.5 orders of magnitude above the noise floor at a gain setting of $10^7$. But, near identical lifetime results are obtained at the maximum gain setting of $10^8$, where the system response is noticeable slow. Thus, the current lifetime measurement setup should suffice to measure the changes in lifetime that are expected when the emission of neodymium is overlapped with photonic band-gaps.

7.4 Conclusions

The 1% neodymium doped nano-particles has thus far produced the longest lifetimes, compared to doping at higher concentrations. These lifetimes are somewhat below values reported in the literature , which is likely due to quenching at the particle surface by OH groups. Growing larger particles, either with the addition of doped or intrinsic material may reduce the OH quenching and increase the quantum efficiency. Also, it is recommended to reduce the doping concentration to about 0.25% so that

quantum efficiency is further increased. A better candidate photonic crystal structure may best be found by using atomic layer deposition to fine tune the geometry of a photonic crystals that can readily be fabricated with the existing techniques available to the research group. The lifetime characterization system appears to be capable of detecting the faint emission from a thin layer of nano-particles embedded in a photonic crystal sandwich structure. Furthermore, the system should be capable of resolving the resulting changes lifetime due to the photonic band-gap.

# CHAPTER 8

## CONCLUSIONS


Direct laser writing has been shown to be a potentially useful method of making periodic photonic crystals. Furthermore, the ability to easily add non-period features to photonic crystals make direct laser writing a powerful method for fabricating functional photonic crystals.

Angle-resolved spectroscopy is a powerful method capable of characterizing the photonic crystals and capturing effects, such as enhanced emission, that is attributed to the electromagnetic mode distribution inside the photonic crystal.

A colloidal crystal having a relatively low refractive index can exhibit alterations in the electromagnetic density of states that result in increased emission in specific directions. It is possible to exploit the physics of this process to increase the efficiency of solid state lighting. A simple model of the electromagnetic wave-function described the emissive enhancements observed in the inverted colloidal crystal. Furthermore, another model was effective at describing the emission patterns of less than perfect fluorescent photonic crystals.

Calculations of the electromagnetic properties are very useful in the design and characterization of photonic crystal devices. This enables one to target the fabrication process to make photonic crystals with band-gaps at a desired energy range. Versatile methods for replicating photonic crystal templates in to high refractive index materials is somewhat reliant on the conformal deposition calculation algorithm which was developed. This algorithm invites experimentalists to perform a series of conformal

deposition and etching steps by allowing them to predict the the final resulting structure.

The results of this research has generally been promising, in that incremental improvements are being made. The fabrication methods are being expanded and improved, the optical characterization techniques are being becoming more powerful, and the calculations used for design are becoming more reliable. So long as steady progress is being made, it will only be a matter of time before photonic crystals are adapted to a wide variety of applications.
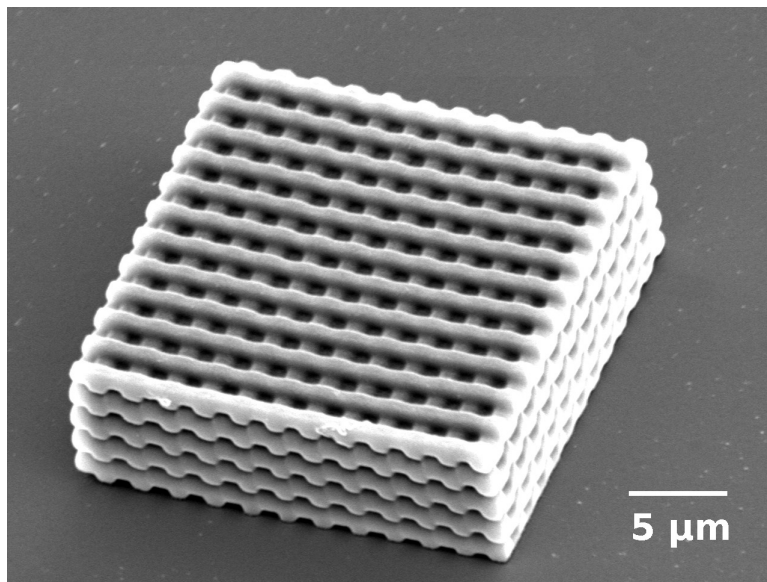
**FIGURES**



Figure 1. Scanning electron micrograph of the highest quality woodpile structure fabricated in SU8 photo-resist using direct laser writing.
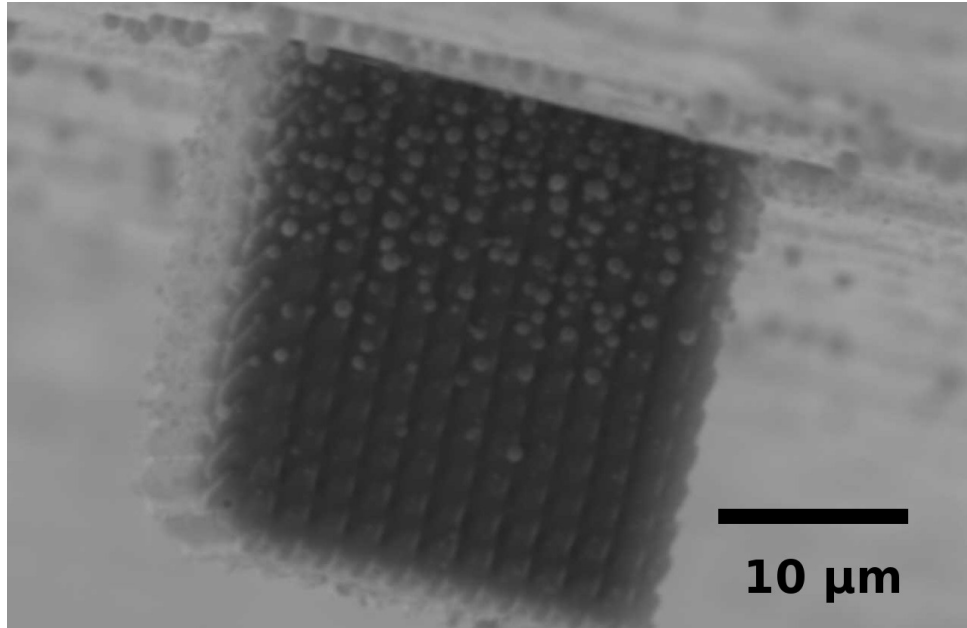
Figure 2. Scanning electron micrograph of an over-polymerized woodpile structure fabricated in SU8 photo-resist using direct laser writing. Note that the pores are closed, when compared with Fig. 1.
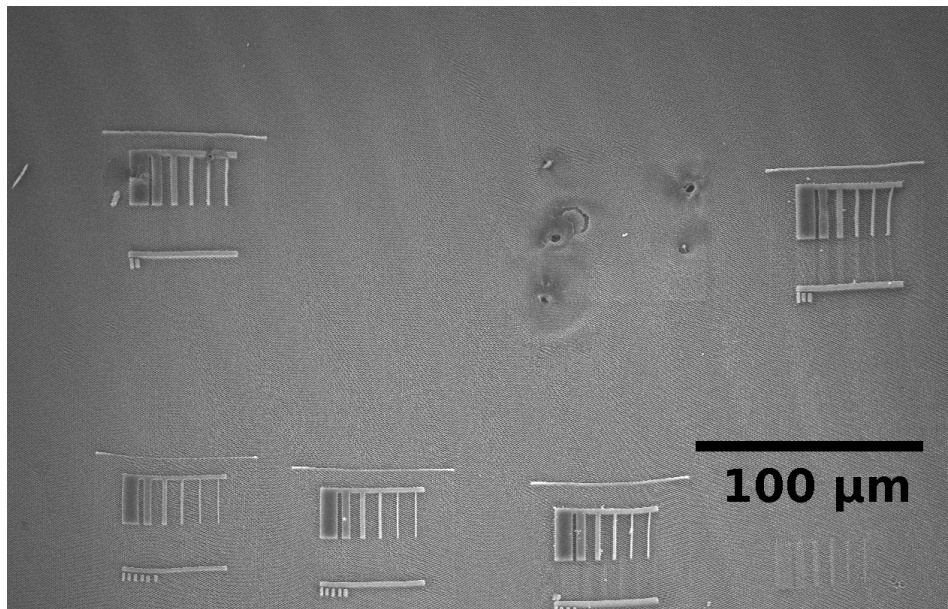


Figure 3. Scanning electron micrograph of a host polymer photonic crystal, fabricated using interference lithography. Direct laser writing was used to add non-periodic defects to the host crystal. The defect areas tend to be highly polymerized and stiff while the host crystal shows significant distortion.
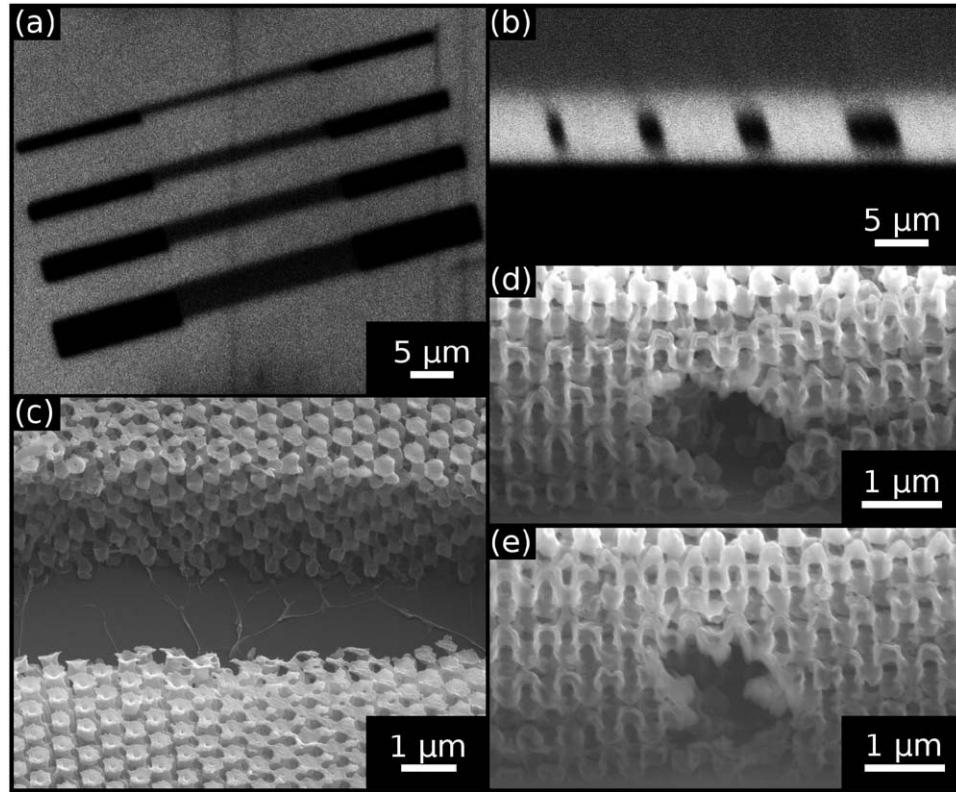
Figure 4. Confocal micrographs of the (a) top-view and the (b) cross-section of regions polymerized (dark) by direct laser writing. Scanning electron micrographs of photonic crystals inverted in silicon showing (c) the 4 µm channel and the focused ion beam milled cross-sections of the (d) 1 µm channel and (e) the 0.5 µm channel. [V. Ramanan, E. Nelson, A. Brzezinski, P.V. Braun, and P. Wiltzius, Applied Physics Letters, vol. 92, 2008, p. 173304.]

Figure 5. SEM micrographs of (a) polystyrene colloidal template and (b) FPC cross-section. (c) Normalized emission spectra, integrated over 76% of 2π sr, from FPC, RuBpy film, and their ratio. Also in (c), normal-incidence reflectance from FPC and template.

FIG. 6. Parts (a)-(e) each have subparts (i), (ii), (iii). FPC emission at (a) 712 (b) 690 (c) 650 (d) 617 and (e) 560 nm. (a)(i)-(e)(i) Normalized intensity vs. θ and φ. (a)(ii) Comparison with model 16. (b)(ii)-(e)(ii) Satisfaction of Bragg condition (white) comparable to (b)(i)-(e)(i) but plotted at half-scale; Bragg planes labeled with Miller index; high symmetry points U, K, and W identified. (a)(iii)-(e)(iii) φ-averaged intensity vs. θ (black, with vertical bars depicting min. and max.), normalized to theoretical BLB (grey); over-bars depict theoretical width of TE (upper bar) and TM (lower bar) stopgaps. Tables point to the stopgap, mode enhancements (ME), and mode density enhancements (DE) where obscured features were extrapolated and reported in parentheses. ME111 points to vertices of bright arcs nominally at φ = 90, 210, and 330º; ME200 vertices at φ = 30, 150, and 270º.
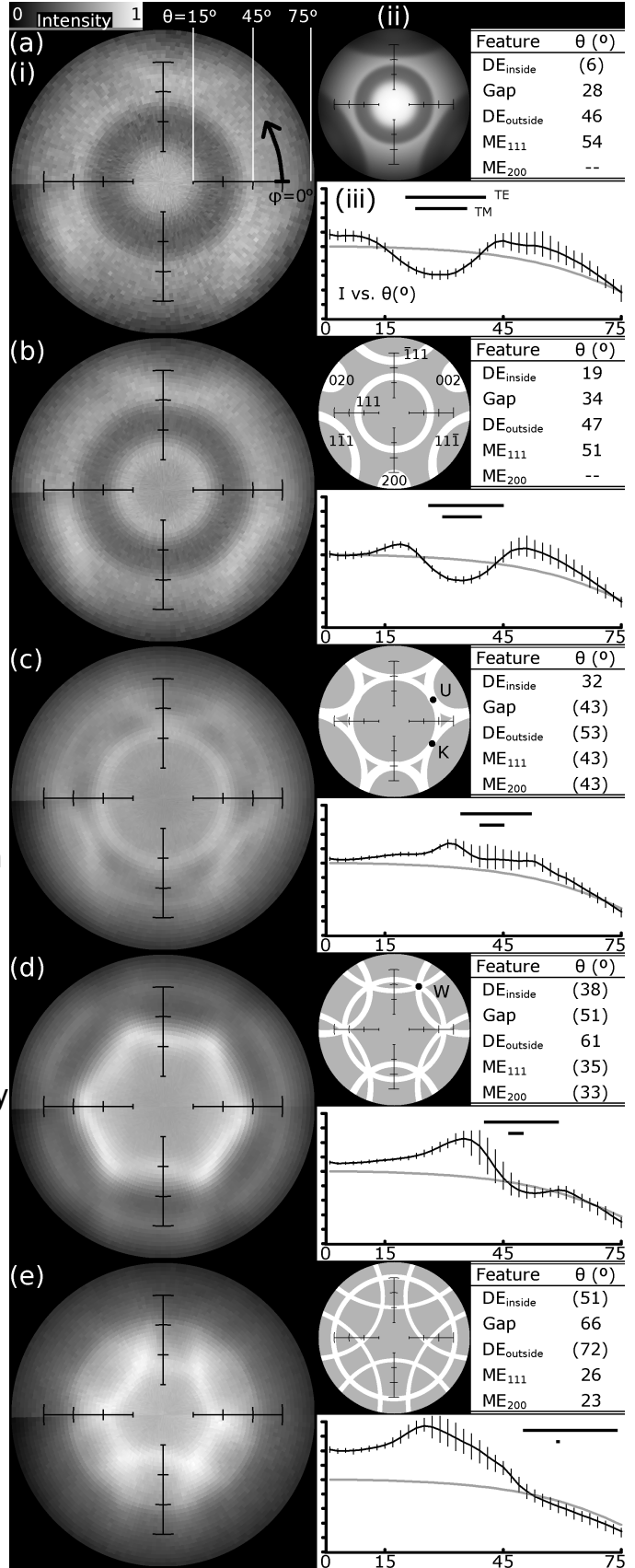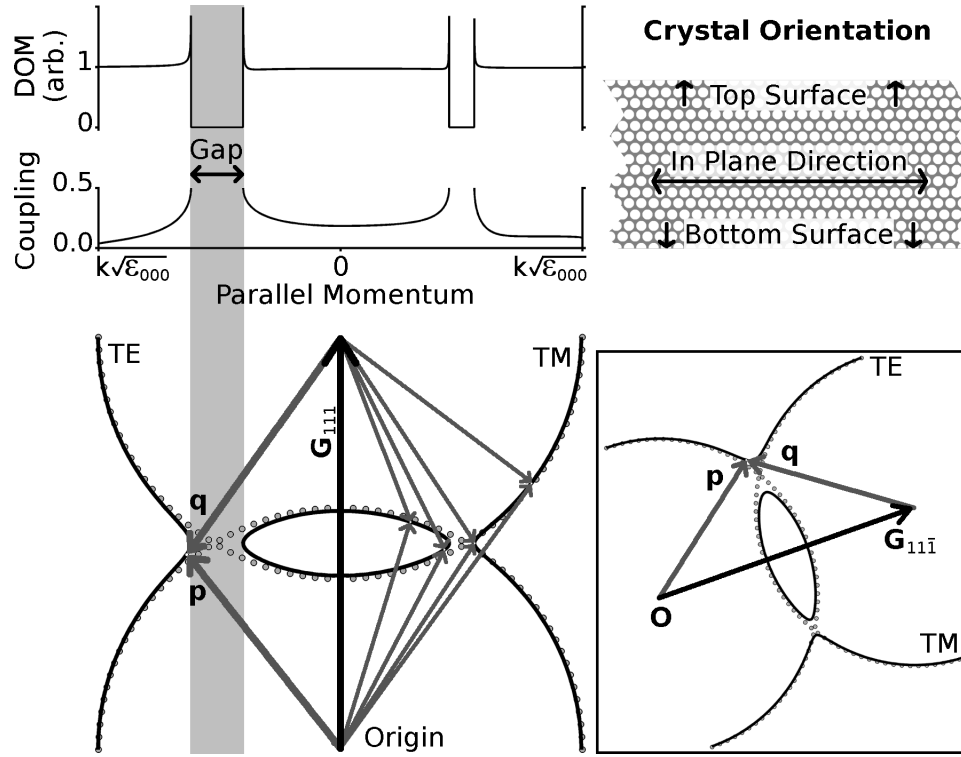
FIG. 7. Momentum space dispersion surface for TE (left of $\mathbf{G}_{111}$ ) and TM (right) for energy $\lambda = 690$ nm and diffraction in $(111)$ , shown relative to $k\varepsilon_{000}^{1/2}$ plane-wave dispersion (dots). A mode point on the dispersion surface is identified with the coupling and DOM by drawing a vertical line. Inset: dispersion for $(11\bar{1})$ Bragg plane at 70.5° to FPC surface.
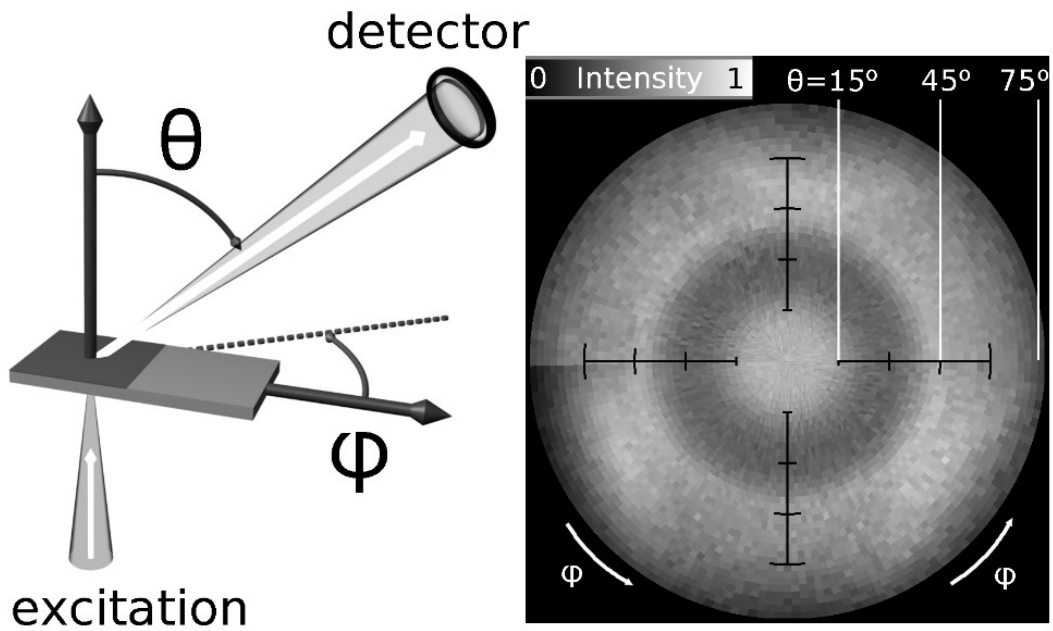
Figure 8. (left) the excitation beam enters the photonic crystal perpendicular to the substrate. Emission data is collected at 2° intervals relative to the normal (θ-direction)and also about the normal (Φ-direction). (right) The collected data, for a single wavelength, is plotted as a function of the exit angle. The high intensity values are light and low intensity values are dark.
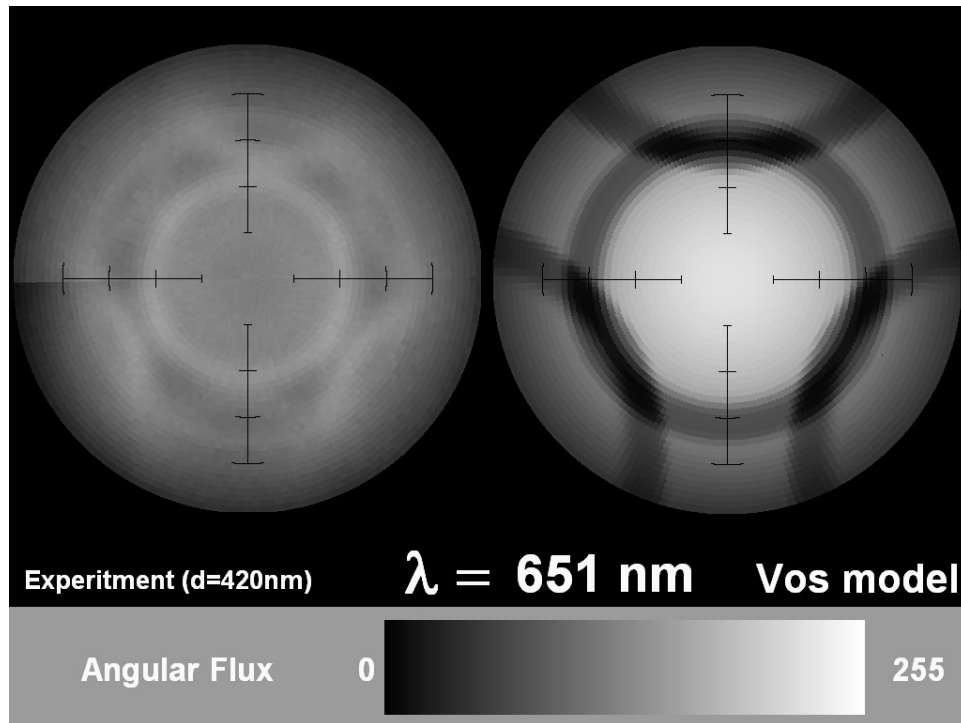
Figure 9. Comparison of the emission from a high quality photonic crystal (left) with the emission calculated using the Vos model (right).
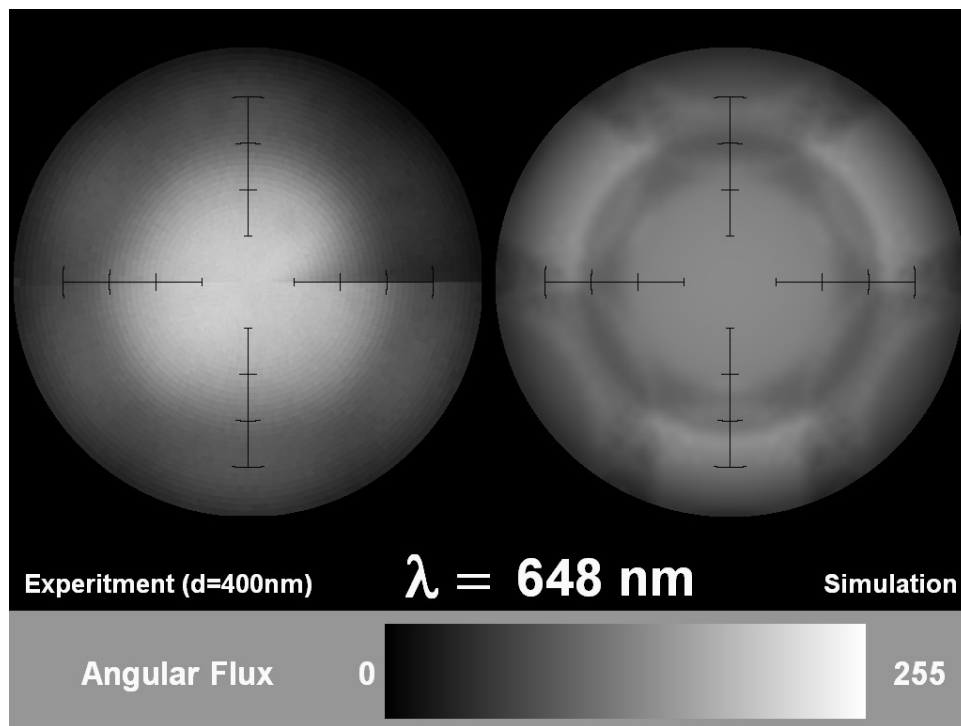


Figure 10. Comparison of the emission from a moderate quality photonic crystal (left) with the emission calculated via a simulation based on a new model (right).
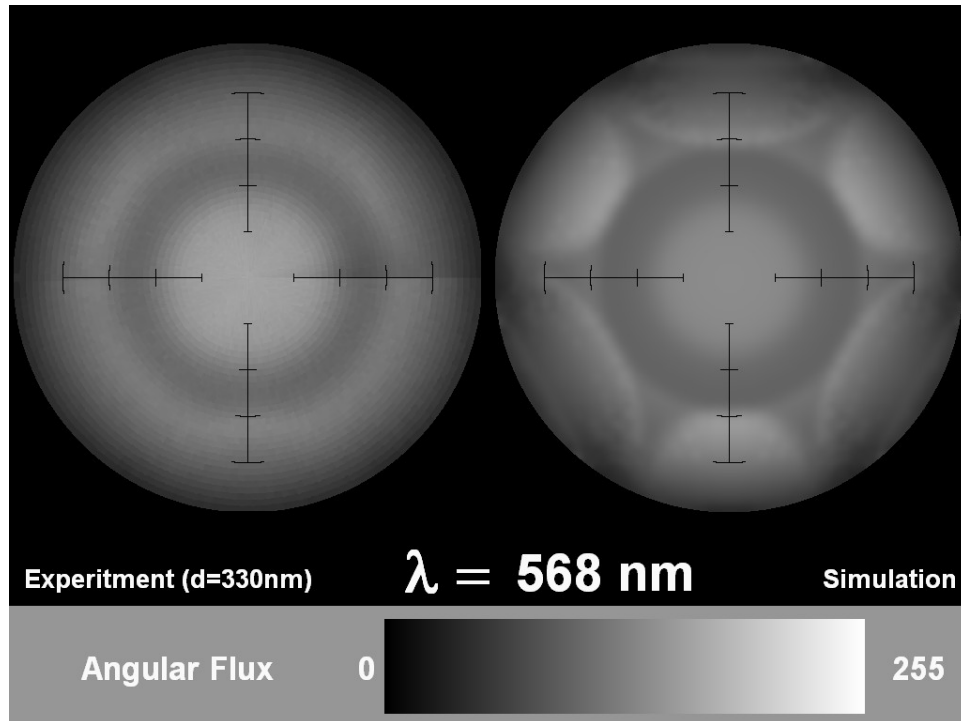
Figure 11. Comparison of the emission from a moderate quality photonic crystal (left) with the emission calculated via a simulation based on a new model (right).
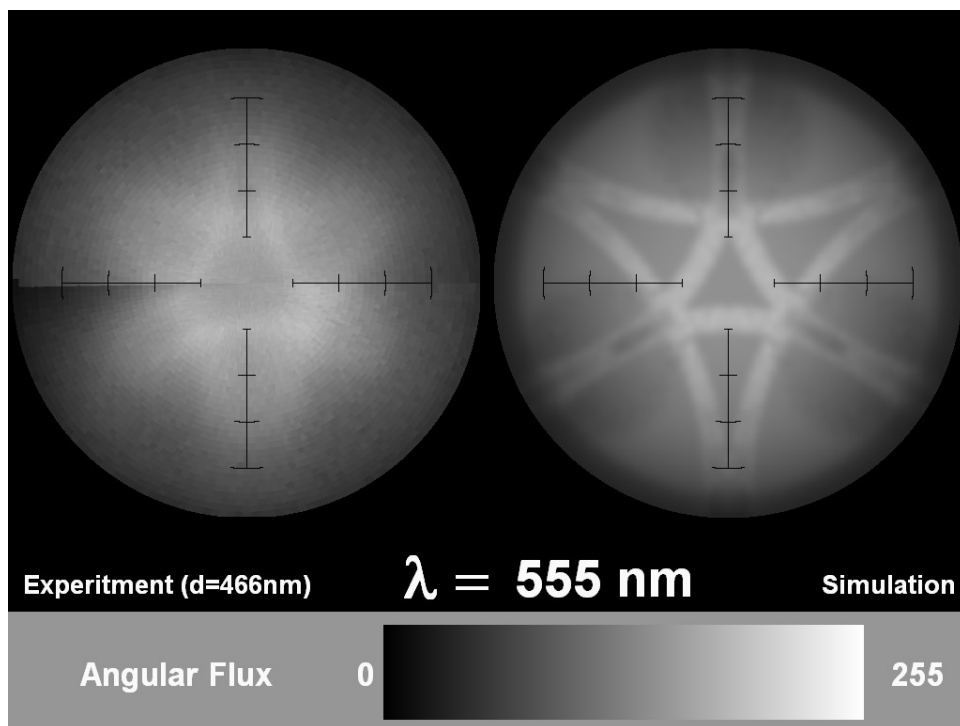


Figure 12. Comparison of the emission from a moderate quality photonic crystal (left) with the emission calculated via a simulation based on a new model (right).
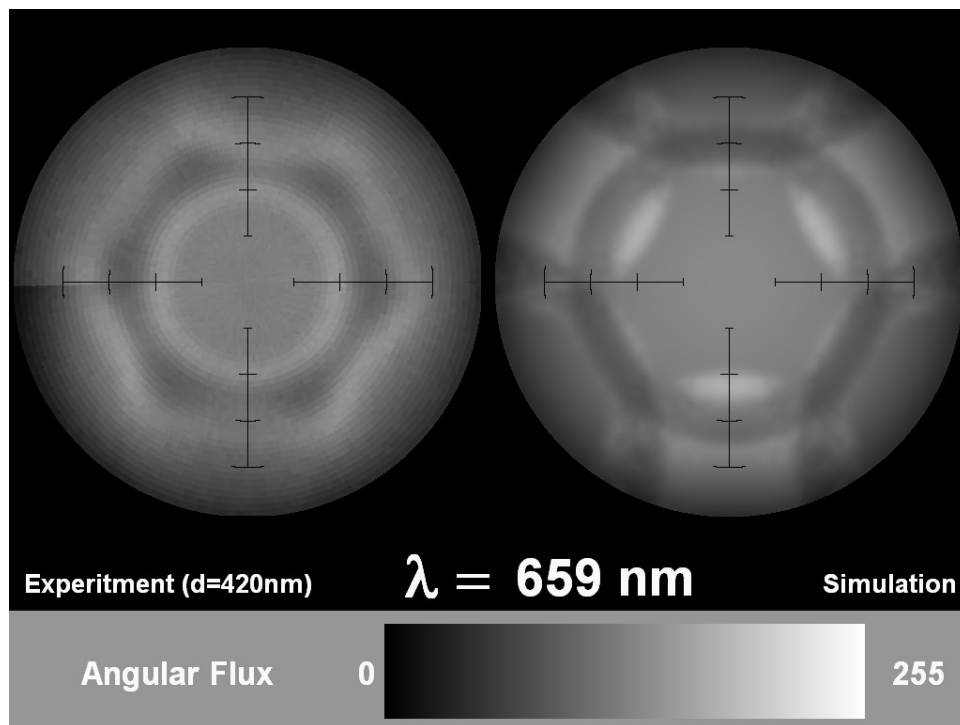
Figure 13. Comparison of the emission from a high quality photonic crystal (left) with the emission calculated via a simulation based on a new model (right).
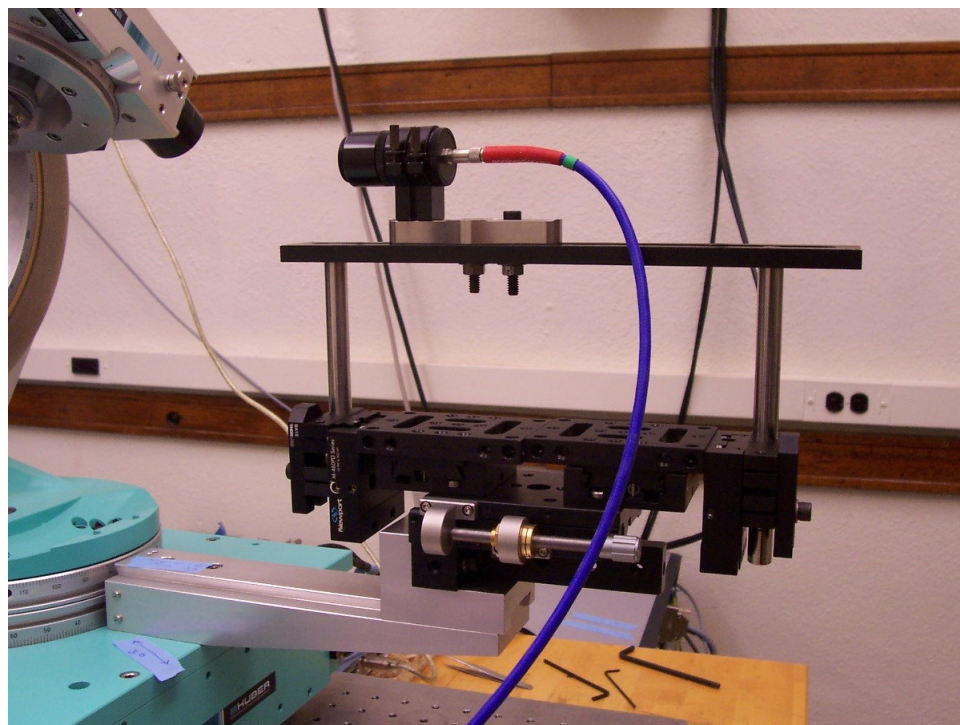


Figure 14. The 5 translation stages that provide all the needed motions for aligning the optical assembly on the fixed arm of the 4-circle diffractometer.
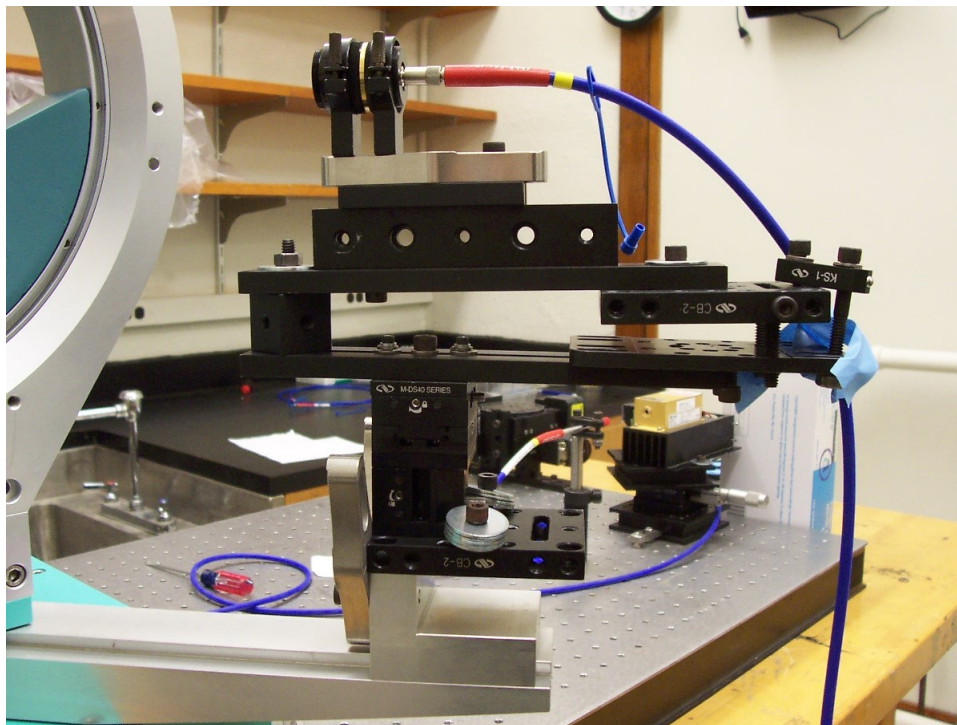
Figure 15. The 3 translation stages plus the screw and platform arrangement that provide all the needed motions for aligning the optical assembly on the mobile arm of the 4-circle diffractometer.
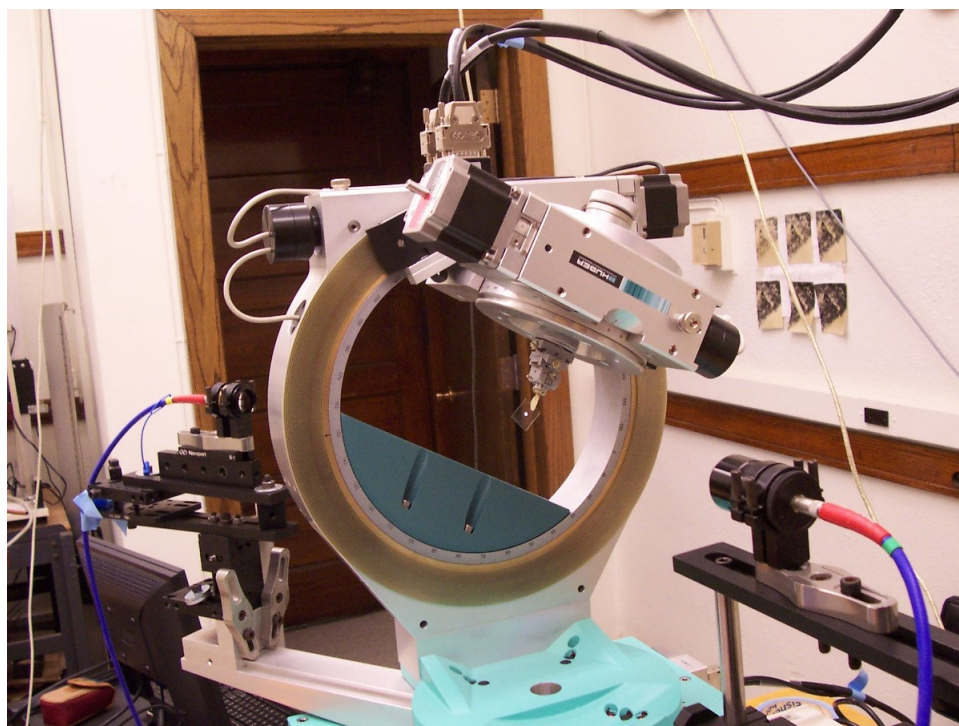


Figure 16. The four circles of the diffractometer: the fixed arm (theta ring), the mobile arm (tau), the Eulerian cradle (phi) and the chi-axis, where the sample is mounted.
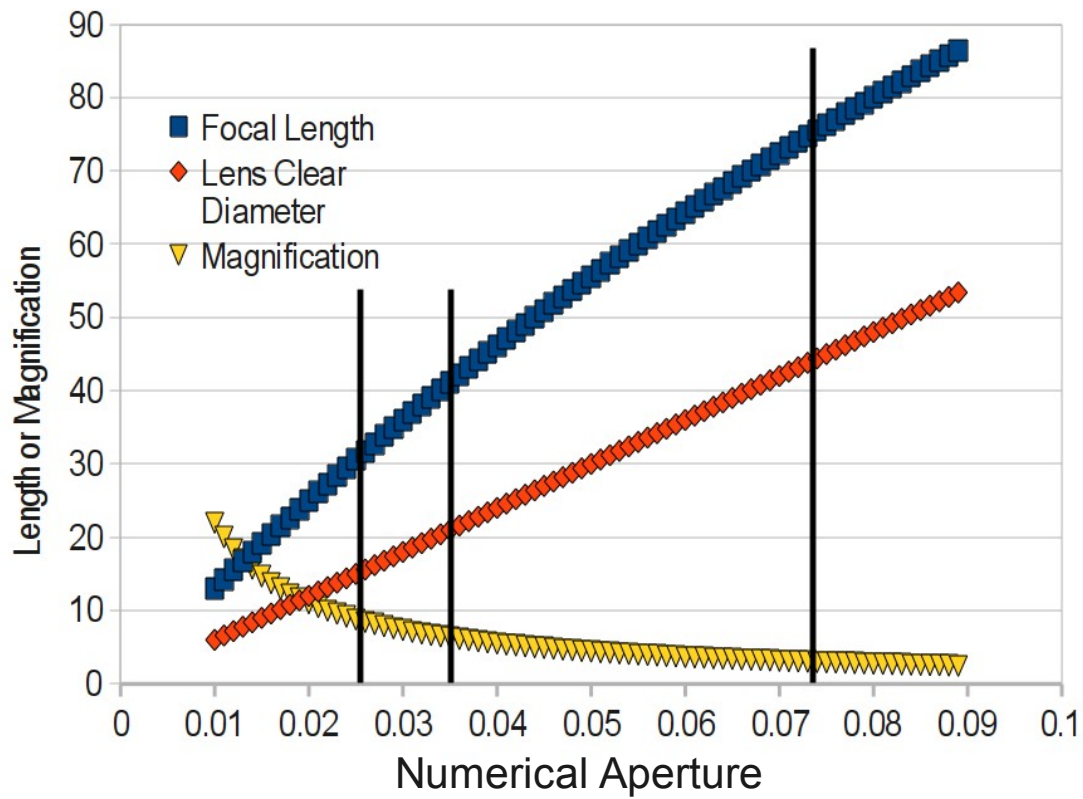
Figure 17. The relationship of the lens focal length, the required clear diameter, the magnification ratio, and the numerical aperture. The three vertical black bars correspond to commercially available lenses where the two leftmost bars are 25 mm diameter lenses and the rightmost is a 50 mm diameter lens.
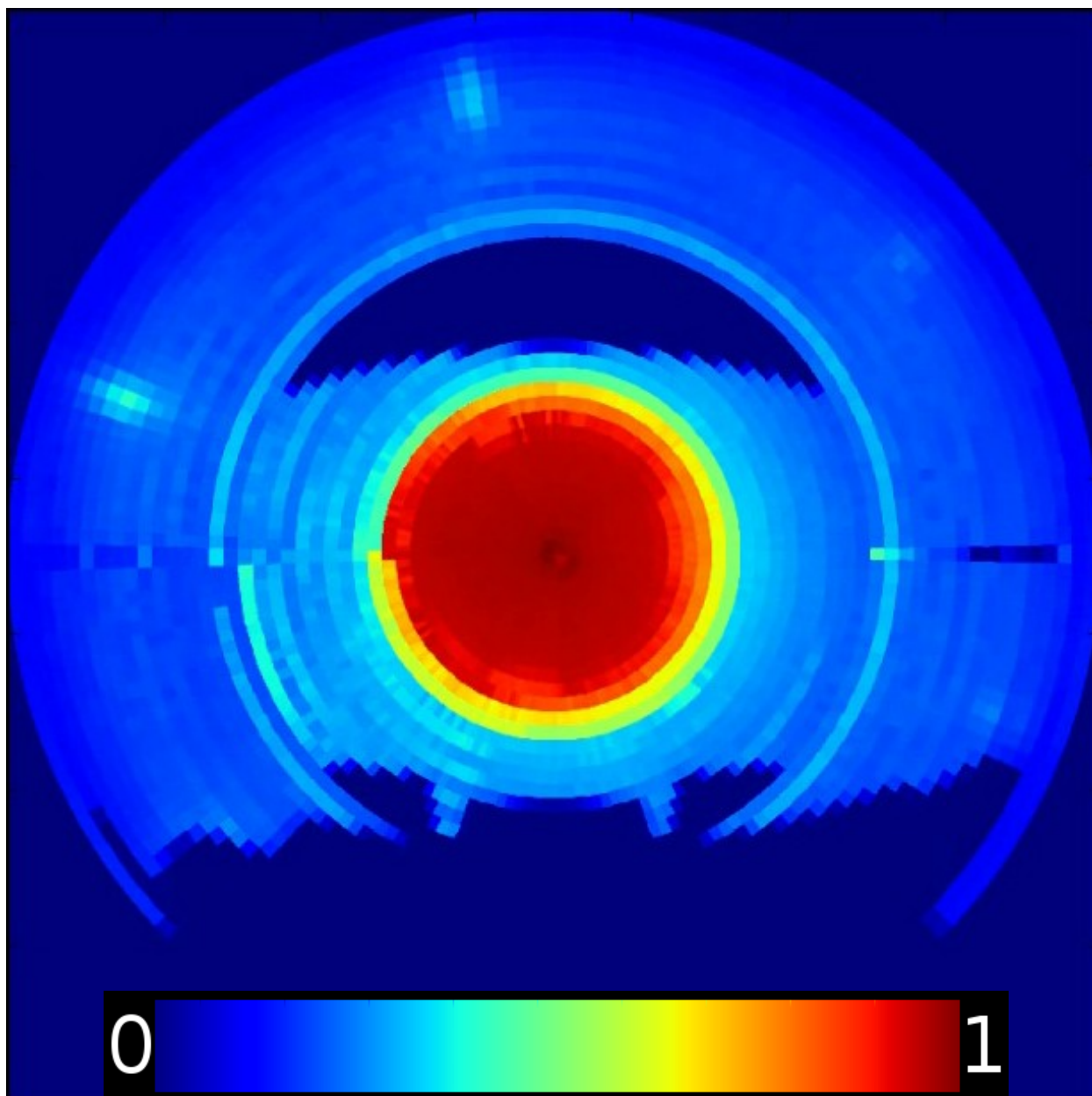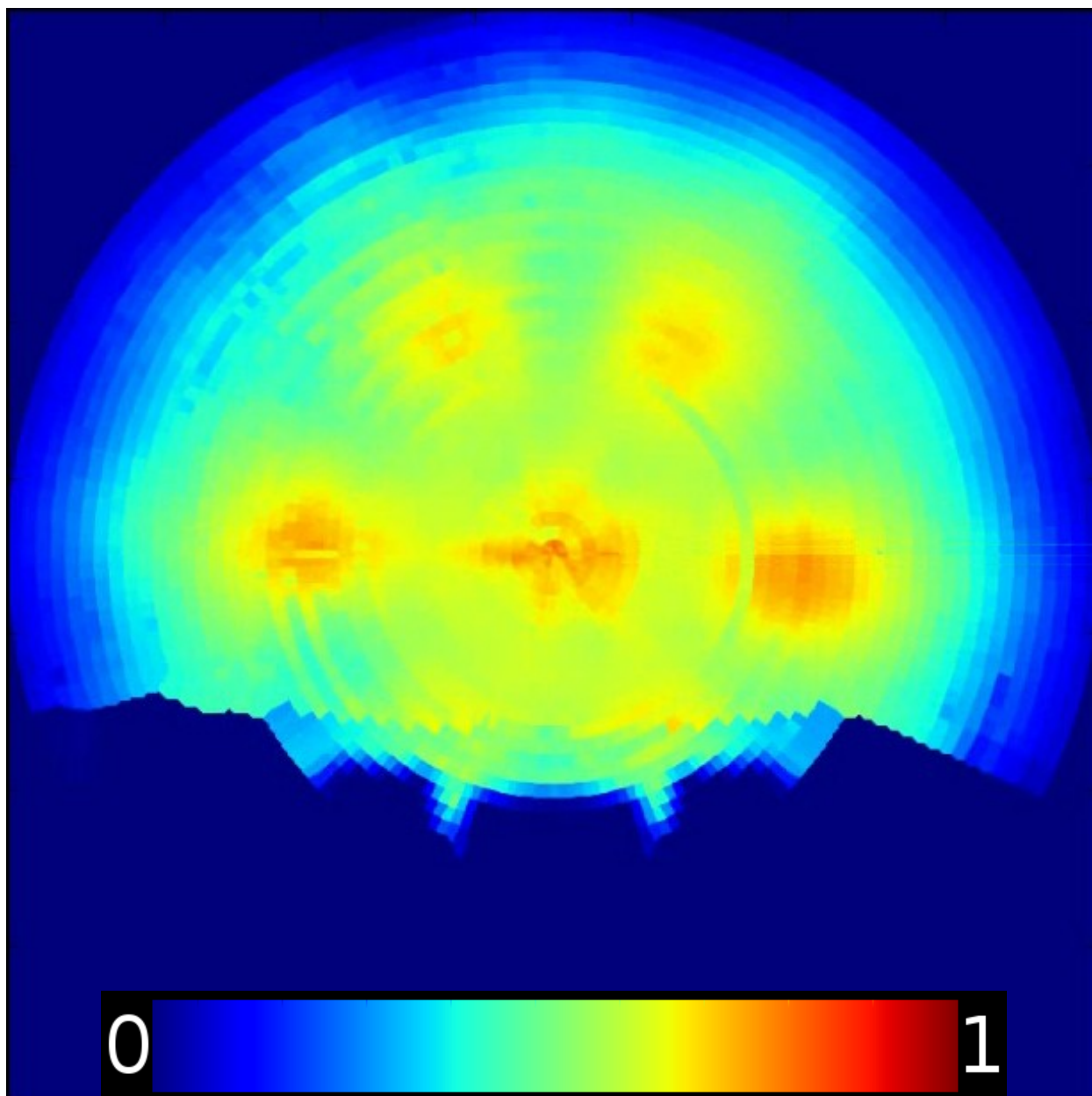
Figure 18. Polar plot of 720 nm light transmitted through a cuprous oxide photonic crystal with ~900 nm in-plane lattice vector. The center of the plot is light collected normal to the sample while at the edge of the plot the light is collected at 75° from the normal. Red regions have high intensity while dark blue regions have low intensity. There is a six-fold set of diffraction spots at ~60°, while a second six-fold set of spots is barely discernible at ~25°.

Figure 19. Polar plot of 700 nm light transmitted through a titanium dioxide photonic crystal with ~600 nm in-plane lattice vector (the colloidal diameter). The center of the plot is light incident normal to the sample while at the edge of the plot the light is incident at 75° from the normal. Red regions have high intensity while dark blue regions have low intensity. There is a six-fold set of diffuse diffraction spots at ~40°.

a)



b)



c)



Figure 20 (a) Two dimensional schematic of conformal deposition (yellow). The initial structure (blue) is more clearly seen in (b) where a continuous path exists between the source (S) and all the initial surface voxels. A one-voxel thick deposition occurred on the third iteration because each iteration increases the deposition thickness by one third the voxel diagonal. Every deposited voxel points (arrows) to the path providing the nearest initial surface. In each iteration, voids (white) adjacent to filled voxels have the minimum distance to the initial surface (blue) tested and if the distance is less than or equal to the current deposition thickness then the void is filled. Only a void's nearest neighbors are probed (in the order: north, east, south, west) to find the minimum distance, following the path along the arrows until an initial surface (blue) is reached and then the Euclidean distance is calculated. Ties for minimum distance go to the first probed path. Voxels deposited in iteration 10 (shaded yellow) pinched-off the path between the source and central region in (a), but deposition can continue outside the pinched-off region. (c) Range of calculated total fill fractions (black) after conformal deposition to the pinch-off point versus the analytical result of 0.9641 for a face centered cubic lattice of spheres (red line); (inset) pinch-off occurs here when the pore, centered on three touching spheres, is closed.
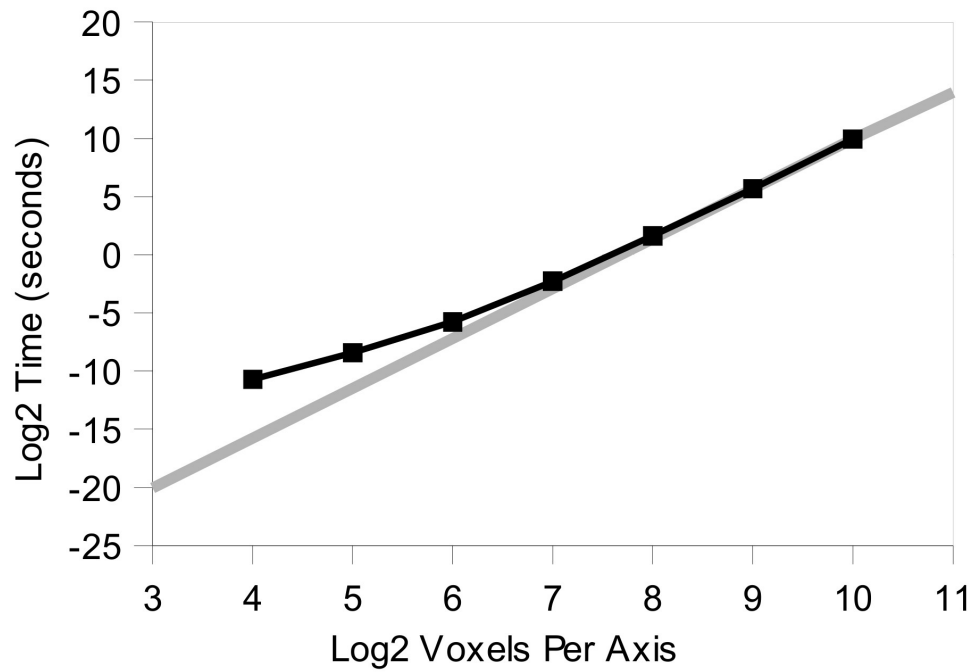
92
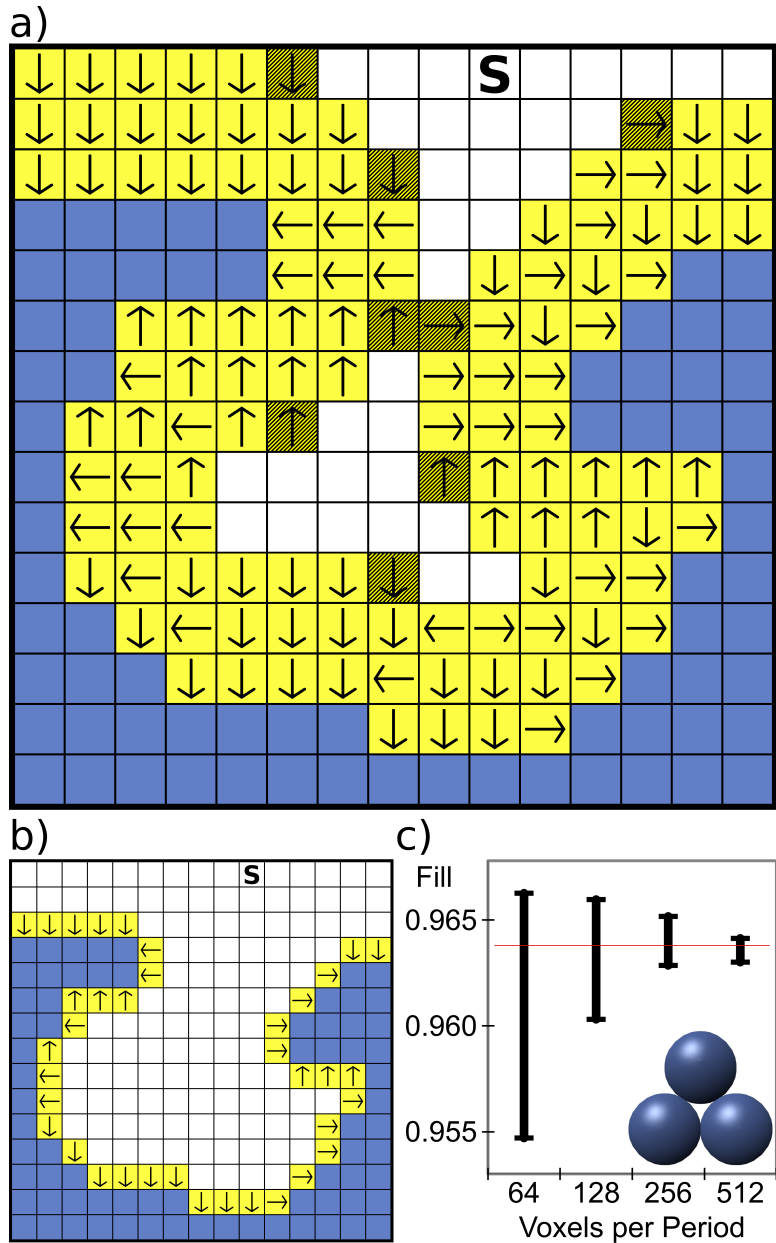
Figure 21. The scaling of computation time versus the number of voxel per axis (black). The scaling approaches the expected N4 asymptotic behavior (grey), which is plotted with a slope of 4 and passes through the data point at 1024 voxels per side.
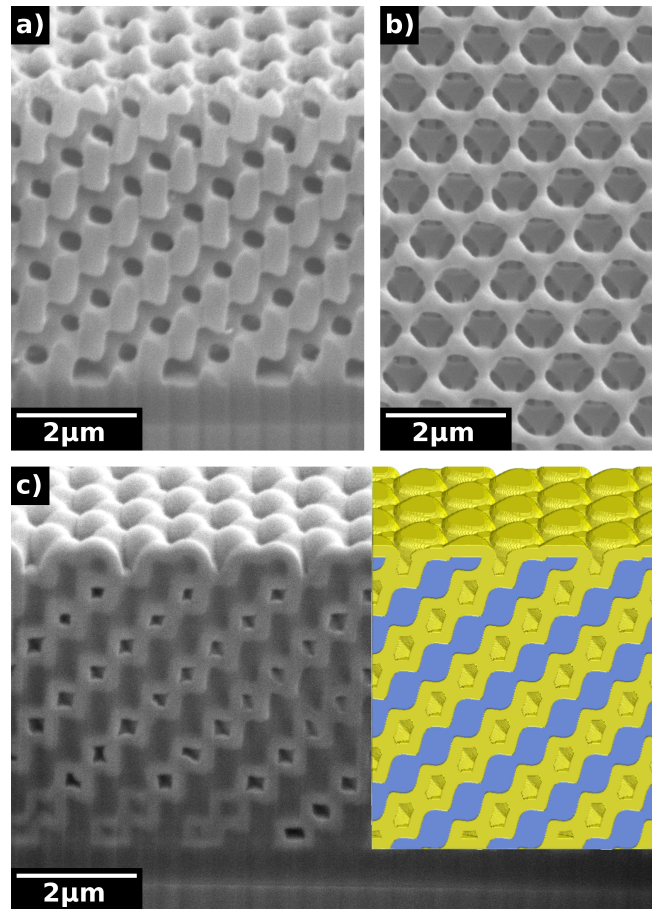
Fig. 22 (a) Focused-ion beam milled (FIB) cross-section of SU-8 photonic crystal template and the (b) top view. (c) FIB cross-section of template after 228 nm ALD shown beside the calculated structure (at right) showing polymer (blue) and alumina (yellow); in the micrograph, alumina is brighter than SU-8. The alumina thickness inside the structure is limited to ~177 nm due to pinch-off of the pores.
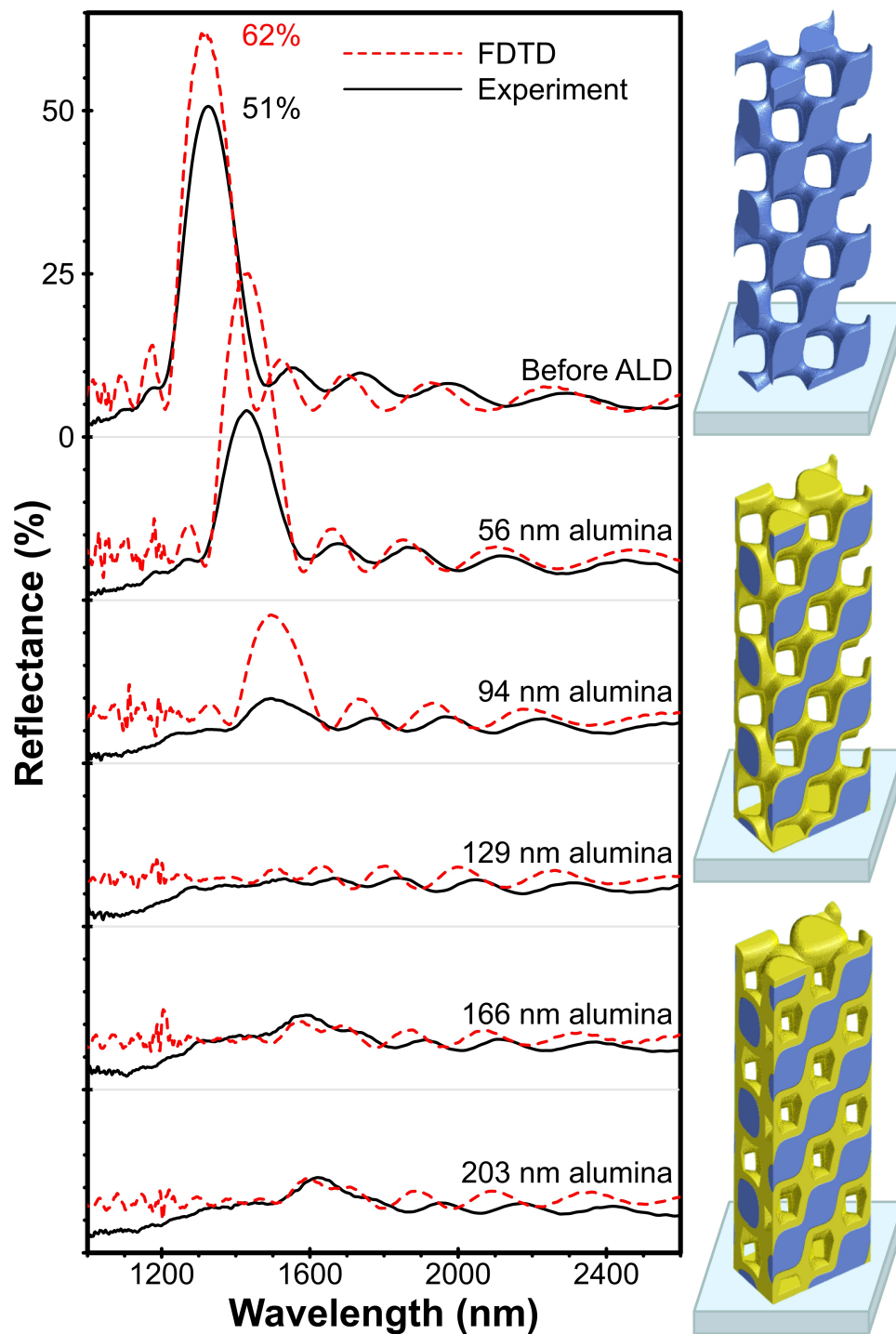
Figure 23. Comparison of experimental (solid black) and FDTD calculated (dashed red) reflectance; each curve is offset by 25% for clarity. The calculation unit cell showing the original template (top right), after 56 nm ALD (middle right), and after 129 nm (bottom right), showing the polymer (blue) and conformally deposited material (yellow).
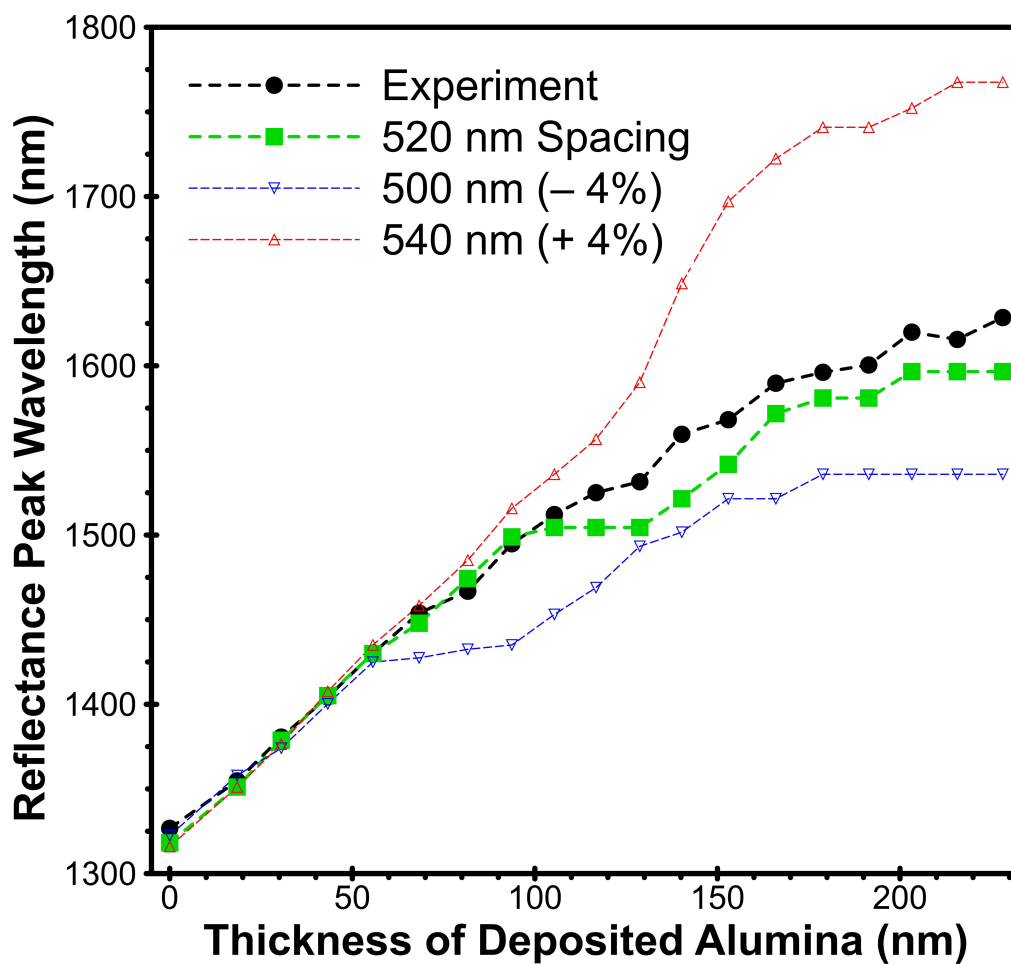
95

Figure 24. Evolution of experimental and FDTD calculated reflectance peak position during ALD of alumina on a SU-8 polymer template.
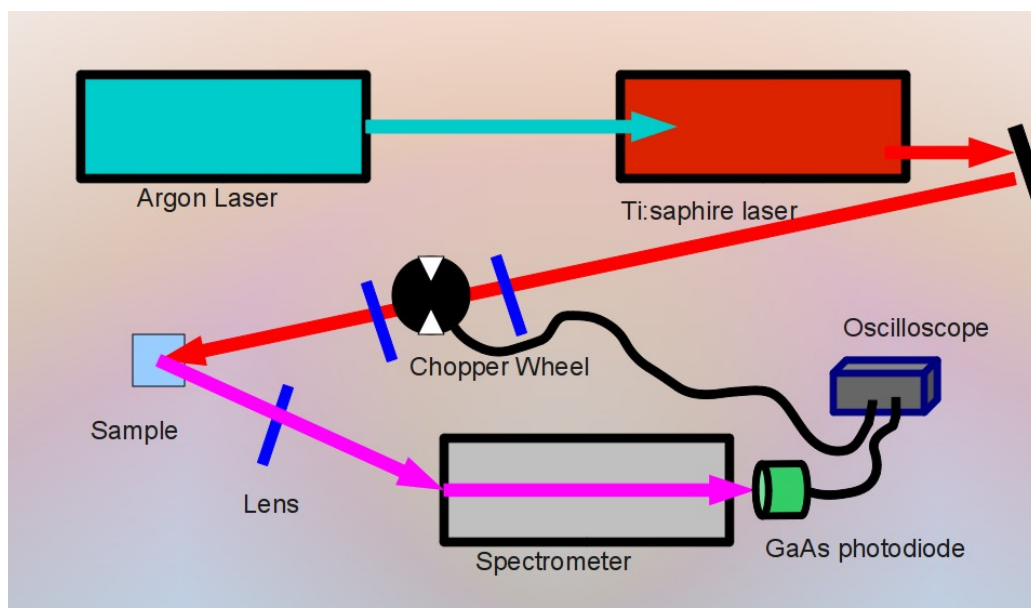
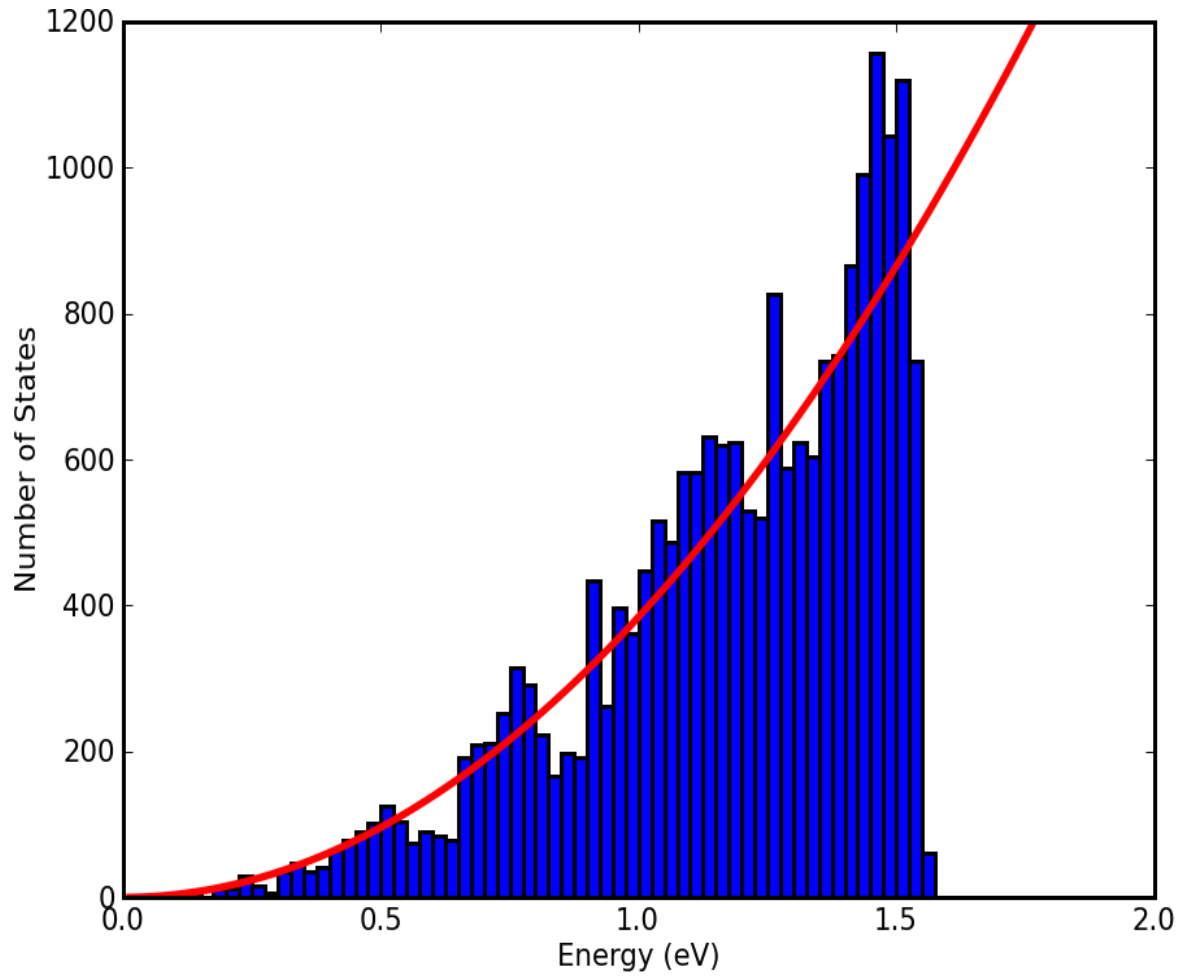Figure 25. Schematic of the lifetime measurement apparatus.

Figure 26. Number of electromagnetic modes versus the mode energy. The structure is calculated for an interference lithography pattern that is inverted in electro-deposited cuprous oxide. The red line depicts the number of modes that occur in a homogeneous dielectric material with the same average refractive index as the photonic crystal. This structure shows a sizable depression in the density of modes at about 0.9 eV.
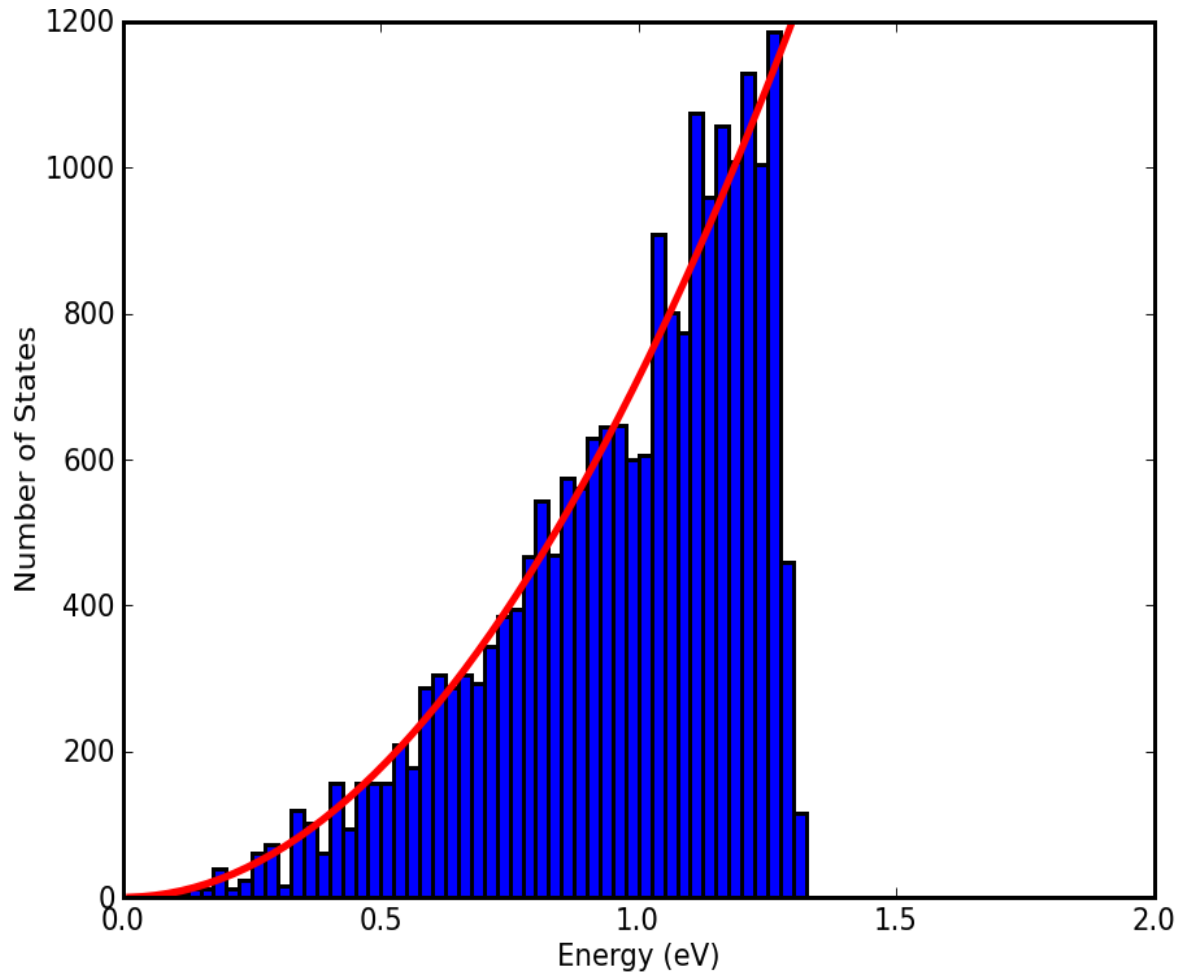
Figure 27. Number of electromagnetic modes versus the mode energy. The structure is calculated for an interference lithography pattern that is inverted in electro-deposited cuprous oxide. The red line depicts the number of modes that occur in a homogeneous dielectric material with the same average refractive index as the photonic crystal. This structure does not show significant depression in the number of modes. This photonic crystal has the same spacing but a lower filling fraction compared with the photonic crystal in Figure 26.
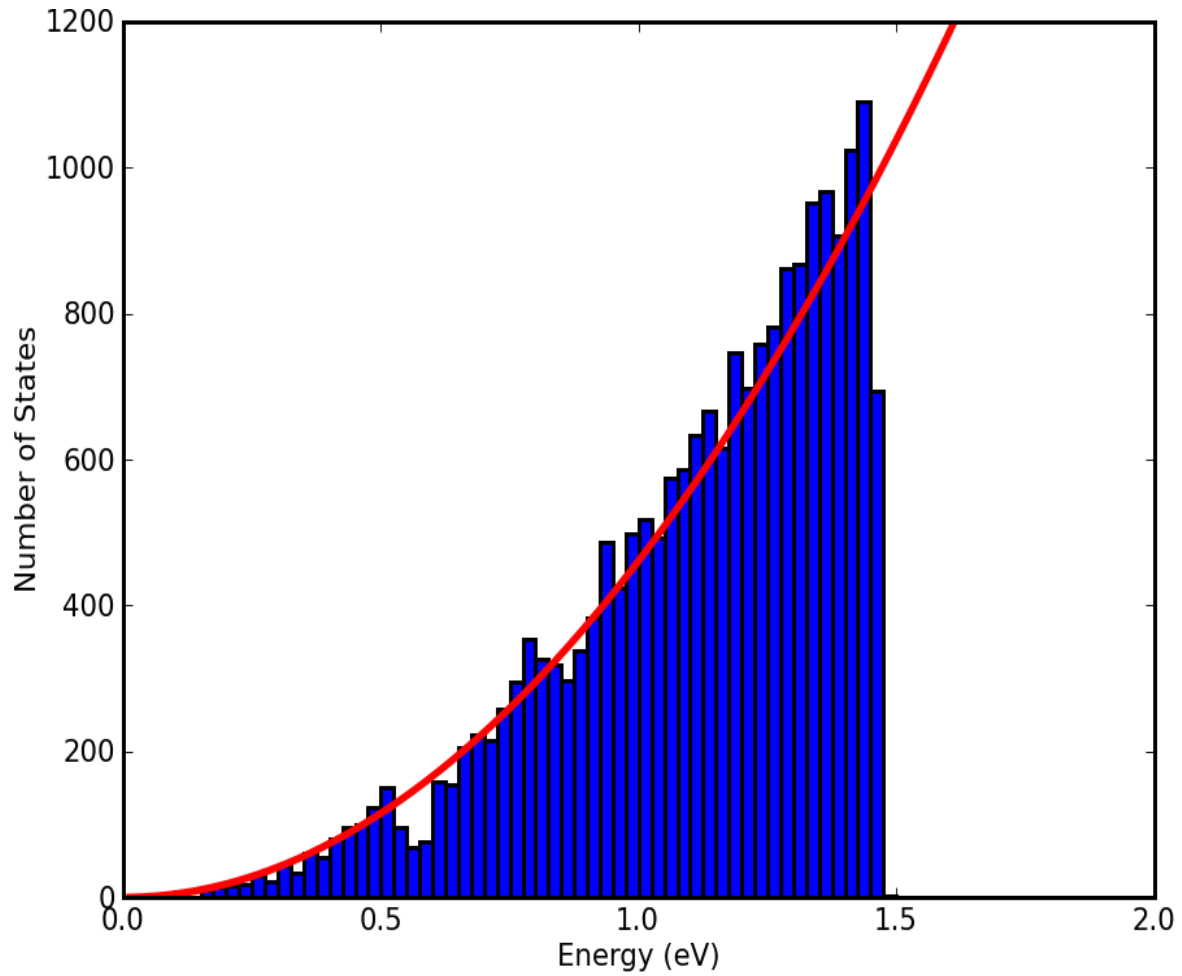
Figure 28. Number of electromagnetic modes versus the mode energy. The structure is calculated for an interference lithography pattern that is inverted in electro-deposited cuprous oxide. The red line depicts the number of modes that occur in a homogeneous dielectric material with the same average refractive index as the photonic crystal. This structure does not show significant depression in the number of modes. This photonic crystal has larger spacing but a the same filling fraction compared with the photonic crystal in Figure 26.
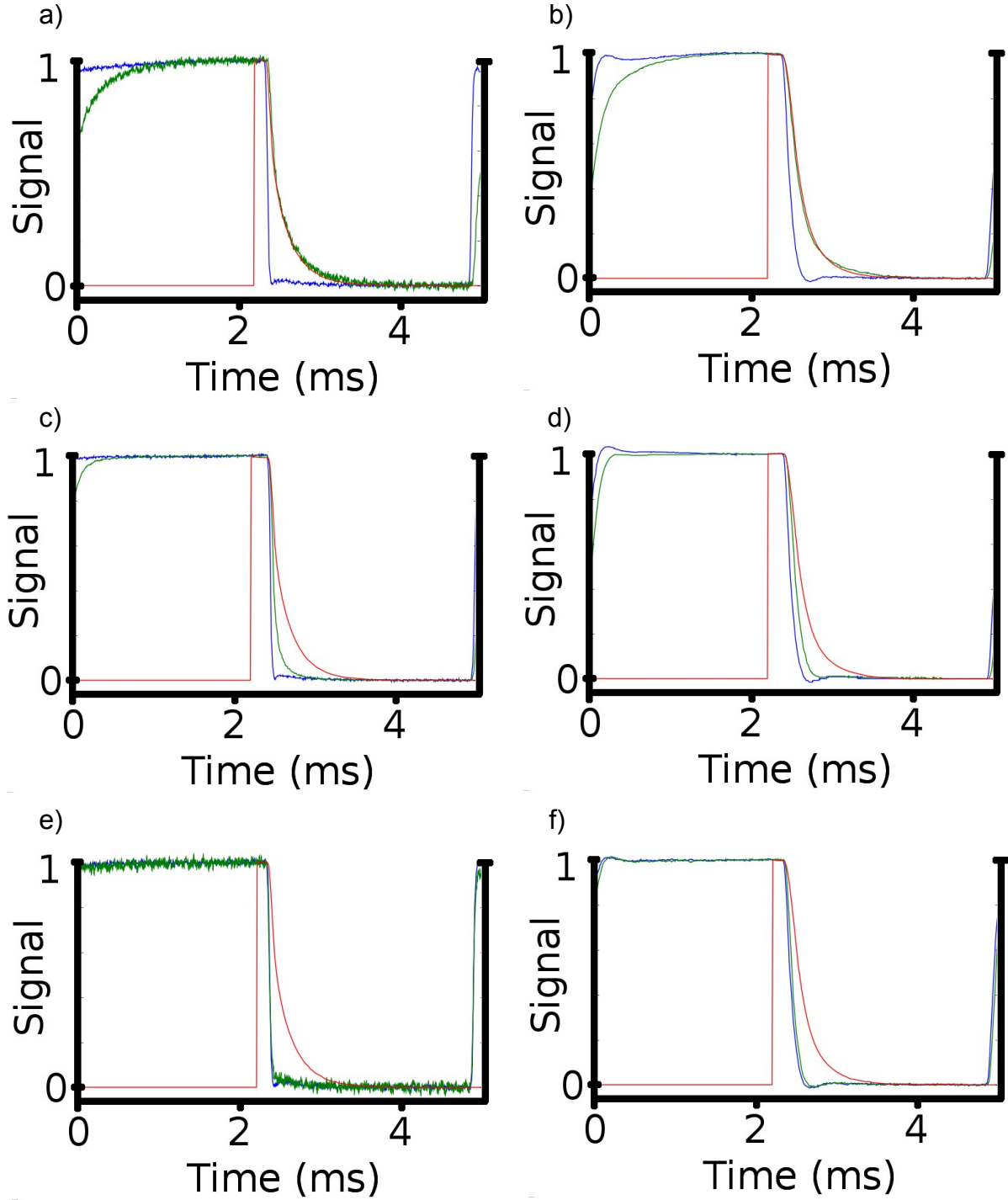
Figure 29. Life time measurements where the system response (blue) is convolved with a bi-exponential lifetime model, 70% at 40 µs and 30% at 220 µs, to obtain a curve (red) that can be compared with the collected signal (green). All curves are normalized. The leftmost plots, (a) (c) and (e) have a gain setting of 107 while the rightmost plots, (b), (d), (f) have a gain of 108. The topmost plots, (a) and (b) have 1% Nd doping. The middle plots (c) and (d) have 5% Nd, and the bottommost, (e) and (f) have 10%.

101

# CHAPTER 10

# REFERENCES

[1]     J.D. Joannopoulos, S.G. Johnson, J.N. Winn, and R.D. Meade, *Photonic crystals: molding the flow of light*, Princeton Univ Pr, 2008.

[2]     L. Rayleigh, "On the propagation of waves through a stratified medium, with special reference to the question of reflection," *Proceedings of the Royal Society of London. Series A, Containing Papers of a Mathematical and Physical Character*, 1912, pp. 207-226.

[3]     E. Yablonovitch, "Inhibited spontaneous emission in solid-state physics and electronics," *Physical review letters*, vol. 58, 1987, pp. 2059-2062.

[4]     S. John, "Strong localization of photons in certain disordered dielectric superlattices," *Physical Review Letters*, vol. 58, Jun. 1987, pp. 2486-2489.

[5]     C. Kittel and P. McEuen, *Introduction to solid state physics*, Wiley New York, 1996.

[6]     B.W. Batterman and H. Cole, "Dynamical diffraction of X rays by perfect crystals," *Reviews of modern physics*, vol. 36, 1964, pp. 681-717.

[7]     A. Brzezinski, J.T. Lee, J.D. Slinker, G.G. Malliaras, P.V. Braun, and P. Wiltzius, "Enhanced emission from fcc fluorescent photonic crystals," *Physical Review B*, vol. 77, 2008, p. 233106.

[8]     N.W. Ashcroft and N.D. Mermin, "Solid state physics," *Holt, Rinehart and Winston, New York*, vol. 826, 1976.

[9]     W. Lee, S. A. Pruzinsky, and P. V. Braun, "Multi-Photon Polymerization of Waveguide Structures Within Three-Dimensional Photonic Crystals," *Advanced Materials*, vol. 14, 2002, pp. 271-274.

[10]   S. Noda, K. Tomoda, N. Yamamoto, and A. Chutinan, "Full Three-Dimensional Photonic Bandgap Crystals at Near-Infrared Wavelengths," *Science*, vol. 289, Jul. 2000, pp. 604-606.

[11]   A. Mekis, J.C. Chen, I. Kurland, S. Fan, P.R. Villeneuve, and J.D. Joannopoulos, "High transmission through sharp bends in photonic crystal waveguides," *Physical Review Letters*, vol. 77, 1996, pp. 3787-3790.

[12]   S.Y. Lin, E. Chow, V. Hietala, P.R. Villeneuve, and J.D. Joannopoulos, "Experimental demonstration of guiding and bending of electromagnetic waves in a photonic crystal," *Science*, vol. 282, 1998, p. 274.

[13]   M. Ibanescu, Y. Fink, S. Fan, E.L. Thomas, and J.D. Joannopoulos, "An all-dielectric coaxial waveguide," *Science*, vol. 289, 2000, p. 415.

[14]   Y. Fink, J.N. Winn, S. Fan, C. Chen, J. Michel, J.D. Joannopoulos, and E.L. Thomas, "A dielectric omnidirectional reflector," *Science*, vol. 282, 1998, p. 1679.

[15]   A. Bruyant, G. Lérondel, P.J. Reece, and M. Gal, "All-silicon omnidirectional mirrors based on one-dimensional photonic crystals," *Applied Physics Letters*, vol. 82, 2003, p. 3227.

[16]   F. De Martini and G.R. Jacobovitz, "Anomalous spontaneous–stimulated-decay phase transition and zero-threshold laser action in a microscopic cavity," *Physical review letters*, vol. 60, 1988, pp. 1711-1714.

[17] J.K. Hwang, H.Y. Ryu, D.S. Song, I.Y. Han, H.W. Song, H.K. Park, Y.H. Lee, and D.H. Jang, "Room-temperature triangular-lattice two-dimensional photonic band gap lasers operating at 1.54 m," *Applied Physics Letters*, vol. 76, 2000, p. 2982.

[18] I.I. Tarhan and G.H. Watson, "Photonic band structure of fcc colloidal crystals," *Physical review letters*, vol. 76, 1996, pp. 315-318.

[19] W.L. Vos, R. Sprik, A. van Blaaderen, A. Imhof, A. Lagendijk, and G.H. Wegdam, "Strong effects of photonic band structures on the diffraction of colloidal crystals," *Physical Review B*, vol. 53, 1996, pp. 16231-16235.

[20] J. Wijnhoven and W.L. Vos, "Preparation of photonic crystals made of air spheres in titania," *Science*, vol. 281, 1998, p. 802.

[21] Y.H. Ye, F. LeBlanc, and A. Haché, "Self-assembling three-dimensional colloidal photonic crystal structure with high crystalline quality," *Applied Physics Letters*, vol. 78, 2001, p. 52.

[22] W. Lee, A. Chan, M.A. Bevan, J.A. Lewis, and P.V. Braun, "Nanoparticle-mediated epitaxial assembly of colloidal crystals on patterned substrates," *Langmuir*, vol. 20, 2004, pp. 5262-5270.

[23] Y. Lu, Y. Yin, B. Gates, and Y. Xia, "Growth of large crystals of monodispersed spherical colloids in fluidic cells fabricated using non-photolithographic methods," *Langmuir*, vol. 17, 2001, pp. 6344-6350.

[24] P. Pieranski, "Colloidal crystals," *Contemporary Physics*, vol. 24, 1983, p. 25.

[25] M. Campbell, D.N. Sharp, M.T. Harrison, R.G. Denning, and A.J. Turberfield, "Fabrication of photonic crystals for the visible spectrum by holographic lithography," *Nature*, vol. 404, Mar. 2000, pp. 53-56.

[26] C.K. Ullal, M. Maldovan, M. Wohlgemuth, E.L. Thomas, C.A. White, and S. Yang, "Triply periodic bicontinuous structures through interference lithography: a level-set approach," *Journal of the Optical Society of America A*, vol. 20, 2003, pp. 948-954.

[27] S. Yang, M. Megens, J. Aizenberg, P. Wiltzius, P.M. Chaikin, and W.B. Russel, "Creating periodic three-dimensional structures by multibeam interference of visible laser," *Chemistry of Materials*, vol. 14, 2002, pp. 2831-2833.

[28] Y.V. Miklyaev, D.C. Meisel, A. Blanco, G. Von Freymann, K. Busch, W. Koch, C. Enrich, M. Deubel, and M. Wegener, "Three-dimensional face-centered-cubic photonic crystal templates by laser holography: fabrication, optical characterization, and band-structure calculations," *Applied Physics Letters*, vol. 82, Feb. 2003, pp. 1284-1286.

[29] J. Serbin, A. Egbert, A. Ostendorf, B.N. Chichkov, R. Houbertz, G. Domann, J. Schulz, C. Cronauer, L. Fröhlich, and M. Popall, "Femtosecond laser-induced two-photon polymerization of inorganic organic hybrid materials for applications in photonics," *Optics letters*, vol. 28, 2003, pp. 301-303.

[30] M. Deubel, G. von Freymann, M. Wegener, S. Pereira, K. Busch, and C.M. Soukoulis, "Direct laser writing of three-dimensional photonic-crystal templates for telecommunications," *Nat Mater*, vol. 3, Jul. 2004, pp. 444-447.

[31] M. Albota, D. Beljonne, J.L. Brédas, J.E. Ehrlich, J.Y. Fu, A.A. Heikal, S.E. Hess, T. Kogej, M.D. Levin, and S.R. Marder, "Design of organic molecules with large two-photon absorption cross sections," *Science*, vol. 281, 1998, p. 1653.

[32] S.A. Pruzinsky and P.V. Braun, "Fabrication and characterization of two-photon

polymerized features in colloidal crystals," *Advanced Functional Materials*, vol. 15, 2005, pp. 1995-2004.

[33] D.E. Spence, P.N. Kean, and W. Sibbett, "60-fsec pulse generation from a self-mode-locked Ti: sapphire laser," *Optics Letters*, vol. 16, 1991, pp. 42-44.

[34] M. Farsari, G. Filippidis, K. Sambani, T.S. Drakakis, and C. Fotakis, "Two-photon polymerization of an Eosin Y-sensitized acrylate composite," *Journal of Photochemistry & Photobiology, A: Chemistry*, vol. 181, 2006, pp. 132-135.

[35] K.S. Lee, R.H. Kim, D.Y. Yang, and S.H. Park, "Advances in 3D nano/microfabrication using two-photon initiated polymerization," *Progress in Polymer Science*, 2008.

[36] S. Jeon, E. Menard, J.U. Park, J. Maria, M. Meitl, J. Zaumseil, and J.A. Rogers, "Three-dimensional nanofabrication with rubber stamps and conformable photomasks," *Advanced Materials*, vol. 16, 2004, pp. 1369-1373.

[37] D. Shir, E.C. Nelson, Y.C. Chen, A. Brzezinski, H. Liao, P.V. Braun, P. Wiltzius, K.H.A. Bogart, and J.A. Rogers, "Three dimensional silicon photonic crystals fabricated by two photon phase mask lithography," *Applied Physics Letters*, vol. 94, Jan. 2009, pp. 011101-3.

[38] R. Rumpf and E. Johnson, "Comprehensive modeling of near-field nano-patterning," *Optics Express*, vol. 13, 2005, pp. 7198-7208.

[39] K.K. Seet, V. Mizeikis, S. Matsuo, S. Juodkazis, and H. Misawa, "Three-dimensional spiral-architecture photonic crystals obtained by direct laser writing," *Advanced Materials(FRG)*, vol. 17, 2005, pp. 541-545.

[40] H. Lorenz, M. Despont, N. Fahrni, N. LaBianca, P. Renaud, and P. Vettiger, "SU-8: a low-cost negative resist for MEMS," *Journal of Micromechanics and Microengineering*, vol. 7, 1997, pp. 121-124.

[41] K. Busch, G.V. Freymann, S. Linden, S. Mingaleev, L. Tkeshelashvili, and M. Wegener, "Periodic nanostructures for photonics," *Physics Reports*, vol. 444, Jun. 2007, pp. 101-202.

[42] R.G. Denning, A.J. Turberfield, and C.J. Summers, "Infiltration and Inversion of Holographically Defined Polymer Photonic Crystal Templates by Atomic Layer Deposition*," *Adv. Mater*, vol. 18, 2006, pp. 1561-1565.

[43] H. Miguez, F. Meseguer, C. Lopez, M. Holgado, G. Andreasen, A. Mifsud, and V. Forness, "Germanium FCC structure from a colloidal crystal template," *Langmuir*, vol. 16, 2000, pp. 4405-4408.

[44] A. Stein and R.C. Schroden, "Colloidal crystal templating of three-dimensionally ordered macroporous solids: materials for photonics and beyond," *Current Opinion in Solid State & Materials Science*, vol. 5, 2001, pp. 553-564.

[45] R.M. Almeida and S. Portal, "Photonic band gap structures by sol–gel processing," *Current opinion in solid state & materials science*, vol. 7, 2003, pp. 151-157.

[46] P.V. Braun and P. Wiltzius, "Macroporous materials—Electrochemically grown photonic crystals," *Current Opinion in Colloid & Interface Science*, vol. 7, 2002, pp. 116-123.

[47] I.B. Divliansky, A. Shishido, I.C. Khoo, T.S. Mayer, D. Pena, S. Nishimura, C.D. Keating, and T.E. Mallouk, "Fabrication of two-dimensional photonic crystals using interference lithography and electrodeposition of CdSe," *Applied Physics Letters*,

vol. 79, 2001, p. 3392.

[48] T. Sumida, Y. Wada, T. Kitamura, and S. Yanagida, "Macroporous ZnO films electrochemically prepared by templating of opal films," *Chemistry Letters*, vol. 30, 2001, pp. 38-39.

[49] M. Miyake, Y.C. Chen, P.V. Braun, and P. Wiltzius, "Fabrication of Three-Dimensional Photonic Crystals Using Multibeam Interference Lithography and Electrodeposition," *Advanced Materials*, vol. 21, 2009.

[50] H.O. Pierson, *Handbook of chemical vapor deposition: principles, technology, and applications*, Noyes Pubns, 1999.

[51] F. Pérez-Willard, S. John, M. Wegener, and G.A. Ozin, "New Route to Three-Dimensional Photonic Bandgap Materials: Silicon Double Inversion of Polymer Templates*," *Adv. Mater*, vol. 18, 2006, pp. 457-460.

[52] M. Leskelä and M. Ritala, "Atomic layer deposition (ALD): from precursors to thin film structures," *Thin Solid Films*, vol. 409, 2002, pp. 138-146.

[53] C. López, "Materials aspects of photonic crystals," *Advanced Materials*, vol. 15, 2003, pp. 1679-1704.

[54] V. Ramanan, E. Nelson, A. Brzezinski, P.V. Braun, and P. Wiltzius, "Three dimensional silicon-air photonic crystals with controlled defects using interference lithography," *Applied Physics Letters*, vol. 92, 2008, p. 173304.

[55] F. García-Santamaría, J.F. Galisteo-López, P.V. Braun, and C. López, "Optical diffraction and high-energy features in three-dimensional photonic crystals," *Physical Review B*, vol. 71, 2005, p. 195112.

[56] Y.C. Chen, J.B. Geddes, III, J.T. Lee, P.V. Braun, and P. Wiltzius, "Holographically fabricated photonic crystals with large reflectance," *Applied Physics Letters*, vol. 91, Dec. 2007, pp. 241103-3.

[57] W.L. Vos and H.M. van Driel, "Higher order Bragg diffraction by strongly photonic fcc crystals: onset of a photonic bandgap," *Physics Letters A*, vol. 272, 2000, pp. 101-106.

[58] I.S. Nikolaev, P. Lodahl, and W.L. Vos, "Quantitative analysis of directional spontaneous emission spectra from light sources in photonic crystals," *Physical Review A*, vol. 71, 2005, p. 53813.

[59] A. Richel, N.P. Johnson, and D.W. McComb, "Observation of Bragg reflection in photonic crystals synthesized from air spheres in a titania matrix," *Applied Physics Letters*, vol. 76, 2000, p. 1816.

[60] J.F. Galisteo Lòpez and W.L. Vos, "Angle-resolved reflectivity of single-domain photonic crystals: Effects of disorder," *Physical Review E*, vol. 66, 2002, p. 36616.

[61] P. Lodahl, A. Floris van Driel, I.S. Nikolaev, A. Irman, K. Overgaag, D. Vanmaekelbergh, and W.L. Vos, "Controlling the dynamics of spontaneous emission from quantum dots by photonic crystals," *Nature*, vol. 430, 2004, pp. 654-657.

[62] M. Notomi, "Theory of light propagation in strongly modulated photonic crystals: Refractionlike behavior in the vicinity of the photonic band gap," *Physical Review B*, vol. 62, 2000, pp. 10696-10705.

[63] D. Englund, D. Fattal, E. Waks, G. Solomon, B. Zhang, T. Nakaoka, Y. Arakawa, Y. Yamamoto, and J. Vu kovi, "Controlling the spontaneous emission rate of single quantum dots in a two-dimensional photonic crystal," *Physical review letters*, vol.

95, 2005, p. 13904.

[64]   H.P. Schriemer, H.M. van Driel, A.F. Koenderink, and W.L. Vos, "Modified spontaneous emission spectra of laser dye in inverse opal photonic crystals," *Physical Review A*, vol. 63, 2000, p. 11801.

[65]   S. Noda, K. Tomoda, N. Yamamoto, and A. Chutinan, "Full Three-Dimensional Photonic Bandgap Crystals at Near-Infrared Wavelengths," *Science*, vol. 289, Jul. 2000, pp. 604-606.

[66]   Z.Y. Li and L.L. Lin, "Photonic band structures solved by a plane-wave-based transfer-matrix method," *Physical Review E*, vol. 67, 2003, p. 46607.

[67]   A.F. Koenderink and W.L. Vos, "Light Exiting from Real Photonic Band Gap Crystals is Diffuse and Strongly Directional," *Physical Review Letters*, vol. 91, Nov. 2003, p. 213902.

[68]   A. Taflove and S.C. Hagness, *Computational electrodynamics: the finite-difference time-domain method*, Artech House Norwood, MA, 1995.

[69]   A. Farjadpour, D. Roundy, A. Rodriguez, M. Ibanescu, P. Bermel, J.D. Joannopoulos, S.G. Johnson, and G.W. Burr, "Improving accuracy by subpixel smoothing in the finite-difference time domain," *Optics Letters*, vol. 31, Oct. 2006, pp. 2972-2974.

[70]   J.D. Joannopoulos, S.G. Johnson, J.N. Winn, and R.D. Meade, *Photonic crystals: molding the flow of light*, Princeton Univ Pr, 2008.

[71]   S.G. Johnson and J.D. Joannopoulos, "Block-iterative frequency-domain methods for Maxwell's equations in a planewave basis," *vacuum*, vol. 83, 1999, pp. 967-970.

[72]   J. Moon, Y. Xu, Y. Dan, S. -M. Yang, A. T. Johnson, and S. Yang, "Triply Periodic Bicontinuous Structures as Templates for Photonic Crystals: A Pinch-off Problem," *Advanced Materials*, vol. 19, 2007, pp. 1510-1514.

[73]   J.A. Lewis and P.V. Braun, "Direct-Write Assembly of Three-Dimensional Photonic Crystals: Conversion of Polymer Scaffolds to Silicon Hollow-Woodpile Structures*," *Adv. Mater*, vol. 18, 2006, pp. 461-465.

[74]   J.J. Wierer, A. David, and M.M. Megens, "III-nitride photonic-crystal light-emitting diodes with high extraction efficiency," *Nat Photon*, vol. 3, Mar. 2009, pp. 163-169.

[75]   M. Boroditsky, T.F. Krauss, R. Coccioli, R. Vrijen, R. Bhat, and E. Yablonovitch, "Light extraction from optically pumped light-emitting diode by thin-slab photonic crystals," *Applied Physics Letters*, vol. 75, 1999, p. 1036.

[76]   T. Yamasaki and T. Tsutsui, "Spontaneous emission from fluorescent molecules embedded in photonic crystals consisting of polystyrene microspheres," *Applied Physics Letters*, vol. 72, 1998, p. 1957.

[77]   E.P. Petrov, V.N. Bogomolov, I.I. Kalosha, and S.V. Gaponenko, "Spontaneous emission of organic molecules embedded in a photonic crystal," *Physical Review Letters*, vol. 81, 1998, pp. 77-80.

[78]   M. Megens, J. Wijnhoven, A. Lagendijk, and W.L. Vos, "Fluorescence lifetimes and linewidths of dye in photonic crystals," *Physical Review A*, vol. 59, 1999, pp. 4727-4731.

[79]   S.V. Gaponenko, V.N. Bogomolov, E.P. Petrov, A.M. Kapitonov, D.A. Yarotsky, I.I. Kalosha, A.A. Eychmueller, A.L. Rogach, J. McGilp, and U. Woggon,

"Spontaneous emission of dye molecules, semiconductor nanocrystals, and rare-earth ions in opal-based photonic crystals," *Journal of lightwave technology*, vol. 17, 1999, p. 2128.

[80] L. Bechger, P. Lodahl, and W.L. Vos, "Directional fluorescence spectra of laser dye in opal and inverse opal photonic crystals," *J. Phys. Chem. B*, vol. 109, 2005, pp. 9980-9988.

[81] M. Li, P. Zhang, J. Li, J. Zhou, A. Sinitskii, V. Abramova, S.O. Klimonsky, and Y.D. Tretyakov, "Directional emission from rare earth ions in inverse photonic crystals," *Applied Physics B: Lasers and Optics*, vol. 89, 2007, pp. 251-255.

[82] Z.A. Sechrist, B.T. Schwartz, J.H. Lee, J.A. McCormick, R. Piestun, W. Park, and S.M. George, "Modification of opal photonic crystals using Al 2 O 3 atomic layer deposition," *Chem. Mat*, vol. 18, 2006, pp. 3562–3570.

[83] R. Sprik, B. van Tiggelen, and A. Lagendijk, "Optical emission in periodic dielectrics," *EPL (Europhysics Letters)*, vol. 35, 1996, pp. 265-270.

[84] M. Knez, K. Nielsch, and L. Niinist, "Synthesis and Surface Engineering of Complex Nanostructures by Atomic Layer Deposition," *Advanced Materials*, vol. 19, 2007, pp. 3425-3438.

[85] E.F. Schubert and J.K. Kim, "Solid-State Light Sources Getting Smart," *Science*, vol. 308, May. 2005, pp. 1274-1278.

[86] A. Mekis, J.C. Chen, I. Kurland, S. Fan, P.R. Villeneuve, and J.D. Joannopoulos, "High Transmission through Sharp Bends in Photonic Crystal Waveguides," *Physical Review Letters*, vol. 77, Oct. 1996, p. 3787.

[87] W. Lee, S. A. Pruzinsky, and P. V. Braun, "Multi-Photon Polymerization of Waveguide Structures Within Three-Dimensional Photonic Crystals," *Advanced Materials*, vol. 14, 2002, pp. 271-274.

[88] S.Y. Lin, J.G. Fleming, D.L. Hetherington, B.K. Smith, R. Biswas, K.M. Ho, M.M. Sigalas, W. Zubrzycki, S.R. Kurtz, and J. Bur, "A three-dimensional photonic crystal operating at infrared wavelengths," *Nature*, vol. 394, Jul. 1998, pp. 251-253.

[89] Stephanie A. Rinne, Florencio Garc|[iacute]|a-Santamar|[iacute]|a, and Paul V. Braun, "Embedded cavities and waveguides in three-dimensional silicon photonic crystals," Dec. 2007.

[90] G. Gratson, F. García-Santamaría, V. Lousse, M. Xu, S. Fan, J. A. Lewis, and P. V. Braun, "Direct-Write Assembly of Three-Dimensional Photonic Crystals: Conversion of Polymer Scaffolds to Silicon Hollow-Woodpile Structures," *Advanced Materials*, vol. 18, 2006, pp. 461-465.

[91] F. García-Santamaría, M. Xu, V. Lousse, S. Fan, P.V. Braun, and J.A. Lewis, "AGermanium Inverse Woodpile Structure with a Large Photonic Band Gap*," *Adv. Mater*, vol. 19, 2007, pp. 1567-1570.

[92] J. King, E. Graugnard, O. M. Roche, D. N. Sharp, J. Scrimgeour, R. G. Denning, A. J. Turberfield, and C. J. Summers, "Infiltration and Inversion of Holographically Defined Polymer Photonic Crystal Templates by Atomic Layer Deposition," *Advanced Materials*, vol. 18, 2006, pp. 1561-1565.

[93] J. King, D. P. Gaillot, E. Graugnard, and C. J. Summers, "Conformally Back-Filled, Non-close-packed Inverse-Opal Photonic Crystals," *Advanced Materials*, vol. 18, 2006, pp. 1063-1067.

[94]  D. Gaillot and D. School of Materials Science and Engineering, Georgia Institute of Technology, Atlanta, Georgia 30332-0245, USA, "Photonic band gaps in highly conformal inverse-opal based photonic crystals," *Physical Review B*, vol. 72, p. 205109.

[95]  J.W. Rinne and P. Wiltzius, "Design of holographic structures using genetic algorithms," *Optics Express*, vol. 14, Oct. 2006, pp. 9909-9916.

[96]  M. Maldovan, C.K. Ullal, W.C. Carter, and E.L. Thomas, "Exploring for 3D photonic bandgap structures in the 11 f.c.c. space groups," *Nat Mater*, vol. 2, Oct. 2003, pp. 664-667.

[97]  J.H. Moon, S. Yang, W. Dong, J.W. Perry, A. Adibi, and S. Yang, "Core-shell diamond-like silicon photonic crystals from 3D polymer templates created by holographic lithography," *Optics Express*, vol. 14, Jun. 2006, pp. 6297-6302.

[98]  Richard Courant, *On the partial difference equations of mathematical physics*, (New York): Courant Institute of Mathematical Sciences, New York University, 1956.

[99]  W.G.M. Geraets, A.N.V. Daatselaar, and J.G.C. Verheij, "An efficient filling algorithm for counting regions," *Computer Methods and Programs in Biomedicine*, vol. 76, Oct. 2004, pp. 1-11.

[100] K. Dolgaleva, R.W. Boyd, and P.W. Milonni, "Influence of local-field effects on the radiative lifetime of liquid suspensions of Nd: YAG nanoparticles," *Journal of the Optical Society of America B*, vol. 24, 2007, pp. 516-521.

[101] T. Kushida, H.M. Marcos, and J.E. Geusic, "Laser transition cross-section and fluorescence branching ratio for Nd3 in yttrium aluminum garnet," *Phys. Rev*, vol. 167, 1968, pp. 289–291.

[102] M.C. Tan, G.A. Kumar, R.E. Riman, M.G. Brik, E. Brown, and U. Hommerich, "Synthesis and optical properties of infrared-emitting YF3: Nd nanoparticles," *Journal of Applied Physics*, vol. 106, 2009, p. 3118.

[103] J.W. Stouwdam and F. van Veggel, "Near-infrared emission of redispersible Er3+, Nd3+, and Ho3+ doped LaF3 nanoparticles," *Nano letters*, vol. 2, 2002, pp. 733-737.

## Author's Biography

Andrew Brzezinski was born in Brampton, Ontario, Canada in 1969. After gaining considerable work and life experiences, he entered the Engineering Science program at the University of Toronto in 2000. Andrew graduated in 2004 from the University of Toronto with a Bachelor of Applied Science, with Honors. In 2004, Andrew became a PhD candidate in the Department of Materials Science and Engineering at the University of Illinois in Urbana-Champaign, under the joint supervision of Professor Paul Braun and Professor Pierre Wiltzius. Andrew's research focused on engineering and characterizing the behavior of light in photonic crystal. Andrew graduated from the University of Illinois in 2010 with a PhD degree.